Novel hardware for terahertz time-domain spectroscopy (THz-TDS)

by

Benjamin Seam-Yu Ung

B. Eng. (Computer Systems Engineering with Hons.)
B. Sci. (Mathematics & Computer Science),
The University of Adelaide, 2006

Thesis submitted for the degree of

Doctor of Philosophy

in

School of Electrical and Electronic Engineering
Faculty of Engineering, Computer & Mathematical Sciences
The University of Adelaide

2013

Supervisor: Prof Derek Abbott
Co-supervisor: Dr Bernd Michael Fischer
Co-supervisor: Dr Brian Wai-Him Ng

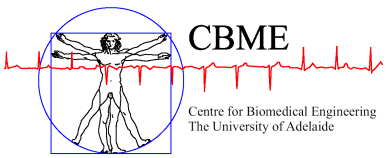

Contents

Abstract

Terahertz time-domain spectroscopy (THz-TDS) systems have been generally limited to a single mode of operation, either in transmission or reflection geometries. The possibility of systems able to operate simultaneously in both geometries opens new possibilities for material characterisation. This Thesis designs and characterises a novel system able to simultaneously capture spectra from samples at normal incidence transmission and reflection. This enables materials that are opaque and/or partially reflective, as well as materials that exhibit non-unity values of permittivity and/or permeability to be thoroughly investigated.

In addition to a dual geometry system, this Thesis presents two novel beam-splitters useable in the terahertz (THz) range of frequencies from 0.1 to 10 THz. Optical components in the THz frequency range have been limited, with ongoing developments being made to fabricate and characterise lenses, polarizers and waveguides, with beam-splitters that are polarization dependent. The presented original contributions include a low-cost beam-splitter fabricated from an ultra-thin polymer substrate and silver paint, and a novel beam-splitter fabricated from conductive polymers. These beam-splitters provide a near frequency and polarization independent response.

An introductory background into THz-TDS along with generation and detection methods are also offered as part of this Thesis. Four auxiliary investigations are also described in the appendices: (i) a dual scanning THz-TDS system, to improve acquisition times, (ii) a mini investigation into food quality control using THz-TDS, (iii) an investigation into security applications for THz-TDS and (iv) second harmonic generation (SHG) using a β radiation damaged barium borate (BBO) crystal and a Ti:Sapphire laser.

Statement of Originality

This work contains no material that has been accepted for the award of any other degree or diploma in any university or other tertiary institution to Benjamin Seam-Yu Ung and, to the best of my knowledge and belief, contains no material previously published or written by another person, except where due reference has been made in the text.

I give consent to this copy of my thesis when deposited in the University Library, being made available for loan and photocopying, subject to the provisions of the Copyright Act 1968. The author acknowledges that copyright of published works contained within this thesis resides with the copyright holder(s) of those works.

I also give permission for the digital version of my thesis to be made available on the web, via the University's digital research repository, the Library catalogue, the Australasian Digital Theses Program (ADTP) and also through web search engines, unless permission has been granted by the University to restrict access for a period of time.

	30/08/2013
Signed	Date

Acknowledgments

Thanks be to the Lord Jesus Christ! Without Him I would not have been given this great opportunity to praise and exalt Him with all the trials and tribulations throughout this PhD.

There are so many people I would like to thank for the journey to the completion of this thesis and this space can not fully express my deepest gratitude to all of you.

I would like to express my gratitude to my principal supervisor, Prof Derek Abbott for taking me on as a PhD candidate and giving me the opportunity to work in the field of terahertz spectroscopy. His constant stream of ideas and concepts, delicate use of the English language, generosity with travel funding and easy going nature have been extremely encouraging and helpful for the course of my research in the University of Adelaide. Many thanks must be given to my co-supervisors, Dr Bernd M. Fischer and Dr Brian W.-H. Ng, as well as other great scientists, Prof Christophe Fumeaux and Dr Withawat Withayachumnankul, of whom I have had the pleasure to work with. I am very much grateful to Dr Bernd M. Fischer for his vast experience in the THz field, used to great effect in helping to establish the Australian National T-ray Facility. His experience was instrumental in me learning the skills necessary to design and build THz systems, while his international links with the community have fostered many new friends and collaborations. I am also grateful to Dr Brian W.-H. Ng, who has provided many alternative insights and thoughtful discussions to guide my research. To Prof Christophe Fumeaux, I am very much grateful for helping to guide me the direction of my research, especially with Dr Bernd M. Fischer's return to Europe. His help in developing the beam-splitters presented in this Thesis has been invaluable. Dr Withawat Withayachumnankul, has been a pleasure to work with during his own PhD and as a postdoctoral fellow. His wealth of knowledge, friendship and humour has been a highlight. Thanks are also in order to Prof Emma MacPherson, an international collaborator from The Chinese University of Hong Kong, who hosted my many visits in Hong Kong.

I would also like to express my appreciation to the staff of The School of Electrical & Electronic Engineer at The University of Adelaide. To the technical staff, Mr Ian Linke, Mr Brandon Pullen, Mr Alban O'Brien, Mr Pavel Simcik and Mr Danny Di Giacomo

for many fruitful discussions and helping me fabricate the many devices and sample holders used throughout my research. Many thanks to the administrative staff, Mrs Rose-Marie Descalzi and Mrs Ivana Rebellato for their assistance. Many thanks to the Computer Services staff, Mr David Bowler, Mr Mark Innes and Mr Ryan King for helping with the many IT related issues that cropped up. To all the teaching staff, A/Prof Mike Liebelt, Dr Benham Jamali, Mr Alfio Grasso, Dr Andrew Allison and Mr Charlie Green, thank you all for enabling the experiences I gained by teaching many courses during my PhD candidature.

I would like to also acknowledge the funding bodies that made all of this work possible. Thank you to the University of Adelaide for awarding me a Divisional Scholarship (2006), as well as the Research Abroad Scholarship (2010) that supported me during my PhD as well as giving me the opportunities to travel abroad and visit international collaborators. The Australian Research Council is also greatly gratefully acknowledged for funding Discovery Projects DP120100661, DP120100200, DP1097281, DP1095151 and DP0988673.

To all the people of the Adelaide T-ray Group, in particular, Dr Hungyen Lin, who I would like to specially like to acknowledge and thank for all your support and friendship. Thank you also to Mr Henry Ho, Mr Shaoming Zhu, Mr Andrew Li, Dr Shaghik Atakaramians and Mrs Inke Jones for the encouragement and friendship over the course of my PhD candidature. It has been a privilege to have worked with so many talented and dedicated people.

Of the two committees that I have served in, the schools Occupational Health, Safety and Well-being (OHSW), and the Electrical and Electronic Engineering Society of Adelaide University (EEESAU), it has certainly been a pleasure and learning experience. Special thanks are due to the head of School A/Prof Cheng Chew Lim, Mr Stephen Guest, Mr Greg Pullman, Mr David Vowles and Dr Said Al-Sarawi of the OHSW committee, as well as Mr Simon Knight, Mr Luke Bolzan, Dr Zhining Lim, Dr Gretel Png, Dr Bobby Yau, Dr Daniel Kelly, Mr Adam Burdeniuk, Ms Hui Min Tan, Dr Muammar Kabir, Mr Robert Moric and Mr James Kitchener of the EEESAU executive committee.

To all the academic staff that I have not yet mentioned, Dr Mathias Baumert, Dr Thomas Kaufmann and Prof Bevan Bates and also, all the postgraduate students that I have met along this journey, Dr Omid Kavehei, Mr Mostafa Rahimi Azghadi, Ms Taraneh Arianfar, Mr Danny Wong, Mr Arash Mehdizadeh, Mr Muhammad Asraful

Hasan, Mr Sam Darvishi and Mr Pouria Yaghmaee, thank you for the encouragement and the jokes told over many conversations.

Outside of work I must thank all my friends, particularly the Best Man at my wedding, Theodore Bourlotos and his family, the support has been nothing short of inspiring. To the staff of the Evangelical Society, Mr Geoff Lin, Mr Dave Brown and Mr Reuben Salagaras, thank you all for your ministry at the university. To all my fellow Christian brothers and sisters of the Austral-Asian Christian Church, thank you all for your continual support and encouragement to Christ our Lord.

Finally, and most important of all I must express my deepest and sincere gratitude to my family. To my Grandpa, thank you so much for being there all my life, unfortunately you didn't quite make it make it to see this Thesis get printed, this work is in dedication to you. To my parents, Mum and Dad, thank you so much for all the support over the many long years, the advice that is always there and the abundance of love you give me. Last but by no means least, to my lovely and beautiful wife Angel, thank you for being the rock of our marriage, the willingness to always listen, the love that you give me and finally the patience to see the light at the end of the tunnel!

For Grandpa

Conventions

Typesetting : This Thesis is typeset using the LaTeX2e software. Processed plots and images were generated using Matlab 7.6 (Mathworks Inc.) and Adobe Illustrator CS6 (Adobe Systems Incorporated) was used to produce schematic diagrams and other drawings.

Spelling : Australian English spelling has been adopted throughout, as defined by the Macquarie English Dictionary (Yallop and Delbridge 2005). Where more than one spelling variant is permitted such as 'biassing' or 'biasing' and 'infra-red' or 'infrared' the option with the fewest characters has been chosen.

System of units : The units comply with the international system of units recommended in an Australian Standard: AS ISO 1000—1998 (*Standards Australia Committee ME/71, Quantities, Units and Conversion* 1998).

Physical constants : The physical constants comply with a recommendation by the Committee on Data for Science and Technology: CODATA (Mohr *et al.* 2012).

Frequency band definition : The terahertz spectrum from 0.1 to 10 THz is referred to as terahertz radiation as opposed to 'T-rays' in Abbott and Zhang (2007). This is because of the growing popularity of terms such as 'terahertz time-domain spectroscopy—THz-TDS' and 'terahertz gap' in the community.

Referencing : The Harvard style is used for referencing and citation in this Thesis.

Publications

Journal Publications

UNG-B. S.-Y., WENG-B., SHEPHERD-R., ABBOTT-D., & FUMEAUX-C., (2013). Inkjet printed conductive polymer-based beam-splitters for terahertz applications, *Optics Materials Express*, **3**(9), pp. 1242–1249.

UNG-B. S.-Y., LI-J., LIN-H., FISCHER-B. M., WITHAYACHUMNANKUL-W., & ABBOTT-D., (2013). Dual-mode terahertz time-domain spectroscopy system, *IEEE Transactions on Terahertz Science and Technology*, **3**(2), pp. 216–220.

UNG-B. S.-Y., FUMEAUX-C., LIN-H., FISCHER-B. M., NG-B. W.-H., & ABBOTT-D., (2012). Low-cost ultra-thin broadband terahertz beam-splitter, *Optics Express*, **20**(5), pp. 4968–4978.

LI-J., SHAH-C. M., WITHAYACHUMNANKUL-W., **UNG-B. S.-Y.**, MITCHELL-A., SRIRAM-S., BHASKARAN-M., CHANG-S., & ABBOTT-D., (2013). Flexible terahertz metamaterials for dual-axis strain sensing, *Optics Letters*, **38**(12), pp. 2104–2106.

LI-J., SHAH-C. M., WITHAYACHUMNANKUL-W., **UNG-B. S.-Y.**, MITCHELL-A., SRIRAM-S., BHASKARAN-M., CHANG-S., & ABBOTT-D., (2013). Mechanically tunable terahertz metamaterials, *Applied Physics Letters*, **102**(12), art. no. 121101.

NIU-T., WITHAYACHUMNANKUL-W., **UNG-B. S.-Y.**, MENEKSE-H., BHASKARAN-M., SRIRAM-S., & FUMEAUX-C., (2013). Experimental demonstration of reflectarray antennas at terahertz frequencies, *Optics Express*, **21**(3), pp. 2875–2889.

KHODASEVYCH-I. E., SHAH-C. M., SRIRAM-S., BHASKARAN-M., WITHAYACHUMNANKUL-W., **UNG-B. S.-Y.**, LIN-H., ROWE-W. S. T., ABBOTT-D., & MITCHELL-A., (2012). Elastomeric silicone substrates for terahertz fishnet metamaterials, *Applied Physics Letters*, **100**(6), art. no. 061101.

LIN-H., FUMEAUX-C., **UNG-B. S.-Y.**, & ABBOTT-D., (2011). Comprehensive modeling of THz microscope with a sub-wavelength source, *Optics Express*, **19**(6), pp. 5327–5338.

WITHAYACHUMNANKUL-W., PNG-G. M., YIN-X., ATAKARAMIANS-S., JONES-I., LIN-H., **UNG-B. S.-Y.**, BALAKRISHNAN-J., NG-B. W.-H., FERGUSON-B., MICKAN-S. P., FISCHER-B. M., & ABBOTT-D., (2007). T-ray sensing and imaging, *Proceedings of the IEEE*, **95**(8), pp. 1528-1558.

Conference Publications

UNG-B. S.-Y., BALAKRISHNAN-J., FISCHER-B. M., NG-B. W.-H., & ABBOTT-D., (2006). Substance Detection for Security Screening Using Terahertz Imaging Technology, *31st International Conference on Infrared and Millimeter Waves and Terahertz Waves*, Shanghai, China, doi: 10.1109/ICIMW.2006.368655.

UNG-B. S.-Y., BALAKRISHNAN-J., FISCHER-B. M., NG-B. W.-H., & ABBOTT-D., (2006). Terahertz detection of substances for security related purposes, *Proc. SPIE Smart Structures, Devices, and Systems III*, vol. 6414, Adelaide, Australia, art. no. 64141U

UNG-B. S.-Y., NG-B. W.-H., & ABBOTT-D., (2008). Toward quality control of food using terahertz, *Proc. SPIE Microelectronics, MEMS, and Nanotechnology*, vol. 6799, Canberra, Australia, art. no. 67991E.

UNG-B. S.-Y., NG-B. W. -H., & ABBOTT-D., (2008). Simultaneous dual scanning terahertz system, *33rd International Conference on Infrared and Millimeter Waves and Terahertz Waves*, Pasadena, USA, doi: 10.1109/ICIMW.2008.4665807.

UNG-B. S.-Y., FISCHER-B. M., NG-B. W.-H., & ABBOTT-D., (2009). Comparative investigation of detection of melamine in food powders, *34th International Conference on Infrared and Millimeter Waves and Terahertz Waves*, Busan, Korea, doi: 10.1109/ICIMW.2009.5324952.

UNG-B. S.-Y., NG-B. W.-H., & ABBOTT-D., (2010). A preliminary study of hydrogenation of oils using terahertz time domain spectroscopy, *35th International Conference on Infrared and Millimeter Waves and Terahertz Waves*, Rome, Italy, doi: 10.1109/ICIMW.2010.5612480.

UNG-B. S.-Y., FUMEAUX-C., LIN-H., FISCHER-B. M., NG-B. W.-H., & ABBOTT-D., (2012). Power scaling of ultra-thin terahertz beam-splitters, *37th International Conference on Infrared and Millimeter Waves and Terahertz Waves*, Wollongong, Australia, doi: 10.1109/IRMMW-THz.2012.6380077.

LI-J., SHAH-C. M., WITHAYACHUMNANKUL-W., **UNG-B. S.-Y.**, SRIRAM-S., BHASKARAN-M., CHANG-S., & ABBOTT-D., (2013). Planar terahertz metamaterials for strain sensing, *37th International Conference on Infrared and Millimeter Waves and Terahertz Waves*, Wollongong, Australia, doi: 10.1109/IRMMW-THz.2012.6380222.

NIU-T., WITHAYACHUMNANKUL-W., **UNG-B. S.-Y.**, MENEKSE-H., BHASKARAN-M., SRIRAM-S., & FUMEAUX-C., (2013). Design and implementation of terahertz reflectarray, *37th International Conference on Infrared and Millimeter Waves and Terahertz Waves*, Wollongong, Australia, doi: 10.1109/IRMMW-THz.2012.6380422.

SHAH-C. M., SRIRAM-S., BHASKARAN-M., KHODASEVYCH-I., WITHAYACHUMNANKUL-W, **UNG-B. S.-Y.**, LIN-H., ABBOTT-D., & MITCHELL-A. (2011). Microfabrication of flexible large-area terahertz fishnet metamaterials, *International Conference on Materials for Advanced Technologies*, Singapore.

LIN-H., **UNG-B. S. Y.**, FISCHER-B. M., MICKAN-S. P., & ABBOTT-D. (2009). Effect of crystal thickness in localized terahertz generation via optical rectification in ZnTe — preliminary investigation, *34th International Conference on Infrared and Millimeter Waves and Terahertz Waves*, Busan, Korea, doi: 10.1109/ICIMW.2009.5325560.

WITHAYACHUMNANKUL-W., **UNG-B. S.-Y.**, FISCHER-B. M., & ABBOTT-D., (2009). Measurement of linearity in THz-TDS, *34th International Conference on Infrared and Millimeter Waves and Terahertz Waves*, Busan, Korea, doi: 10.1109/ICIMW.2009.5324721.

List of Figures

List of Tables

Chapter 1

Introduction

TERAHERTZ (THz) or T-ray radiation spans the frequency range from 0.1 to 10 THz. This region lies in the electromagnetic spectrum between the millimetre wave and the infrared bands. Currently, discrete terahertz generation sources and their corresponding detection techniques have been developed both within the laboratory and also in the context of consumer level devices. These systems and devices are ever increasing in sophistication and generated power.

This introductory Chapter will provide a brief overview of THz radiation, THz time-domain-spectroscopy (THz-TDS) and an outline of this thesis.

1.1 Introduction

This Chapter provides a brief overview of THz radiation and the motivation for research to improve THz beam splitters for various applications and for a novel simultaneous reflective and transmission mode THz-TDS system. An outline of the Thesis and a summary of the novel contributions are presented.

1.1.1 Terahertz Radiation

Terahertz or T-ray radiation ranges from 0.1 to 10 THz in the electromagnetic spectrum, with 1 THz corresponding to a period of 1 ps, 10^{12} cycles per second, a wavelength of 300 μm or a colour temperature of 48 Kelvin (Abbott and Zhang 2007). This frequency range is surrounded by the neighbouring millimetre wave and infrared regions and represents the so-called 'THz-Gap'. This is in-between the regions of the spectrum normally associated with electronics and photonics, as can be seen in Fig. 1.1. The generation of the THz range of frequencies has so far been challenging due to the significant difference to that of techniques employed in the neighbouring regions. Some sources and detectors borrowed from these regions such as, Backward-Wave Oscillators (BWOs) and Fourier-Transform Infrared-spectroscopy (FTIR) along with liquid nitrogen or helium cooled bolometers have difficulty generating and detecting higher than 0.1 THz or lower than 10 THz. Other challenges present in the THz range include high background thermal radiation noise and high atmospheric absorption.

1.1.2 THz Radiation Sources

With the advent of the photoconductive switch by Auston *et al.* (1980), and the mode-locked Ti:Sapphire laser in the 1980s (Moulton 1986), along with associated optics and electronics, THz radiation sources have made significant strides in increasing generated power and accessibility. The following sections briefly describe some of the techniques used for the generation of THz radiation, and outline the basis of THz-TDS (terahertz time-domain spectroscopy).

Pulsed THz Radiation

Pulsed THz radiation schemes rely on a mode-locked laser with pulse widths no longer than 100 fs in duration (Schmuttenmaer 2004, Tonouchi 2007). These lasers are typically

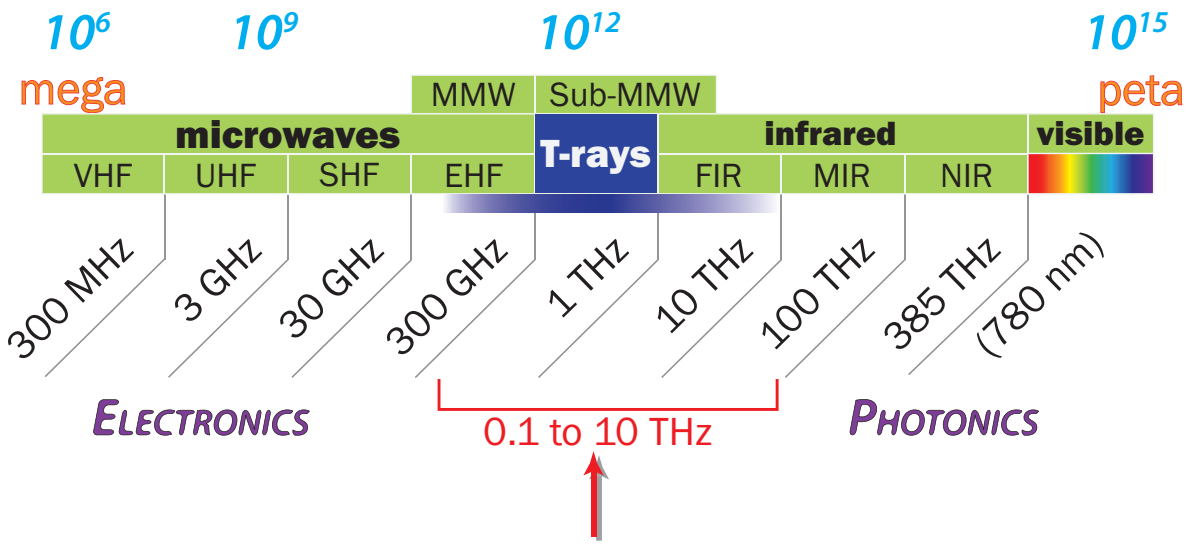

Figure 1.1. The electromagnetic spectrum. The electromagnetic spectrum, centred on THz radiation surrounded on the left and right by the microwave and infrared ranges. The far right shows the location of the visible spectrum with respect to the THz range.

Ti:Sapphire mode-locked lasers, which can also be amplified by use of a multi-pass amplifier or erbium doped ultra-fast fibre lasers. Terahertz radiation is then generated by focusing an incident laser beam onto either a photoconductive material or a non-linear medium. Photoconductive THz emission is generated by the incident laser beam creating photocarriers within the photoconductive material, which are accelerated by an applied DC bias across electrodes (Reimann 2007, Hoffmann and Fülöp 2011). Generation of THz radiation using a non-linear medium is conducted by the process of optical rectification, where the generation of THz is due to optical mixing of the many frequency components constituting the femtosecond laser pulse (Bass *et al.* 1962, Auston and Nuss 1988, Rice *et al.* 1994, Xu *et al.* 2010, Fülöp *et al.* 2012, Nagai *et al.* 2012). Other less common generation techniques include air plasma generation, reflection from an optically excited semiconductor surface, and even quantum-cascade lasers (QCLs) which are beginning to be able to emit pulses at THz frequencies (Gousev *et al.* 1999, Williams *et al.* 2005, Williams 2007), these techniques will be discussed in further detail in Chapter 2.

Continuous-wave THz Radiation

Difference Frequency Generation (DFG), which is the most common form of Continuous-wave (CW) THz radiation, relies on the process of photomixing of two monochromatic optical laser beams focused on a semiconductor (Deninger *et al.* 2008,

Sartorius *et al.* 2012). The two lasers are thus tuned such that the difference between their frequencies matches those in the THz range. The point of focus on the semiconductor is usually accompanied by inter-digitated striplines where a DC bias voltage is applied, as the photocarriers are generated, they are accelerated across the gaps in the inter-digitated striplines generating THz radiation (Gregory *et al.* 2005). Other sources of CW THz radiation include BWOs and QCLs, the latter of which will be discussed more in Chapter 2. Note that BWOs generate THz radiation by means of an electron gun firing a beam of electrons into a vacuum tube containing a slow-wave structure (Gorshunov *et al.* 2005, Philipp *et al.* 2007, Xu *et al.* 2012). An electromagnetic wave is then generated and sustained by the slow-wave structure and propagates in the opposite direction of the electron beam. Also of note, BWOs are currently limited from the gigahertz range to approximately 1 THz, but are now able to generate CW THz radiation at 1 THz with up to 1.9 W average power (Xu *et al.* 2012). Further information on BWOs can be found in Mair *et al.* (2004). However, QCLs are semiconductor lasers where THz radiation is generated by laser transitions between intersubbands in the semiconducting structure (Williams 2007).

1.1.3 THz Detection Methods

A challenge equal to the generation of THz radiation is its detection. Detection of THz radiation can be grouped into two types, direct and indirect methods. Direct detection of THz radiation consists of a detector directly being influenced by an incident THz beam, whereby an induced current or temperature change can be observed. In these cases, a photoconductive switch can be used to observe the induced current, while bolometers cooled to cryogenic temperatures can be used to directly detect incident temperature changes. Indirect methods of THz detection rely on changes an incident THz beam has on a probing laser beam. These methods are reliant on Electro Optical (EO) techniques, requiring a non-linear crystal and either photodiodes or a Charge-Coupled Device (CCD) sensor for observing the indirect changes of the THz beam on the probing laser beam.

1.1.4 THz-TDS by Pulsed Radiation

Coherent detection of THz pulses via a pair of suitably matched emitters and detectors allows samples to measured. This then allows the refractive index and absorption to

be determined simultaneously. This technique is known as THz-TDS, and is useful for determining many characteristics of samples that respond to THz radiation. The physical setups for THz-TDS systems can be seen in Chapter 2.

1.1.5 Applications of THz Radiation

Non-polar, non-metallic and dry materials are transparent to THz radiation. These properties can be exploited for use in multiple scenarios, such as pharmaceutical quality control, where the chemical consistency and makeup of tablets can be individually and non-destructively scanned during manufacture (Zeitler *et al.* 2007, May *et al.* 2011, Russe *et al.* 2012). This also enables the detection of chiral chemicals (Franz *et al.* 2011), which may be potentially hazardous if produced in the wrong orientation. As THz radiation is non-ionising, it can be safely used for many detection procedures in humans at low THz power levels. These include, but are not limited to the following: the possible detection of Alzheimer's plaques (Png *et al.* 2009), skin cancer (Woodward *et al.* 2002, Woodward *et al.* 2003b, Woodward *et al.* 2003a, Wallace *et al.* 2006, Yu *et al.* 2012), breast cancer (Ashworth *et al.* 2009), teeth (Pickwell and Wallace 2006) and other biological tissues (Hadjiloucas *et al.* 1999, Han *et al.* 2000, Pickwell *et al.* 2004, Liu *et al.* 2007a, Markelz 2008). Plastics, polymers and paper are all generally transparent to THz radiation, this leads to many security applications with THz radiation (Ferguson *et al.* 2003, Coward and Appleby 2003, Zandonella 2003, Liu *et al.* 2007b). These applications include the possibility of detecting hidden explosives (Kawase *et al.* 2003, Watanabe *et al.* 2003, Yamamoto *et al.* 2004, Liu *et al.* 2006), while combining the ability to detect biological substances allows for the possible detection of illicit narcotics (Lu *et al.* 2006) and also biological weapons, such as anthrax (Te *et al.* 2002, Wang *et al.* 2002). The property of transparency to polymers was cleverly exploited for the detection of defects caused by air bubbles in the external space shuttle foam (Chiou *et al.* 2007) to prevent future disasters as suffered by the space shuttle Challenger. In this case THz imaging provides advantages over X-rays which do not provide enough contrast to determine defects in soft materials, and the shorter infrared wavelengths which yield too much scattering. The evaluation of genuine artworks also exploits the transparency of paper to THz radiation, where the paints can be scanned and checked for authenticity (Yasuda *et al.* 2007, Adam *et al.* 2009). Terahertz radiation is also readily absorbed by molecular bonds in many non-polar materials in their solid,

liquid and gaseous states (Harde *et al.* 1997, Mittleman *et al.* 1998, Braly *et al.* 2000, Fischer *et al.* 2002, Walther *et al.* 2003, Naftaly and Miles 2007). The energies absorbed by these bonds show characteristic signatures in the absorption spectrum, which allow for material classification and recognition (Jacobsen *et al.* 1996, Strachan *et al.* 2004, Strachan *et al.* 2005, Taday 2004, Fischer *et al.* 2005). Semiconductors can also be characterised by THz radiation, where plasma frequencies, damping rates and carrier dynamics can be probed (van Exter and Grischkowsky 1990a, Jeon and Grischkowsky 1998, Cole *et al.* 2001).

1.2 Motivation

Due to the ever increasing power of generated THz radiation (Weiner *et al.* 1998, Cook and Hochstrasser 2000, Zhong *et al.* 2006, Dai *et al.* 2007, Reimann 2007, Xie *et al.* 2007, Bakunov *et al.* 2010, Clough *et al.* 2011, Fülöp *et al.* 2010, Malik *et al.* 2010, Hoffmann and Fülöp 2011, Jepsen *et al.* 2011, Kawase *et al.* 2011), methods and associated optics need to be developed to exploit the generated power to its maximum potential. Already, many optical components, such as lenses (Lo and Leonhardt 2008, Scherger *et al.* 2011a, Scherger *et al.* 2011b, Siemion *et al.* 2011), filters (Voisiat *et al.* 2011) and waveguides (Mendis and Mittleman 2009, Nielsen *et al.* 2009, Atakaramians *et al.* 2011, Scherger *et al.* 2011c) operating within the THz range have seen increasing investment in research. Monitoring of generated THz radiation is also becoming a requirement, particularly for QCL systems, for system troubleshooting. In order to achieve these advances, beam splitters for THz applications need to be easily produced with arbitrary splitting ratios, have minimal loss and minimal beam deflection. In addition to these qualities, the beam splitter is also ideally be robust and low-cost.

Currently, beam splitters operating in the THz frequency range are either polarization dependent or have a fixed splitting ratio (Homes *et al.* 2007, Berry and Jarrahi 2012, Ung *et al.* 2012). Another consequence of higher generated power is the possibility of having a single source to power detectors for both reflected and transmitted beams simultaneously. Such as system enables new methods of extracting spectroscopic data from samples where they are both reflective and opaque. The simultaneous acquisition of data is able to cut down not only experimental time, but also errors in measurement, where small angular changes in both reflection and transmission modes may be significant, particularly if the reflected and transmitted data are collected individually from separate systems.

In addition, THz-TDS systems are generally limited to single mode operation in either transmission or reflection mode. Thus far, only a single system (Brunner *et al.* 2009), has been able to simultaneously operate in both modes, and work to improve and simplify these setups are yet to be done. The development of such systems opens up key applications requiring both transmission and reflected data simultaneously, whereby materials can be characterised faster and more accurately, particularly with absorptive materials or metamaterials that have non-unity electromagnetic properties. In addition, experimental times can be cut down and SNR improved by removing the need to transfer samples to and from multiple systems.

1.3 Outline of Thesis

This initial introductory Chapter presents a brief background and motivation for the key contributions presented in this Thesis. Chapter 2 presents detailed methods of generation and detection of THz radiation. Many of the low-power generation and detection techniques are present in our THz-TDS systems, designed and implemented in the National T-ray Facility at The University of Adelaide. The generation and detection techniques discussed are necessary to understand the research presented in later Chapters.

Chapter 3 shows the physical setups for THz-TDS in both transmission and reflection geometries using the emitters and detectors discussed in Chapter 2, and also a new simultaneous reflection and transmission system. Data is shown from the various systems with different types of emitters and detectors. The simultaneous reflection and transmission system's operation is also verified by the measurement of samples. This novel system operates as expected with minimal increases in both complexity and cost.

Chapter 4 presents a novel silver conductive paint coated beam splitter. This Chapter presents the theoretical model, fabrication, characterisation results and a comparison with current silicon beam splitters used in THz-TDS.

Chapter 5 details a progression on Chapter 4's silver paint coated beam splitter by detailing THz beam splitters based on PEDOT[1] and PPY[2] conductive polymers. This Chapter provides background on conductive polymers in general and characterises their use as THz beam splitters.

[1] poly(3,4-ethylenedioxythiophene)
[2] polypyrrole

Finally, a summary of the research presented in this Thesis is complemented by a series of identified possible future research directions. The Appendices show the ancillary contributions made during the course of PhD candidature.

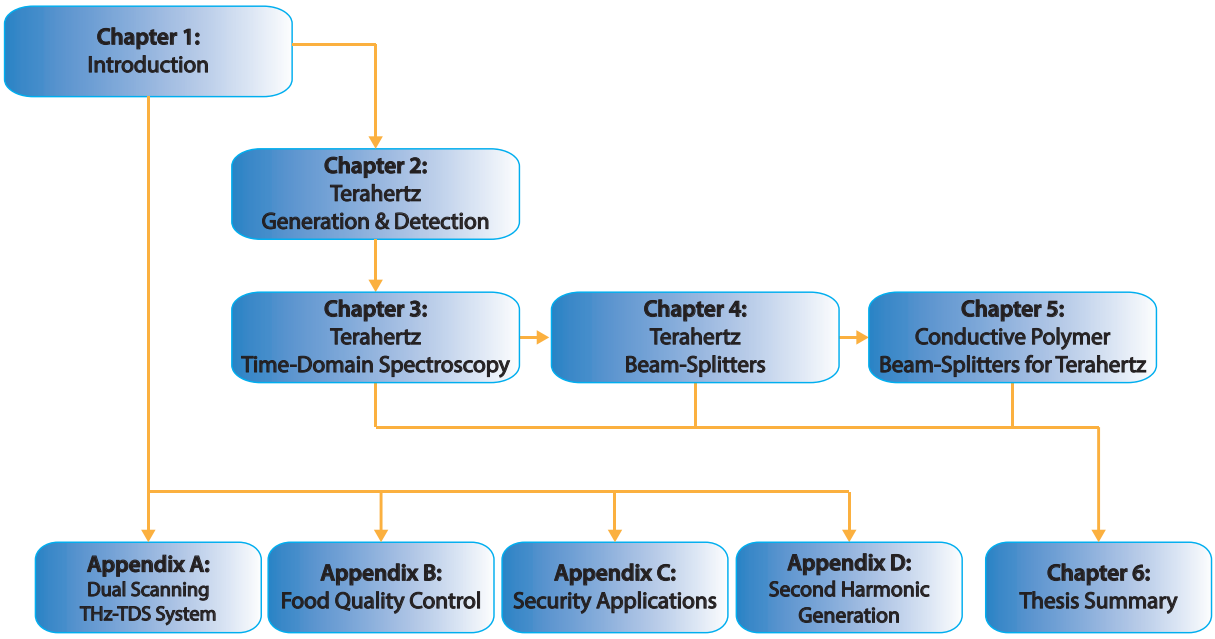

Figure 1.2. Thesis outline. An illustrative outline of this Thesis showing how the Chapters are interlinked with each other.

1.4 Original Contributions

The original contributions presented in this Thesis include the theoretical model and fabrication of two broadband non-polarization dependent beam splitters for the THz range of frequencies. The initially presented beam splitter is based on a thin conductive layer of silver paint on a transparent substrate, which is physically similar to common optical $\lambda/4$ interference based pellicle beam splitters. This beam splitter presents numerous advantages over the currently available beam splitters in the THz range. The results and characterisation of the new beam splitter, in this thesis, have been published (Ung *et al.* 2012).

The follow-up to the initial beam splitter demonstrates the possibility of conductive polymers operating as a beam splitter with the same concept as the silver conductive paint based beam splitter. Here, PEDOT and PPY polymers are inkjet printed on top of a plastic film (Ung *et al.* 2013b). These polymers present an interesting advancement, as the polymers can be conveniently optimized for performance at THz frequencies, while

the inkjet printing yields a much more controllable thickness than rapid prototyping by spray coating the silver conductive paint onto a substrate.

Finally, a simultaneous reflection and transmission THz-TDS system is presented (Ung *et al.* 2013a). This novel system allows for samples to be measured in both reflection and transmission modes, where traditionally THz-TDS systems have either been single mode reflection or transmission. This new system provides for a decrease in measurement times in certain scenarios, and also allows a decrease in measurement errors, particularly where samples need to be positioned accurately and measured in both reflection and transmission modes.

Ancillary contributions for this Thesis are included in the Appendix, these contributions include the following:

- Dual scanning THz-TDS system
  In order to decrease measurement times of THz-TDS systems, a dual scanning system was developed to concurrently measure two transmission systems working from a single optical delay line (Ung *et al.* 2008). This system enables either a sample to be simultaneously measured concurrently with a reference measurement or two samples to be measured at the same time. The simultaneous measurements imply that measurement times can be halved and SNR can be improved, as laser noise in measurements can be removed from simultaneously acquired reference and sample data.

- Mini-investigation into food quality control using THz-TDS
  Investigations into the possibility of monitoring the quality standards of both infant milk powder and cooking oils is performed (Ung *et al.* 2009). The preliminary study on infant milk powder focuses on the melamine and cyanuric acid lacing of infant milk powder by some manufacturers in order to increase protein count. Both THz-TDS and FTIR measurements are performed and compared to determine the minimal concentration measurable by both systems, and the possibility of integration into manufacturing process. Measurements on cooking oils are performed to check for saturated fats in various off-the-shelf consumer cooking oils (Ung *et al.* 2010).

- Mini-investigation into security applications for THz-TDS
  A preliminary study into the possibility of scanning through common suitcase

materials to determine if contents contained illicit materials is performed by cotton sheets laced with a known substance with a THz signature sandwiched between various plastics to simulate clothing packed in a suitcase (Ung *et al.* 2006). As the THz beam is minimally attenuated by the plastics and cotton, the THz signature from the laced substance is still detectable, leading to the possibility of a non-invasive, non-contact and non-destructible method of security screening provided that generated THz power is sufficient to penetrate thicker layers of clothing.

Chapter 2

Terahertz Radiation: Generation & Detection

COMMON THz radiation generation and detection techniques are detailed in this Chapter, particularly for use in high and low power THz-TDS. These techniques can then be applied to implement physical systems in both transmission and reflection geometries, both of which are necessary for the development of the dual-scanning system presented in Chapter 3. Characterisation of the beam splitters discussed in Chapters 4 and 5. High-power generation of THz radiation and other methods of detection are also detailed.

2.1 THz Radiation Sources

Current optical-based generation techniques for THz radiation typically have output powers ranging from μW to mW (Park *et al.* 1998, Faure *et al.* 2004, Löffler *et al.* 2005, Reimann 2007). They can be classed into low and high power generation techniques. Photoconductive antennas, DFG, and Optical Rectification (OR) are generally classed as low-power generation techniques, although OR can also be employed in the high-power range depending on the pump laser. High-power generation techniques generally encompass *air plasma* and QCLs, although other forms of high-power sources are available, such as gyrotrons and syncrotrons. These non-optical based generation techniques will be covered in later sections.

2.1.1 Photoconductive Antennas

Photoconductive antennas (PCAs) are fabricated from a semiconductor substrate with DC biased metal electrodes deposited on top of the surface. The generation of THz radiation from PCA relies on the creation of free carriers by focused ultra-fast laser pulses, sub-picosecond in pulse width, and photon energies greater than the bandgap of the semiconductor material used. The point of focus is generally placed closer to the anode, where the applied DC bias creates a high field region between the two electrodes. The intense electric field accelerates the free carriers across the gap between electrodes, creating a transient current $I(t)$ with a time dependent dipole moment. According to Maxwell's equations, electromagnetic radiation will be emitted with a time dependent electric field $\vec{E}_{\mathrm{THz}}(t)$ described by,

$$I(t) = \left| \frac{\partial p(t)}{\partial t} \right| \quad , \tag{2.1}$$

$$\vec{E}_{\mathrm{THz}}(t) = \frac{1}{4\pi\epsilon_0 c^2 r^3} \vec{r} \times (\vec{r} \times \frac{\partial^2 \vec{p}(t)}{\partial t^2}) \quad . \tag{2.2}$$

As the semiconductor substrate has a sub-picosecond carrier lifetime, the rise time of which is also sub-picosecond, a THz pulse is emitted (Mourou *et al.* 1981, Fattinger and Grischkowsky 1988). This burst of radiation follows colinearly to the incident laser pulse, normal to the surface of the substrate. A crystalline high-impedance (HiZ) hyperhemispherical silicon lens is usually placed on the back surface of the PCA to

collimate the high divergent cone shaped THz radiation, as the HiZ silicon is non-dispersive and non-absorptive (Van Rudd and Mittleman 2002). An illustration of the PCA is shown in Fig. 2.1.

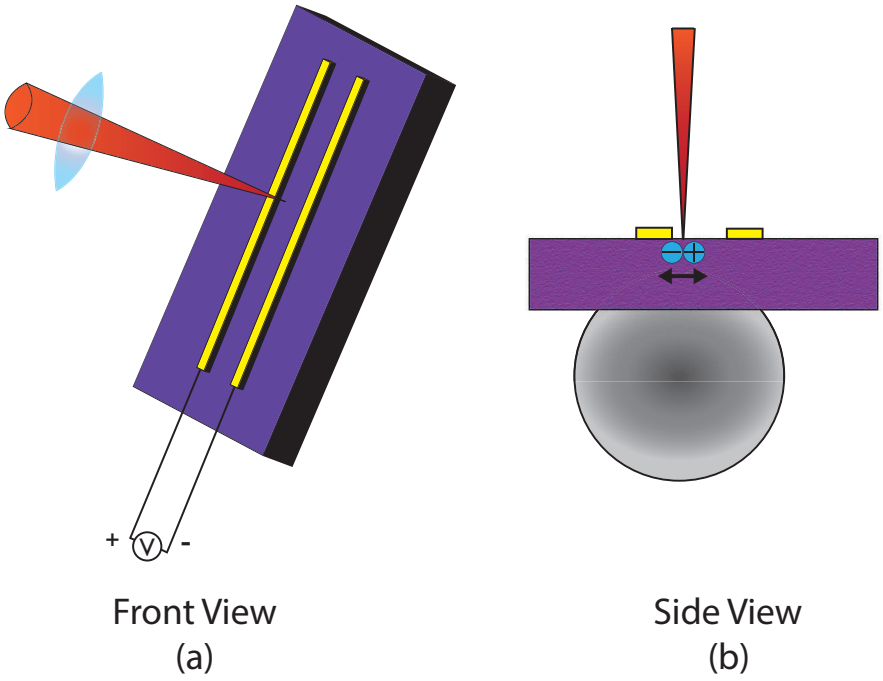

Figure 2.1. Front & side views of PCA emission. The front view (a) depicts an incident focused laser beam onto the PCA. The laser beam is directed between the two electrodes, which are connected to a DC bias. The side view, (b) shows the traversal of the subsequently generated free carriers within the PCA semiconductor substrate. The resultant generated output THz beam is collected and collimated by the hyperhemispherical lens.

The generated THz power from this technique is limited by the DC bias voltage and incident laser intensity, while the generated THz bandwidth is limited by the pulse length of the laser beam, and the carrier lifetime of the semiconductor substrate. The carrier lifetime of the substrate must be sub-picosecond in order for a pulse to be generated with terahertz frequencies. The maximum applied DC bias voltage is dependent on the semiconductor's breakdown voltage, while the maximum applied laser intensity is limited by the damage threshold of the PCA as a whole. An increase in either value results in increases in generated THz power. The carrier lifetime of the semiconductor is highly dependent on the type of semiconductor and its method of growth. It should also be noted that the semiconductor must have a high resistivity of over 10^9 Ohms·cm. This high resistivity is necessary, otherwise *photoconductive persistance* occurs, where the transient current $I(t)$ does not decay to zero during the off-duration of the cycle of incident laser pulses (Ferguson *et al.* 2001). A collection of semiconductors

Semiconductor	Bandgap (eV)	Wavelength (nm)	Resistivity (Ohm·cm)	Carrier Lifetime (ps)	Voltage Breakdown ($kV \cdot cm^{-1}$)
LT-GaAs	1.42	830	10^9	0.3	400
Silicon	1.10	830	10^7	0.8-20.0	300
InGaAs	1.5	1550	10^9	0.3	200
GaN	3.4	330	-	-	2000

Table 2.1. Semiconductors for generating THz radiation. Various semiconductors suitable for THz PCA generation are listed, with their associated bandgaps. These values are adapted from Sakai (2005) and Ferguson *et al.* (2001). Of particular note is GaN, which has a very high voltage breakdown, suitable for large DC bias voltages, but with a large bandgap requiring wavelengths in the blue to UV (ultraviolet) range to excite photocarriers. This requires the use second harmonic generation (SHG) techniques for Ti:Sapphire lasers, which are discussed in Appendix D.

commonly used for THz PCA generation is listed in Table 2.1. Note that PCA generation is able to generate THz at powers greater than 40 μW (Zhao *et al.* 2002b), and also bandwidths up to 20 THz (Shen *et al.* 2003). Commonly, LT-GaAs (low-temperature grown gallium arsenide) is used in conjunction with Ti:Sapphire lasers, as LT-GaAs has a direct bandgap close to the center wavelength produced by these lasers, where the electrons of the LT-GaAs are excited into the valance band directly by the incident beam. Other commonly used lasers, such as erbium doped ultra-fast fibre lasers operate with a centre wavelength of 1.55 μm, which require a semiconductor with an associated bandgap. In this case, InGaAs (indium gallium arsenide) has been fine tuned for use as a PCA substrate material. Another possible future substrate is GaN (gallium nitride) that has many advantageous properties, such as a higher breakdown voltage, but suffers from photoconductive persistence and problems with growing the semiconductor at a high enough resistivity (Ferguson *et al.* 2001).

The electrode structure of the PCA also has a large affect on the generated THz power and bandwidth. In particular, the spacing between the electrodes of the PCA greatly affect the possible generated power and bandwidth. For a simple paired stripline structure, it is possible to generate more THz power if the striplines are placed further apart, as the DC bias voltage and laser intensity can be increased before the voltage breakdown and damage threshold can be reached—this is however at the cost of maximum bandwidth (Walther 2003, Tani *et al.* 2012). If the opposite occurs, where the striplines

are brought closer together, more bandwidth can be achieved, as the recombination times of free carriers are reduced due to the smaller travel distance between electrodes, thus generating shorter, less intense THz pulses (Walther 2003). Bow-tie antennas are another commonly used structure, offering higher generated powers due to a generally large gap between electrodes, while also having a large electrical contact area. However, there is a disadvantage with bow-tie antennas, as the large metal contact area tends to produce many echoes in the generated THz pulse, which significantly reduces usable bandwidths compared to stripe-line based antennas (Walther 2003).

Alternatively, newer structures for PCAs have been developed. Of significant interest is the PCA array structure, where multiple striplines are placed together, with opposite electrodes connected to opposite polarities, forming an inter-digitated structure. This structure does away with the need for a HiZ Si lens to collect and collimate a THz beam from other PCAs, as the array structure is usually of large area (Awad *et al.* 2007a, Awad *et al.* 2007b). Other benefits of the array structure over stripline, bow-tie and H-dipole PCAs, are that array structures generally are able to emit more THz power over a larger bandwidth, provided that the array structure is designed accordingly and a pump laser beam does not need to be focused tightly onto the surface of the PCA. Figure 2.2 shows a comparison between the previously mentioned PCA structures.

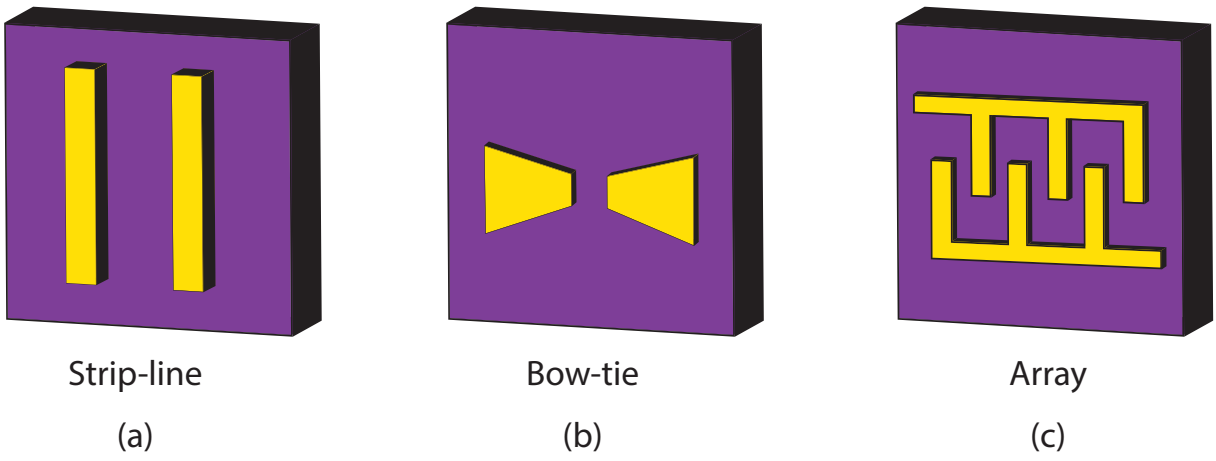

Figure 2.2. Commonly used PCA structures for THz emission. (a) and (b) show the strip-line and bow-tie structures commonly used for THz emission, while (c) shows the more recently developed array structure that does not require a HiZ Si lens for collimation.

2.1.2 Continuous Wave

Difference Frequency Generation (DFG), techniques for THz generation rely on photomixing a pair of tunable monochromatic lasers. The two lasers are tuned such that the frequency difference between the two output wavelengths is equal to a frequency in the THz region. The resultant laser beam is then focused onto an inter-digitiated PCA structure, where a THz beam of a singular frequency is generated, Figure 2.3 shows an inter-digitated PCA for DFG systems. As the two lasers are tuned, it is possible to sweep through a large frequency range in steps down to 250 MHz (Sartorius *et al.* 2012), offering a very high frequency resolution in the THz range. Note that DFG systems can operate at multiple laser center wavelengths, with newer systems lowering costs by employing the use of widely available and well established communications lasers operating at wavelengths of 1.55 μm (Sartorius *et al.* 2012). These systems offer many benefits, in that they are relatively low cost, offer fast operation and compactness, as the laser is fibre-coupled rather than free space. The disadvantage of using DFG systems is however that they do not retain phase data from samples (Gregory *et al.* 2005, Sartorius *et al.* 2012).

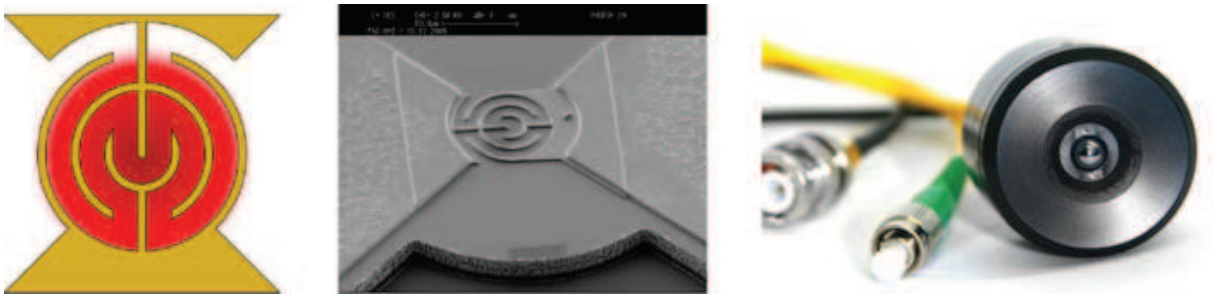

Figure 2.3. A PCA for DFG THZ systems. From left, a diagram of a PCA for DFG generation and detection, micrograph of the fabricated PCA, and an assembled PCA mounted with a silicon lens and optical fibre. After Sartorius *et al.* (2012).

2.1.3 Optical Rectification

Optical Rectification (OR) can be most easily described as a DC polarization generated by the interaction of an intense laser beam with a non-linear optical medium (Bass *et al.* 1962, Rice *et al.* 1994, Sakai 2005). This non-linear second-order optical effect was first observed by Bass *et al.* in 1962, where the effect was exhibited by shining a ruby laser on a potassium dihydrogen phosphate (KDP) crystal (Bass *et al.* 1962). For THz generation, the THz pulse is generated by difference between frequency

components of an incident laser pulse. This process is capable of producing electric fields ranging from DC to mid-infrared frequencies (Ward 1966, Bonvalet *et al.* 1995), but is hampered by a low conversion efficiency and phase-matching difficulties (Shen 2003). Despite these difficulties, bandwidths of over 40 THz (Bonvalet *et al.* 1995) and a maximum conversion efficiency of 0.21%, in a $LiNbO_3$ crystal pumped by an amplified Ti:Sapphire laser, have been demonstrated in a high-power THz system (Fülöp *et al.* 2010, Nagai *et al.* 2012). Zinc Telluride (ZnTe) is another crystal that is commonly used in THz OR generation, and can be pumped by both amplified and non-amplified Ti:Sapphire lasers for high and low power generation, respectively (Rice *et al.* 1994, Park *et al.* 1998, Bartel *et al.* 2005, Tani *et al.* 2011, Fülöp *et al.* 2012).

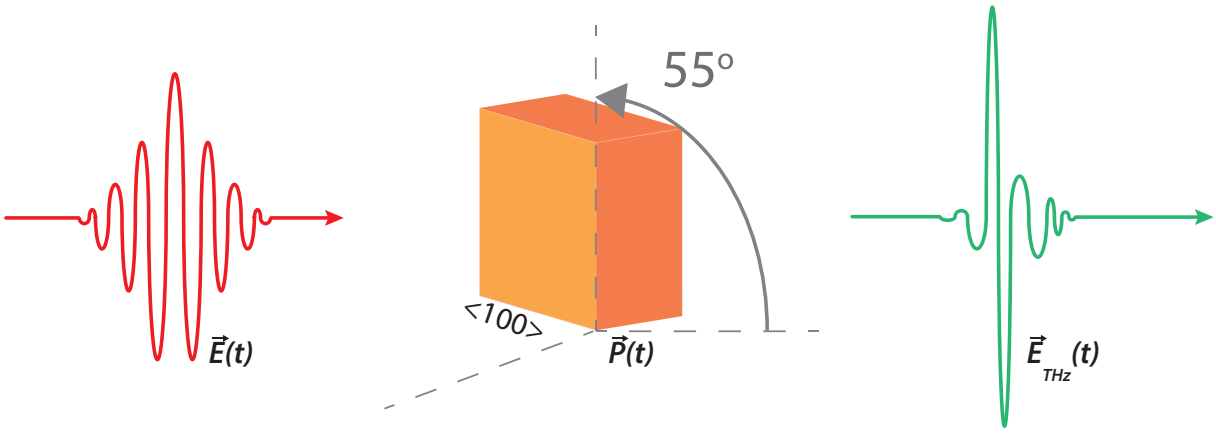

Figure 2.4. An illustration of OR for THz generation. An intense horizontally polarized laser pulse is incident on an EO crystal growth on the crystallographic axis of $\langle 100 \rangle$. If the crystal is rotated to the azimuthal angle, in this case 55°, it will be at the optimal angle to generate the maximum output THz pulse.

The theoretical model of OR generation can be explained by Equations 2.3 to 2.5. It is commonly found that the second-order tensor $\chi^{(2)}$ is the dominant term in Equation 2.3, with all other high-order components assumed to be negligible.

$$\vec{P}(t) = \epsilon_0(\chi^{(1)} \cdot \vec{E}(t) + \chi^{(2)} \cdot \vec{E}^2(t) + \chi^{(3)} \cdot \vec{E}^3(t) + \dots) \quad , \tag{2.3}$$

where $P(t)$ is the sum of the non-linear polarizations, $\chi^{(1\dots n)}$ are the n^{th} order tensors and $\vec{E}^{1\dots n}(t)$ are the n^{th} order electric field vectors.

Assuming that the incident light is a plane wave traveling through free space, its electric field can be expressed as,

$$\vec{E}(t) = \int_0^\infty E(\omega) \cdot e^{-i\omega t} d\omega \quad . \tag{2.4}$$

Now, substituting this Equation back into equation 2.3, along with the difference frequency components of the incident laser beam, Ω, the second-order non-linear polarization can be defined as

$$\vec{P}_{NL}^{(2)}(\omega) = 2\chi^{(2)} \int_0^\infty \int_0^\infty \vec{E}(\omega + \Omega) \cdot \vec{E}(\omega) \cdot e^{-i\Omega t} d\Omega d\omega \quad . \tag{2.5}$$

It is then possible to model the propagation of the THz pulse $\vec{E}_{\mathrm{THz}}$ by Maxwell's wave equation in a non-linear medium,

$$(\nabla^2 - \frac{\epsilon(\omega)}{c^2} \cdot \frac{\partial^2}{\partial t^2}) \vec{E}_{\mathrm{THz}}(t) = \frac{4\pi}{c^2} \cdot \frac{\partial^2 \vec{P}(t)}{\partial t^2} \quad , \tag{2.6}$$

where the THz wave equation can be solved by using the first Born approximation under the assumption that there is negligible depleted light incident on the non-linear crystal (Sakai 2005).

Many organic and inorganic crystals can be used for OR generation, Table 2.2 lists the most commonly used crystals for THz generation (Rice *et al.* 1994, Bonvalet *et al.* 1995, Carrig *et al.* 1995, Wu and Zhang 1996, Huber *et al.* 2000, Nagai *et al.* 2012). If the incident pump laser beam is horizontally polarized in propagation towards the EO crystal's crystallographic axis $\langle 100 \rangle$, the optimal generation of THz pulses occurs at the four Azumith angles, beginning at 55° and rotating through to 325° in 90° increments (Bonvalet *et al.* 1995, Chen and Zhang 1999). In practical setups, the crystal is physically rotated to 55° to yield the highest generated SNR as well as the highest usable bandwidth. This setup is illustrated in Figure 2.4.

2.1.4 Air Plasma

The latest technique for THz generation involves the use of *air plasma*. Air plasma systems are more complex than other generation techniques and, like other high-power based THz systems, require the use of an amplified Ti:Sapphire laser. A surprising fact of air plasma generation is the generation medium, which as the name

Crystal Name	Abbreviation
4-Dimethylamino-N-Methyl-4-Stilbazolium-Tosylate	DAST
Gallium Phosphate	GaP
Gallium Sellenide	GaSe
Potassium Dihydrogen Phosphate	KDP
Lithium Niobate	$LiNbO_3$
Zinc Telluride	ZnTe

Table 2.2. A list of EO crystals for THz systems. A list of common non-linear crystals used for OR generation of THz pulses.

implies, is simply atmospheric air. Air plasma based generation was first developed by Cook and Hochstrasser (2000), at the University of Pennsylvania, where THz pulses of over 3 THz bandwidth were observed. Many other groups quickly followed with enhancements to Cook *et al.*'s developments, with universities in Germany (Kress *et al.* 2004, Löffler *et al.* 2005), Canada (Wang *et al.* 2010) and USA (Zhong *et al.* 2006, Xie *et al.* 2007, Clough *et al.* 2011). This generation technique employs the use of four-wave-mixing in a plasma (Cook and Hochstrasser 2000, Reimann 2007), where a β-barium borate (BBO) crystal is used for second-harmonic generation (SHG) of the fundamental frequency ω_0 to $2\omega_0$. To explain the non-linear optical mechanics of the four-wave-mixing, the third-order susceptibility needs to be observed. Where the third-order polarization $\vec{P}^{(3)}_{\mathrm{NL}}(\Omega)$ can be observed in the generated plasma (Reimann 2007), and the fundamental laser pulse is broadband, containing the frequency components ω_0 to ω_4,

$$\begin{aligned}\vec{P}^{(3)}_{\mathrm{NL}}(\Omega) = \epsilon_0\chi^{(3)}(\Omega = \omega_1 + \omega_2 - 2\omega_0; -2\omega_0, \omega_1, \omega_2) \cdot \vec{E}^*(2\omega_0) \cdot \vec{E}(\omega_1) \cdot \vec{E}(\omega_2) \\ +\epsilon_0\chi^{(3)}(\Omega = 2\omega_0 - \omega_3 - \omega_4; 2\omega_0, -\omega_3, -\omega_4) \cdot \vec{E}(2\omega_0) \cdot \vec{E}^*(\omega_3) \cdot \vec{E}^*(\omega_4) \quad , \quad (2.7)\end{aligned}$$

where ϵ_0 is the permittivity of a vacuum, $\chi^{(3)}$ the third order non-linear tensor, Ω the difference frequency of the four-wave-mixing, and $\vec{E}$ are the optical pulse electric field vectors for the varying optical frequencies $\omega_{0,1,\ldots,4}$.

From this equation, it can be seen that four-wave-mixing of the frequency components is dominated by the mixing of two of the frequencies of the fundamental, ω_1 and ω_2 and the second harmonic $2\omega_0$, to produce $\Omega = \omega_1 + \omega_2 - 2\omega_0$. Within the third order polarisation $\chi^{(3)}$ of the plasma, this produces a wavelength $\lambda_\Omega \approx 100\ \mu$m, which

equates to approximately 3 THz, when the pulse at the fundamental contains wavelengths between 770 to 830 nm (Reimann 2007). Figure 2.5 shows the experimental setup of air plasma generation, as well as the four-wave-mixing in the plasma to produce THz frequencies. The BBO crystal used in this case was of 100 μm in thickness employing type-I phase-matching.

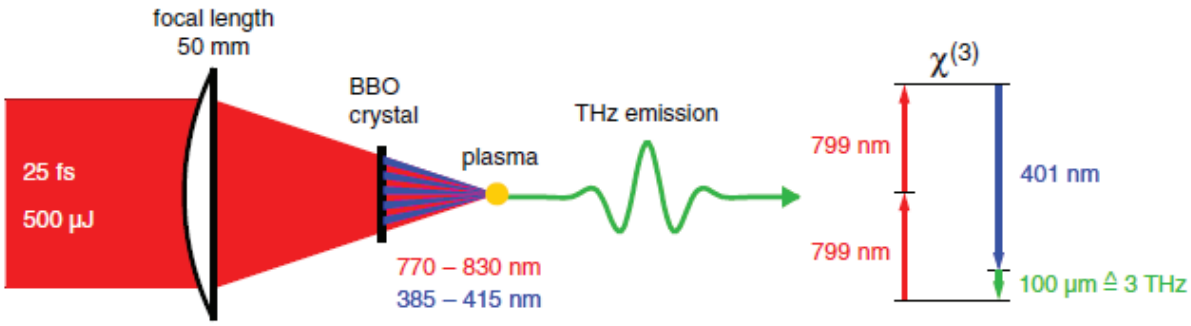

Figure 2.5. Schematic of air plasma generation. On the left of the figure, an amplified ultrafast laser pulse of very narrow pulse width is tightly focused through a BBO crystal to generate intensities high enough to form an air plasma. Four-wave-mixing of the fundamental and second harmonic take place in the air plasma to generate a THz pulse. On the right of the figure, the third-order non-linearity can be visualised when $\lambda_{\omega_1} = \lambda_{\omega_2} = 799$ nm, and $\lambda_{2\omega_0} = 401$ nm. After Reimann (2007).

2.1.5 QCLs

Quantum cascade lasers (QCLs) are an increasingly popular form of THz generation, as they typically offer higher output powers in a singular unit. The principle of operation of a QCL is by the injection of electrons into semiconductor hetrostructures. The electrons travel from the top of the semiconductor and are subsequently trapped in quantum wells at each intersubband, emitting photons as they cascade downward, giving rise to the laser's namesake (Williams 2007). The intersubbands can be modified by altering the thickness of quantum wells, allowing for output wavelengths to be finely tuned. This model was first proposed by Kazarinov *et al.* in 1971 (Kazarinov and Suris 1971). In 1994, Faist *et al.* created the first QCl operating at THz frequencies (Faist *et al.* 1994). Then by 2002, Köhler *et al.* from the Scuola Normale Superiore in Pisa, Italy, in collaboration with the University of Cambridge created the first QCL

lasing at 4.4 THz in the milliwatt power range (Kohler *et al.* 2002). Many other laboratories soon followed this breakthrough shortly afterwards (Rochat *et al.* 2002, Tamosiunas *et al.* 2003, Williams *et al.* 2003, Dhillon *et al.* 2005, Liu *et al.* 2005, Fan *et al.* 2006, Benz *et al.* 2007, Vitiello *et al.* 2007). Currently, Watt class (< 10 W) THz frequency QCLs have been produced in laboratory environments, with the QCL cooled to cryogenic temperatures of several tens of Kelvins (Williams *et al.* 2005, Lee *et al.* 2006, Scalari *et al.* 2006, Walther *et al.* 2006, Williams *et al.* 2006), while other more recent work has yielded milliwatt power outputs at room temperature (Belkin *et al.* 2008, Lu *et al.* 2012).

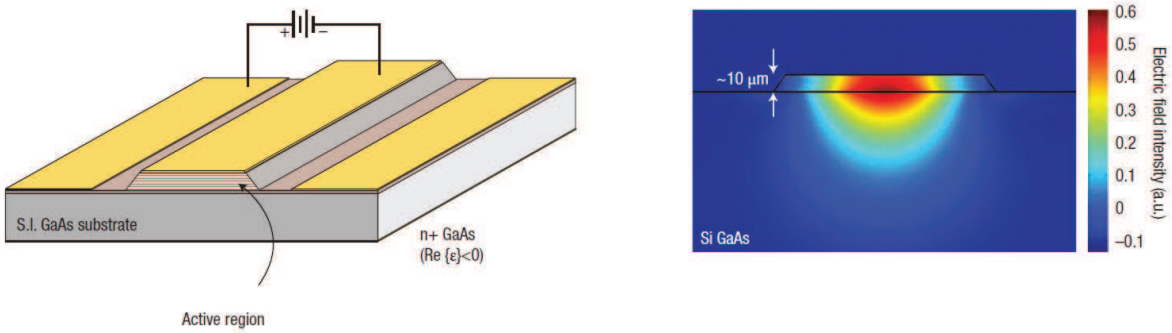

Figure 2.6. Schematic of a QCL waveguide. A schematic of a QCL waveguide used to generate THz radiation. The active region between the top metal and bottom substrate layers produces an intense electric field by the cascading of electrons in the fabricated quantum wells. The emission of the THz radiation then passes through the bottom of the substrate. After Williams (2007).

2.1.6 Other Techniques

Other techniques for THz generation are generally in the high power range of much greater than mWs. These techniques are often high-cost and require large investments in size for generation. Gyrotrons and synchrotrons are such mechanisms for THz generation and both require the use of acceleration of electrons in large magnetic fields. Syncrotrons are also only located in specific parts of the world, with only facility in Australia located in Melbourne, Victoria.

2.2 THz Detection

Terahertz detection techniques may be grouped into direct and indirection methods, with photoconductive sampling and bolometers with associated technologies are able

to directly detect incident THz radiation either by induced current or temperature changes, while indirect methods such as EO sampling and air plasma detection are reliant on detecting the interaction of THz radiation on a probe laser beam.

2.2.1 Photoconductive Sampling

Photoconductive sampling can be described as the inverse process of PCA generation from Section 2.1.1. Instead of applying a bias voltage to accelerate photocarriers generated by a laser pulse across electrodes on the PCA, as in PCA THz generation, detection involves no use of a bias voltage. In PCA detection, the photocarriers are accelerated across the electrodes by incident THz radiation, this creates an induced current that can be measured by an ammeter connected to the electrodes. This induced current is usually very small, generally not more than several microamps and is proportional to the incident THz electric field $E(t)$. As the THz pulse width is in the picosecond range, it is able to sample multiple THz pulses over a time delay τ, which is defined by a connected lock-in amplifier (LIA), as the probe laser pulses have pulse widths of no more than 100 fs. Thus, the photocurrent $j(\tau)$ can be defined by,

$$j(\tau) = e\mu \int_{-\infty}^{\infty} E_{\mathrm{THz}}(t) \cdot N(t-\tau)dt \quad , \tag{2.8}$$

where e is the elementary electric charge, μ is the electron mobility, and $N(t)$ is the photoconductivity (Park *et al.* 1998).

The response of the PCA for detection can be improved to be more sensitive, similarly to PCAs for THz generation. Again, the substrate semiconductor's carrier lifetime is critical to determining the maximum possible detectable bandwidth from a THz pulse, with carrier lifetime being inversely proportional to maximum detectable bandwidth. The distance between the electrodes of the PCA is also a determining factor for both the sensitivity and maximum detectable bandwidth of the PCA. As with PCA emitters, a smaller gap between electrodes yields a higher detectable bandwidth, and as the structure of the PCA is much less than that of wavelengths of the THz range, the PCA can be approximated as an ideal Hertzian dipole. Generally, PCA detectors employ the use of a H structure as shown in Figure 2.7. This structure allows for the direct flow of current from the generated photocarriers across the electrodes in the horizontal arms, as they are tightly spaced. This gap size is usually in the order of a few microns (Jepsen *et al.* 1996).

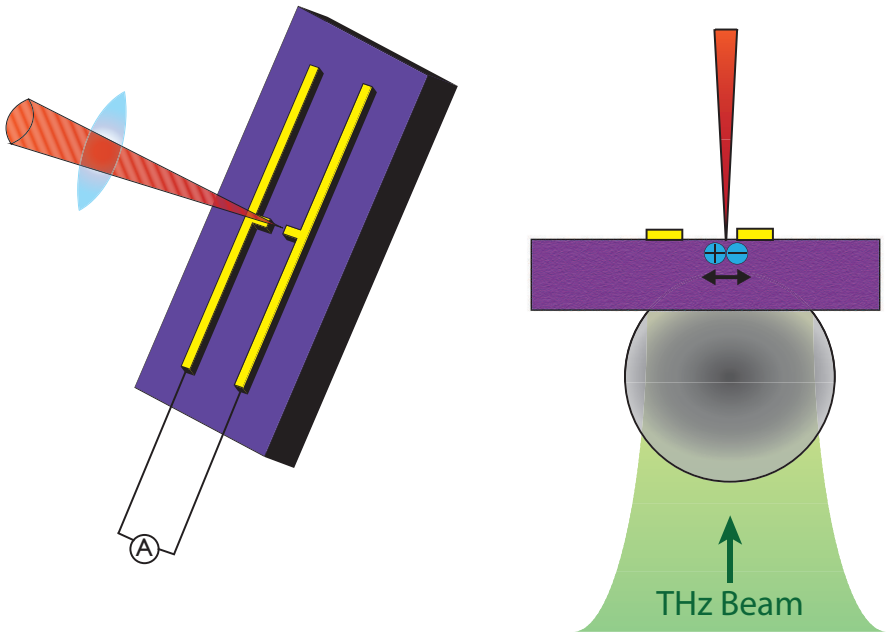

Figure 2.7. Front & side views of PCA detection. The front view (a) depicts an incident focused laser beam onto a H-structure PCA. The laser beam is directed between the two electrodes, which are separated by a few microns and connected to an ammeter. The side view, (b) shows the subsequently generated photocarriers, which are then accelerated by the incident THz electric field coupled by the HiZ Si lens. This induced photocurrent can then be measured by a connected ammeter. The small separation of the electrodes of the H-structure enables the photocurrent to flow more easily between the electrodes, providing a more sensitive response to the incident THz electric field, thus yield higher bandwidths from a better SNR.

2.2.2 EO Detection

Electro Optical (EO) detection is much more complicated to both implement and describe than PCA detection. Essentially, EO detection relies on the Pockels effect, where the refractive index is linearly dependent on an applied electric field and can be described by Equation 2.9. The Pockels effect takes place on the EO detection crystal, where both the probe laser beam and THz pulse are combined. The birefrigence of EO crystal is then changed by the THz electric field, and the polarization of the synchronised probe beam is subsequently rotated from its initial polarization.

$$n = \sqrt{1 + \chi^{(1)} + \chi^{(2)} \cdot \vec{E} + \chi^{(3)} \cdot \vec{E}^2 + \cdots} \quad , \tag{2.9}$$

where, n is the refractive index, $\chi^{(n)}$ is the nth order nonlinear susceptibility tensor, and $\vec{E}$ the nth order optical pulse electric field vector.

To make use of this change in polarization, a quarter-wave plate is used to circularly polarize the probe beam after it passes through the EO crystal. This polarization change causes the horizontal and vertical components of the probe beam to vary, the resultant elliptical polarization from the quarter-wave plate can then be split up into the horizontal P and vertical S polarizations by a Wollaston prism. The P and S polarized beams can then be measured by a pair of balanced photodiodes to detect the change imparted by the THz electric field on the probe beam (Auston and Nuss 1988, Mittleman 2010), the physical setup can be seen in Figure 2.8. The output from the photodiodes is a voltage proportional to the THz electric field strength.

2.2.3 Bolometers, Golay Cells & Pyroelectric Detectors

Bolometers, Golay cells and pyroelectric detectors are all single frequency intensity meters, measuring only power, that operate in a range from infrared to millimetre waves. The single frequency response requires the use of interferometric setups in order to sweep through a range of frequencies. A summary of each detector's advantages and disadvantages is provided in Table 2.3.

Bolometers

The bolometer was invented by Langley in the 1800s (Richards 1994), and be simplified conceptually as a highly sensitive temperature sensor. The concept of a bolometer is based on the change in conductivity of metals as they absorb incident electromagnetic radiation from infrared to millimetre waves, inclusive of THz radiation. The physical construction of a bolometer consists of an absorptive element, which is usually a thin layer of metal, which is able to absorb incident electromagnetic radiation and convert it to heat. This heat is then coupled to a thermal reservoir, which is kept at a constant cryogenic temperature, to aid in the removal of background thermal noise. As the incident radiation heats up the thermal reservoir, this change in temperature can then be measured by an attached thermometer, with the increase in temperature being proportional to the power of the incident electromagnetic radiation. When no incident radiation is present on the bolometer, the thermal reservoir is able to return to its initial temperature at the same rate as the rise in temperature. The rise and fall times of both

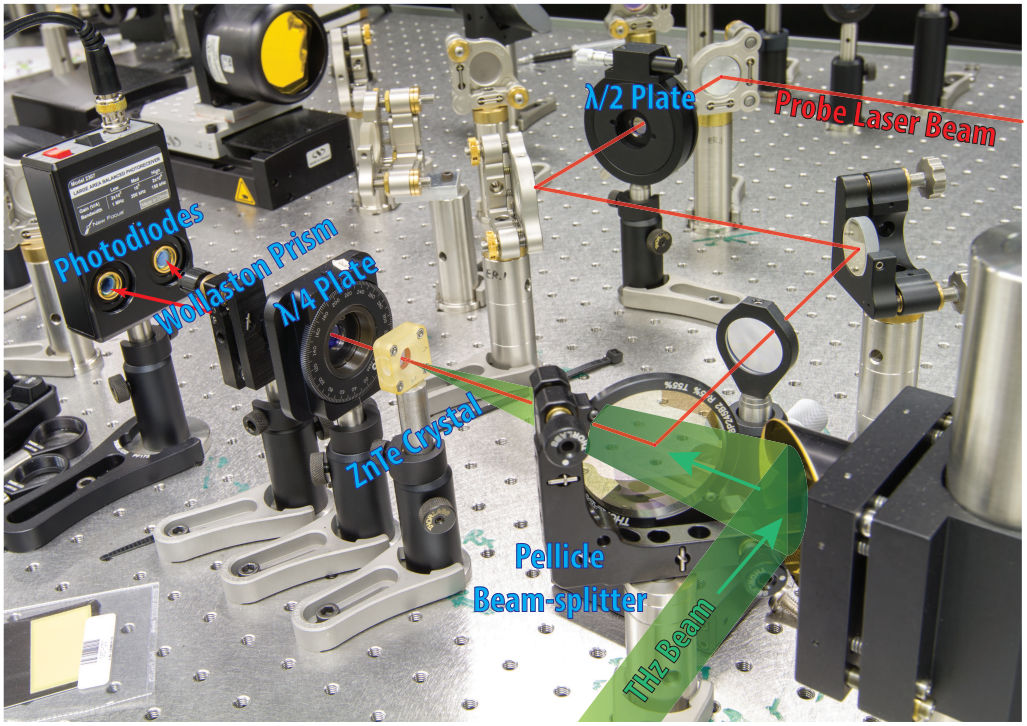

Figure 2.8. Electrooptical detection for THz radiation. A pellicle beam splitter is used to combine the probe laser beam with the incident THz pulse. The pellicle allows the THz beam to pass straight through onto the ZnTe crystal, while the laser beam is reflected to the same position. This causes a change in birefringence of the EO crystal, and through the Pockels effect alters the polarization of the probe laser. The quarter-wave plate then circularly polarizes the laser beam, and is used to zero the offset on the photodiodes when no THz pulse is present. The beam is then split into horizontal and vertical polarizations by the Wollaston prism, whereby the balanced photodiodes can detect a proportional change of polarization exhibited by the THz pulse as a voltage.

the absorber and thermal reservoir can be tuned to frequency band of interest and also optimised for faster response and performance. The major disadvantage of bolometers are that they require the cooling of the thermal reservoir to cryogenic temperatures by either liquid nitrogen or helium, which presents not only higher on-going costs in laboratory use, but also significant safety hazards associated with handling these chemicals. This disadvantage led the development of other devices that are able to measure temperature changes more conveniently at near room temperature. An interferometric setup is also required for bolometers to be able to measure incident power at more than one frequency.

Golay Cells

One such device is the Golay cell, which was originally described by Golay (1947). The principle of the Golay cell follows that of the bolometer, where an absorbing medium is placed in front of incident electromagnetic radiation, however instead of a cryogenically cooled thermal reservoir, the Golay cell ultilises a gas filled cylinder. As the incident radiation heats the absorbing material, the heat is transferred to the gas cylinder, which in turn increases the pressure of the contained gas. As the cylinder is attached to a mirror, its angle is changed yielding a change in response from an optical system measuring this change in angle, which is again directly proportional to the power of the incident radiation (Richards 1994). The Golay cell enables room temperature measurements similar to a bolometer, but is highly susceptible to seismic movements, as measurements are based on the small changes in angle of the mirror attached to the gas cylinder.

Pyroelectric Detectors

Another technology similar to both bolometers and Golay cells is the pyroelectric detector. Pyroelectric detectors operate from the basis that certain crystalline substances are able to generate transient voltages when heated or cooled (Richards 1994, Webster 1999). Again, as with bolometers and Golay cells, the pyroelectric detector contains an absorbing medium for incident electromagnetic radiation. However, in this case the absorbing medium is a crystalline substance that responds to temperature by altering the positions of atoms in its structure. This results in a transient voltage generated across the crystal due change in dielectric constant. The absorbing medium is attached to a voltage biased capacitor, and a change in current can be measured proportional to the power of the incident radiation. Many new materials are being developed to provide a faster response (Webster 1999), as the main disadvantage of a pyroelectric detector is its slow response in detection.

2.2.4 Air Plasma Detection

Air plasma detection, just like air plasma generation from Section 2.1.4 is the latest current detection technique used in THz-TDS. Air plasma detection is also a complex optical process, much the same as air plasma generation. Again, an amplified Ti:Sapphire laser is necessary to implement this detection method. Clough *et al.* was the first to

Detector	Advantages	Disadvantages
Bolometers	Fast response, well established & high accuracy	Requires cryogenic cooling
Golay Cells	Fast response & room temperature operation	Very sensitive to vibrations
Pyroelectric Detectors	Relatively inexpensive & room temperature operation	Slow response time

Table 2.3. Advantages & disadvantages of thermophile detectors. A summary of the advantages and disadvantages of various thermophile based single frequency detectors.

implement such a technique in an all air plasma THz-TDS system (Clough *et al.* 2011), the schematic for this system can be seen in Figure 2.9. The process of detection relies on a probe plasma generated coherently in the detection path to produce a plasma fluorescence with the encoded THz spectroscopic information present. A phase compensator is also required in the probe path to control the relative phase between both the fundamental 800 nm pulse and the second-harmonic 400 nm pulse. When both the probe laser pulses and generated THz pulse are refocused together after the sample, a second detection air plasma is generated, giving off a plasma fluorescence retaining the spectroscopic information of the sample. This can then be detected with a tuned photomultiplier tube, which will decode the spectroscopic information from the plasma fluorescence. Currently, this detection scheme is limited by a lower SNR to other detection techniques of one order of magnitude, meaning that more averages are required per scan to achieve the same SNR for TDS (Clough *et al.* 2011).

2.3 Chapter Summary

Generation and detection techniques for THz radiation have been described in detail in this Chapter, particularly techniques designed for low-power systems pumped by a non-amplified laser source. These generation and detection techniques are essential to implementation of time-domain spectroscopy systems discussed in Chapter 3.

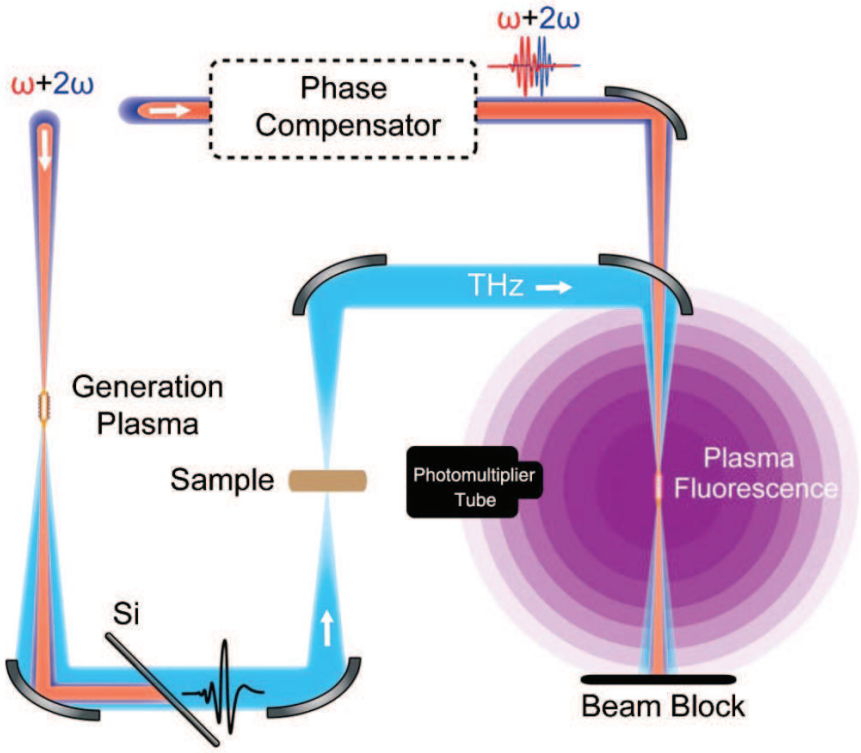

Figure 2.9. Schematic of an all air plasma THz-TDS system. The red and darker blue lines depict the 800 nm and 400 nm fundamental and second-harmonic laser pulses respectively, while the light blue shows the generated THz beam. A phase compensator is used in the probe path, to control the relative phase between the 800 nm and 400 nm laser pulses, while a photomultiplier is used to monitor the coherently encoded THz spectroscopic information in the probe plasma, shown as the plasma fluorescence in purple. After Clough *et al.* (2011).

Chapter 3

Terahertz Time-Domain Spectroscopy

TERAHERTZ time-domain spectroscopy opens many possibilities for characterising materials. In particular, a growing area of interest is the measurement of metamaterials within this frequency range, which may lead to faster and easier characterisation of absorptive liquids, and samples with non-unity permittivities and permeabilities. This Chapter follows on from Chapter 2 and details the optical setups necessary to perform THz-TDS in both transmission and reflection geometries using a low-power laser source to generate pulsed THz radiation. In addition to this, the design, implementation and characterisation of a novel simultaneous reflection and transmission system is presented.

3.1 THz-TDS Systems

Terahertz time-domain spectroscopy systems can be separated into either transmission or reflection mode based systems. In transmission mode, THz radiation incident on a sample will pass through it, while in a reflection mode based system, the incident THz radiation will reflect off the surface of the sample. Both these types of systems have advantages and disadvantages for measuring differing types of samples. Transmission geometry systems are typically easier to setup and configure than reflection mode systems, which are slightly more complicated in alignment and configuration. Transmission measurements are useful for samples that have low absorption, are non-metallic, and non-ionic. On the other hand, reflection geometry based systems are useful for measuring liquids, reflective samples and also samples with higher absorption, which are difficult to measure in transmission mode.

Both transmission and reflection mode THz-TDS systems share many common components, which are necessary to build a functional setup. These include: (i) a pump laser source to power the system, (ii) an emitter to generate the THz radiation, (iii) a detector to detect the transmitted or reflected THz radiation from a sample, (iv) focusing optics to focus the THz radiation, (v) an optical delay stage to create a time delay between the optical paths to the emitter and detector to sweep through the generated THz radiation pulse, (vi) a modulation source for the emitter, which can either be optical or voltage based, (vii) a lock-in amplifier to recover the generated THz signal from the detector and (viii) finally a computer with customised software to acquire the data from the lock-in amplifier and synchronise it with the movement of the optical delay stage. This computer also controls the movement of the optical delay stage.

The following sections discuss in detail the setups for transmission and reflection mode based THz-TDS systems, and a novel system that incorporates both transmission and reflection geometries into a singular setup that is able to simultaneously acquire data from two separate detectors placed in transmission and reflection modes.

3.1.1 THz-TDS Transmission Mode Systems

Transmission mode THz-TDS systems are generally the most common type of system in many laboratories, as they are generally easier to setup than reflection mode systems. Transmission mode systems also offer easier alignment of various emitters and detectors discussed in Chapter 2. This enables many configurations of transmission mode

systems to be setup for customised purposes. For instance, the simplest arrangement involves using two PCAs as an emitter and detector, which forms the basis for many systems, in particular in commercially available systems from both Menlo Systems and Picometrix. The arrangement of a transmission mode system employing the use of two PCAs can be seen in Figure 3.1.

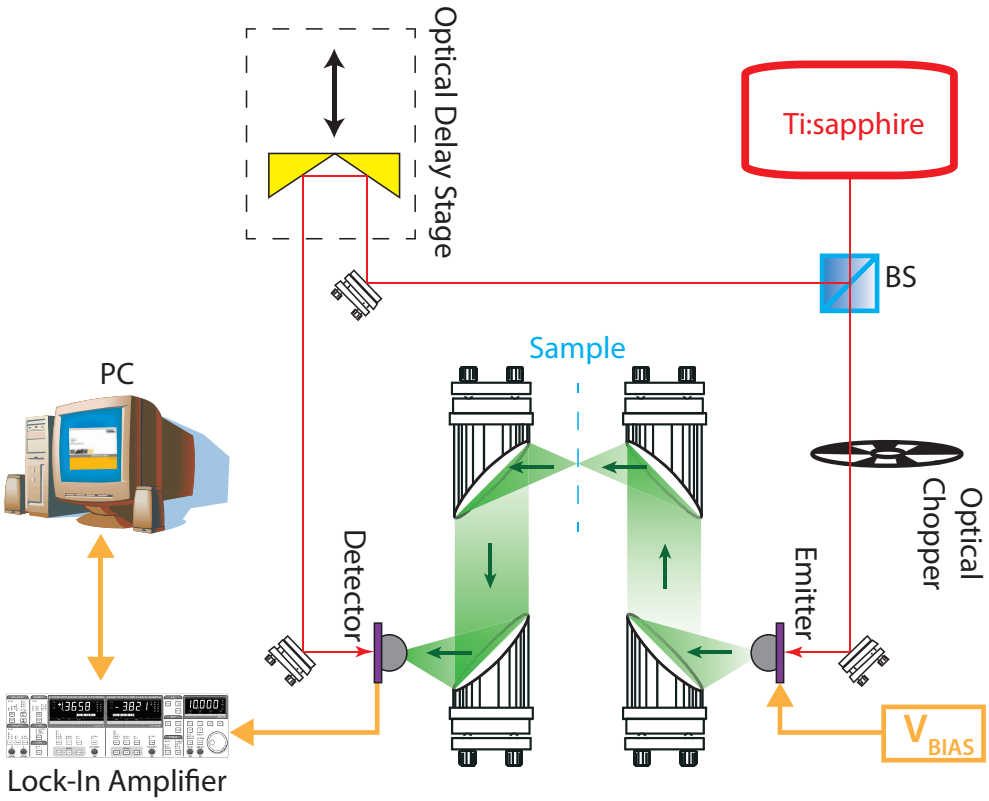

Figure 3.1. A PCA based emitter & detector transmission mode THz-TDS system. An illustration of the simplest transmission mode THz-TDS setup utilizing two PCAs as an emitter and detector, respectively. This type of setup mirrors that of commercially available THz-TDS systems.

An alternative to using PCA detection as previously mentioned, is to employ EO detection techniques as described in Section 2.2.2. This requires a slightly more complex design than in Figure 3.1, but has an added advantage of not being limited in bandwidth in terms of the carrier lifetime of the PCA's substrate material, thus offering more sensitivity and a higher bandwidth from measurements. Figure 3.2 shows the layout required to building a transmission mode system with an EO detector.

In both presented systems, it is possible to replace the PCA emitter with other alternative THz emitters to change the properties and characteristics of the system, with

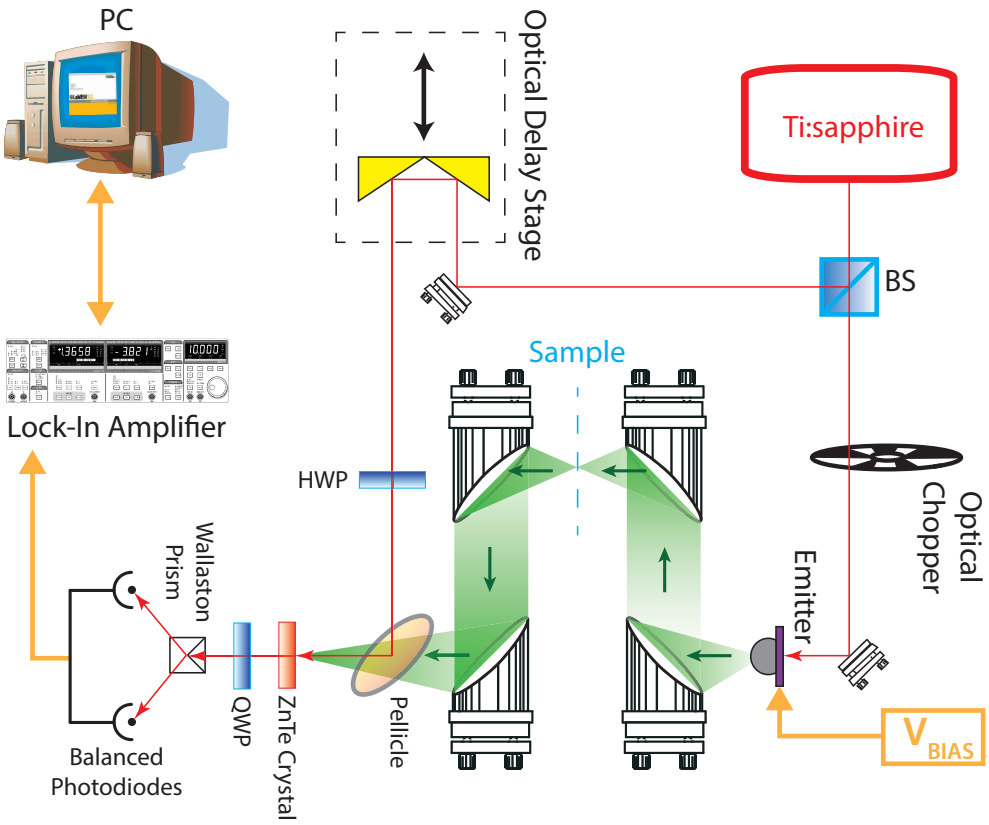

Figure 3.2. A PCA based emitter & EO detector based transmission mode THz-TDS system. An illustration of a PCA emitter and EO detection based THz-TDS system. The emitter used here can be changed to another source with little to no modifications to the optical setup of the system. The use of EO detection in this system adds slight complexity to the overall setup, but has the added advantage of not being bandwidth limited due to the carrier lifetime of a PCA detector. The physical setup of the detector can be seen in Figure 2.8.

little to no changes to the optical setup. The alignment of the pump laser does not require any realignment as the generated THz radiation follows colinearly. An alternate focussing lens is necessary to focus the pump laser beam with a high enough intensity on the EO crystal, which requires minimal effort to replace and realign.

3.1.2 THz-TDS Reflection Mode Systems

Reflection mode THz-TDS systems are slightly more complex than transmission mode systems, due to the need for either a silicon dove prism used in Attenuated Total Reflection (ATR) systems (Sakai 2005), a silicon beam splitter used in conjunction with off-axis parabolic mirrors (Rønne *et al.* 1997) or elliptical mirrors (Fischer 2005) used

in more general reflection mode systems, which can be seen in Figures 3.3, 3.4 & 3.5 respectively. With transmission mode systems discussed in the previous section, various emitters and detectors can be used in reflection mode systems to suit different purposes and applications.

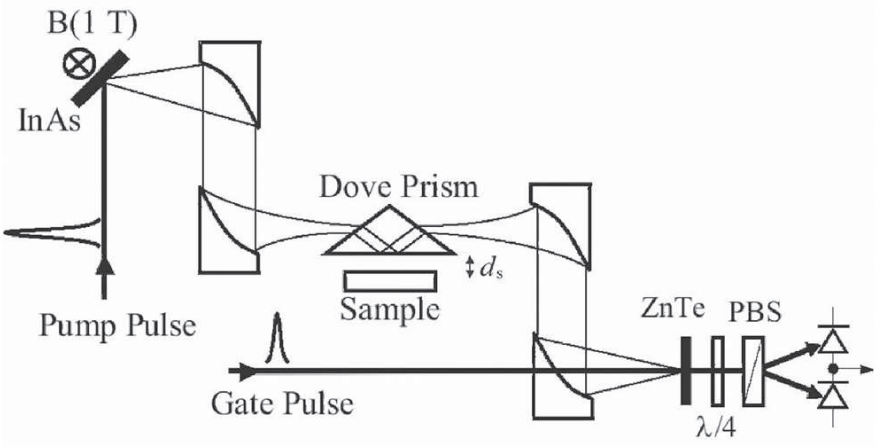

Figure 3.3. A reflection mode THz-TDS using a silicon prism in ATR. A transmission mode THz-TDS system converted to a reflection ATR mode system using a silicon dove prism. A sample is placed onto the prism to perform measurements. Reference measurements are performed likewise with a mirror used instead. After Sakai (2005).

3.1.3 Calculating Refractive Index from THz-TDS

As both transmission and reflection mode THz-TDS systems capture a time-domain representation of an electric field, it is possible to determine the complex refractive index ($\tilde{n} = n + i\kappa$) and absorption of samples from a reference measurement and a sample measurement. It is common to model the electrical field passing through the sample as a plane wave propagating in space along the z-direction as,

$$E(z,t) = E_0(t) \cdot \exp[iz \cdot \frac{n\omega}{c}] \cdot \exp[-z \cdot \frac{\kappa\omega}{c}] \quad , \tag{3.1}$$

where $E_0(t)$ is the amplitude of the electric field, z the direction of propagation, ω the angular frequency, c the speed of light and n and κ the real and imaginary parts of the complex refractive index $\tilde{n}$.

Two measurements are required to extract the required data necessary for determining refractive index and the absorption coefficient of samples. These two measurements

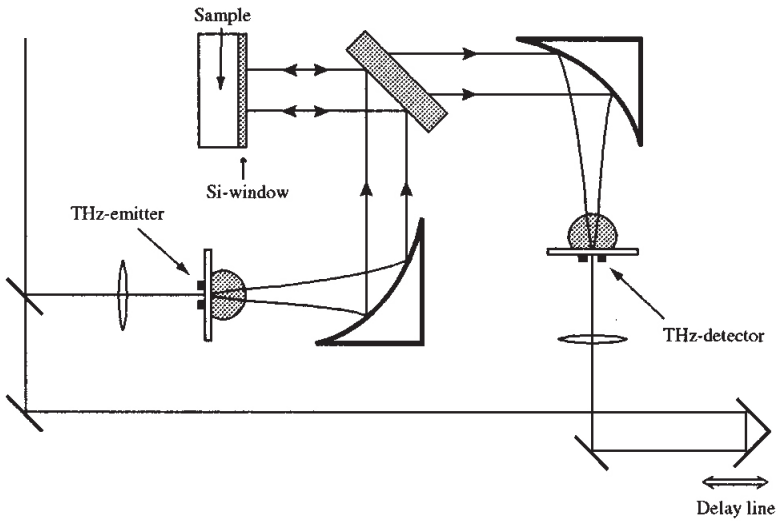

Figure 3.4. A reflection mode THz-TDS using a silicon beam splitter. A reflection mode THz-TDS system built using off-axis parabolic mirrors and a silicon beam splitter. Reference and sample spectra are recorded from normal incident radiation reflecting from the surface of a mirror and the sample respectively. After Rønne *et al.* (1997). Note that in this case, 50% of the emitted THz power is lost from transmission through the silicon beam splitter.

include a reference measurement $E_{\text{ref}}(t)$ and a sample measurement $E_{\text{sam}}(t)$. Generally, the reference measurement is free space for transmission mode measurements, while a mirror in free space, which is assumed to be a perfect reflector is used in reflection measurements. However, if the sample is a mixture or layers of components, then the reference must carefully be selected, such that the sample measurement is singled out from the other components of the mixture or layers.

Examples where the reference may not be simply an atmospheric measurement are samples that are fabricated on top of a substrate. These may include a plastic structure fabricated on top of a silicon wafer. In this case, the plastic structure is being investigated and thus should be clearly seperated from the substrate silcion layer, therefore the reference measurement should be a blank silicon wafer without the plastic structure, while the sample measurement remains the same.

As the refractive index and absorption are frequency dependent, the electric field data from both the reference and sample need to be considered in the frequency domain.

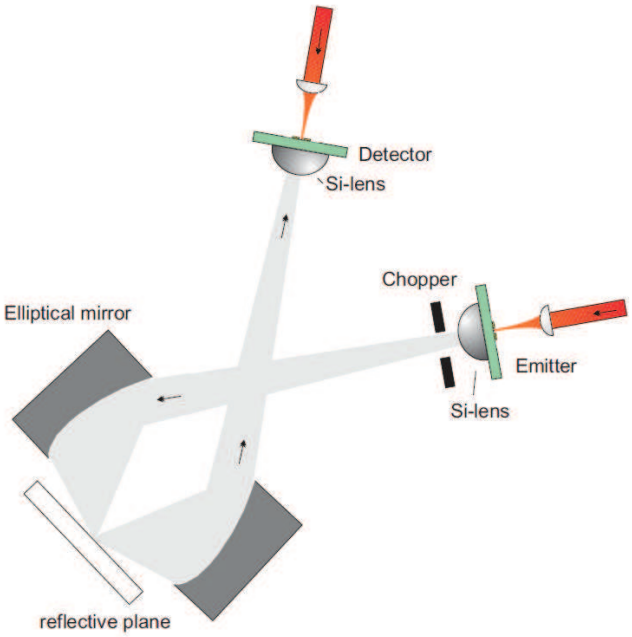

Figure 3.5. A reflection mode THz-TDS using elliptical mirrors. A simple setup of a reflection mode THz-TDS system using elliptical mirrors. These elliptical mirrors require customised machining and high accuracy to enable tight focusing of the THz beam. Measurements of reference and sample data is performed by placing a mirror or sample at the reflective plane. After Fischer (2005).

Therefore, the reflected and transmitted amplitudes from measurements can be determined as,

$$R(\omega) = \frac{E_{\text{sam,rx}}(\omega)}{E_{\text{ref,rx}}(\omega)} \tag{3.2}$$

and,

$$T(\omega) = \frac{E_{\text{sam,tx}}(\omega)}{E_{\text{ref,tx}}(\omega)} \quad , \tag{3.3}$$

where $E_{\text{ref,rx}}(\omega)$, $E_{\text{ref,tx}}(\omega)$, $E_{\text{sam,rx}}(\omega)$ and $E_{\text{sam,tx}}(\omega)$ are the Fourier transforms of reference and sample waveforms in reflection and transmission, respectively.

These equations can then be used to calculate the complex refractive index $\tilde{n}(\omega) = n(\omega) + i\kappa(\omega)$, provided that measurements are performed normal incidence, as well as the absorption coefficient $\alpha(\omega) = 4\pi\kappa(\omega)/c$ (Sakai 2005), by the following equations,

$$R(\omega) = \frac{1-\tilde{n}(\omega)}{1+\tilde{n}(\omega)} + \frac{\frac{4\tilde{n}(\omega)[\tilde{n}(\omega)-1]}{(\tilde{n}(\omega)+1)^3} \cdot \exp[-i2\tilde{n}(\omega)\frac{\omega}{c}d]}{1-(\frac{\tilde{n}(\omega)-1}{\tilde{n}(\omega)+1})^2 \cdot \exp[-i2\tilde{n}(\omega)\frac{\omega}{c}d]} \tag{3.4}$$

and

$$T(\omega) = \frac{4\tilde{n}(\omega)}{[\tilde{n}(\omega)+1]^2} \cdot \frac{\exp\left\{-i[\tilde{n}(\omega)-1]\frac{\omega}{c}d\right\}}{1-(\frac{\tilde{n}(\omega)-1}{\tilde{n}(\omega)+1})^2 \cdot \exp[-i2\tilde{n}(\omega)\frac{\omega}{c}d]} \quad , \tag{3.5}$$

where c is the speed of light, and d is the thickness of the sample.

For measurements taken where the sample is not placed at normal incidence to the beam, these equations become more complex with cosine terms added to the equation and will not be covered here. For further reading, Sakai (2005) provides insight into these calculations.

3.2 Dual-Mode THz-TDS System

3.2.1 Motivation

Terahertz TDS systems in table-top environments have seen many improvements in both generated power and detectable bandwidth (Sun *et al.* 1995, van Exter and Grischkowsky 1990b, Auston and Nuss 1988, Hangyo *et al.* 2002). These systems allow for the study of many materials and fabricated samples in either transmission (van Exter and Grischkowsky 1990a, Exter *et al.* 1989, Nashima *et al.* 2001b) or reflection modes (Jeon and Grischkowsky 1998, Rønne *et al.* 1997, Jepsen *et al.* 2007). Some samples, particularly metamaterials with a magnetic response, i.e., where the permeability is not equal to unity, require both transmission and reflection measurements to determine the intrinsic electric and magnetic parameters (Starr *et al.* 2004). The new system in this Section overcomes this limitation by simultaneously acquiring both reflection and transmission spectra. Additionally, experimental errors due to sample placement and transfers are therefore avoided leading to reduced experimentation times and lower measurement uncertainty (Withayachumnankul *et al.* 2008).

Previous systems operating in transmission mode typically make use of off-axis parabolic mirrors to collimate and focus a THz beam. By contrast, a typical reflection mode system consists of elliptical mirrors placed at an inclined angle, to reflect a THz beam onto and from the sample surface for spectroscopic acquisition. Other reflection geometry systems employ a silicon beam splitter with off-axis parabolic mirrors

to obtain similar results via a normal incident beam. Brunner *et al.* (2009) have published an innovative system, which is able to acquire both transmission and reflection measurements simultaneously.

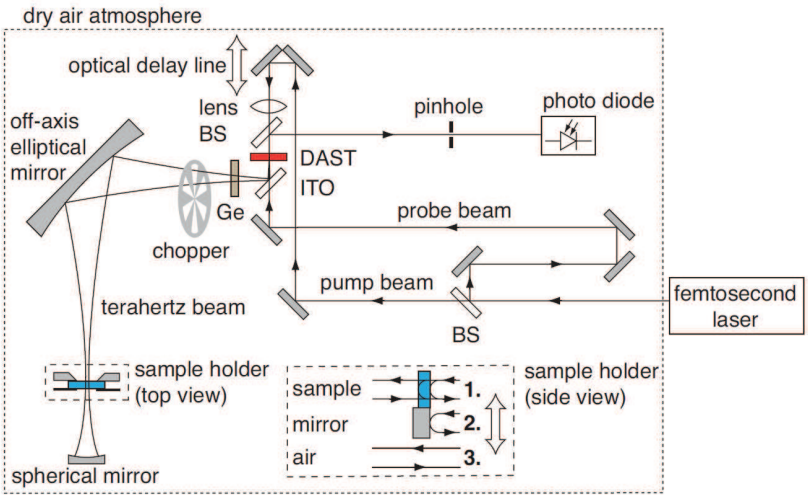

Figure 3.6. A previous design of a dual transmission and reflection THz-TDS system. This system is an innovative design, which minimises phase errors in reflection measurements. Transmission measurements require a double pass through samples, which complicates calculations slightly and attenuates the THz signal. After Brunner *et al.* (2009).

The system presented in this Section integrates the off-axis parabolic mirror concept from traditional THz-TDS transmission mode systems, with an additional silicon beam splitter placed in the back-reflected path for reflection measurements. This work takes a different approach from Brunner *et al.* (2009), as there are no limitations on the emitters or detectors used in the system. Our system does not rely on an EO crystal used as a transceiver and it only requires a single pass through samples, simplifying calculations for refractive index and absorption. The only draw back to our system is the dumping of 50% of the emitted terahertz power, but despite this drawback with currently available emitters the system still yields a very usable SNR. In addition, the system setup is simplified as it only requires three additional components to the conventional transmission system, namely; a silicon beam splitter, an additional off-axis parabolic mirror and an additional terahertz detector for the reflected beam.

To verify the system characteristics, two samples are measured. These include a high-impedance (HiZ) float-zone silicon wafer and an n-type (phosphorous doped) silicon wafer. Measurements of the float-zone silicon wafer, provide a transmittance and reflectance that can be verified by a Fabry-Pérot analytical model (Heavens 1955), with

a previously calculated refractive index. In addition, measurements of the n-type silicon wafer allow for further verification of system performance comparing the Drude model with the measured data.

3.2.2 Experimental Setup

The experimental setup of the simultaneous reflection and transmission THz-TDS system has many similarities to transmission mode setups described in Section 3.1, where four off-axis parabolic mirrors are used within the THz beam path to focus the beam onto a sample. In addition to this configuration, a float-zone intrinsic silicon wafer of 380 μm thickness is used as a beam splitter for the back-reflected path and coupled for measurement with an additional off-axis parabolic mirror. A Ti:Sapphire Spectra Physics Mai Tai laser with a center wavelength of 800 nm and a pulse length of $\leq$ 100 fs is used as the pump source, while a Gigaoptics Tera-SED large area inter-digitated array emitter is used as the THz emitter biased with a $\pm$10 V square-wave with a chopping frequency of 10 kHz. As can be seen in Figure 3.7, the emitter does not have a silicon lens present, as the array structure collimates the emitted THz beam. The detectors used for the measuring of the transmitted and reflected THz beams are Menlo Systems TERA8-1 H-dipole based photoconductive antennas, coupled with Tydex 10 mm diameter hyper-hemispherical lenses to collect the THz beam onto the antenna. Two Stanford Instruments SR-830 lock-in amplifiers are used to recover the induced current for the detectors and allow for simultaneous data acquisition. An illustration of the system setup can be seen in Figure 3.7, while a photograph of the physically realized system can be seen in Figure 3.8.

All experiments are performed at ambient temperature in dry atmospheric conditions. Two reference measurements are initially required for comparison with sample data acquired from transmission and reflection geometries. To minimize errors due to the shift in reference or sample position in a reflection geometry, a fixed CCD camera is placed over the focal point of the terahertz beam. This allows both the sample and mirror surfaces to be placed in the same longitudinal position, within a micron accuracy. This enables the refractive index and absorption calculated in reflection mode to be accurately compared with that calculated from transmission mode measurements, and conforms with the acceptable range of error in literature (Sakai 2005, Nashima *et al.* 2001a). An optical-grade gold mirror is employed in the reference measurements in a reflection geometry and reflects more than 98% of the terahertz beam in the reference measurement.

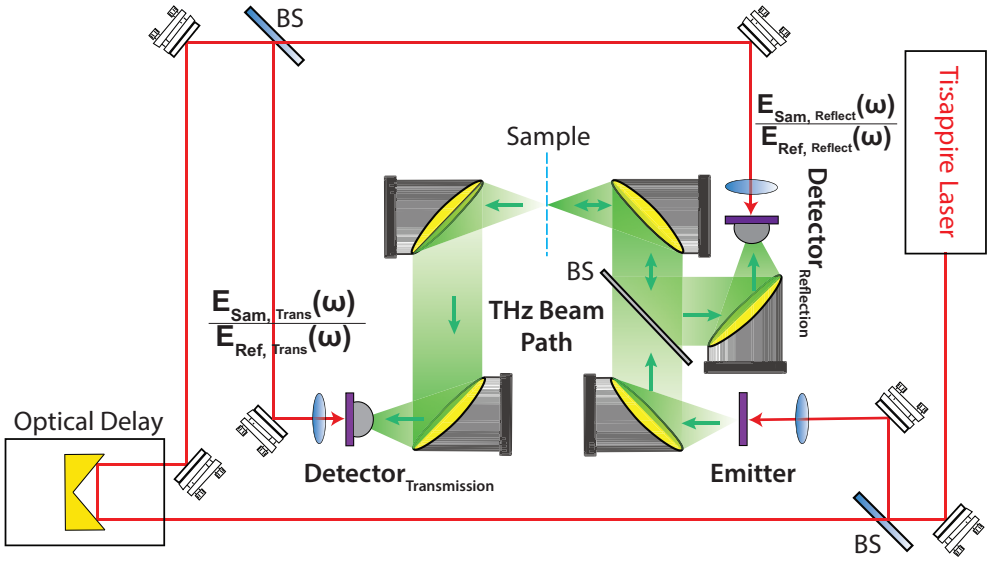

Figure 3.7. Schematic of the dual system. An illustration of the simultaneous reflection & transmission THz-TDS system. The path of the 800 nm laser beam is depicted in red, while the THz beam path is shown in green, with all beams horizontally polarized. The sample is placed in the focus of the parabolic mirrors, and for a reference measurement in reflection geometry, a mirror is used.

It is assumed that the losses are negligible and within experimental error of measurements. Each measurement is conducted over an average of 5 scans, with an integration time at each data point of 100 ms set on the lock-in amplifier over 1024 steps on the optical delay stage.

3.3 Results & Verification

Reference measurements of the system in both reflection and transmission mode show the system performed within expectation, where the silicon beam splitter reflects off approximately 50% of the generated power. The Fourier transform of the reference in reflection mode, $E_{\mathrm{ref,rx}}(\omega)$ is acquired by placing a mirror surface at the point of focus of the parabolic mirrors, while the transmission reference, $E_{\mathrm{ref,tx}}(\omega)$ is obtained without obstructing the THz beam path, apart from the silicon beam splitter, as outlined in Figure 3.7. To determine the loss of the system, a transmission reference is recorded, and subtracted from a measurement in transmission mode without the silicon beam splitter. This conforms to expectations that approximately 50% of the generated power is dumped by the silicon beam splitter. The reference spectra shows that bandwidths of approximately 3 THz are achievable in both geometries. Figures 3.9 & 3.10 show the

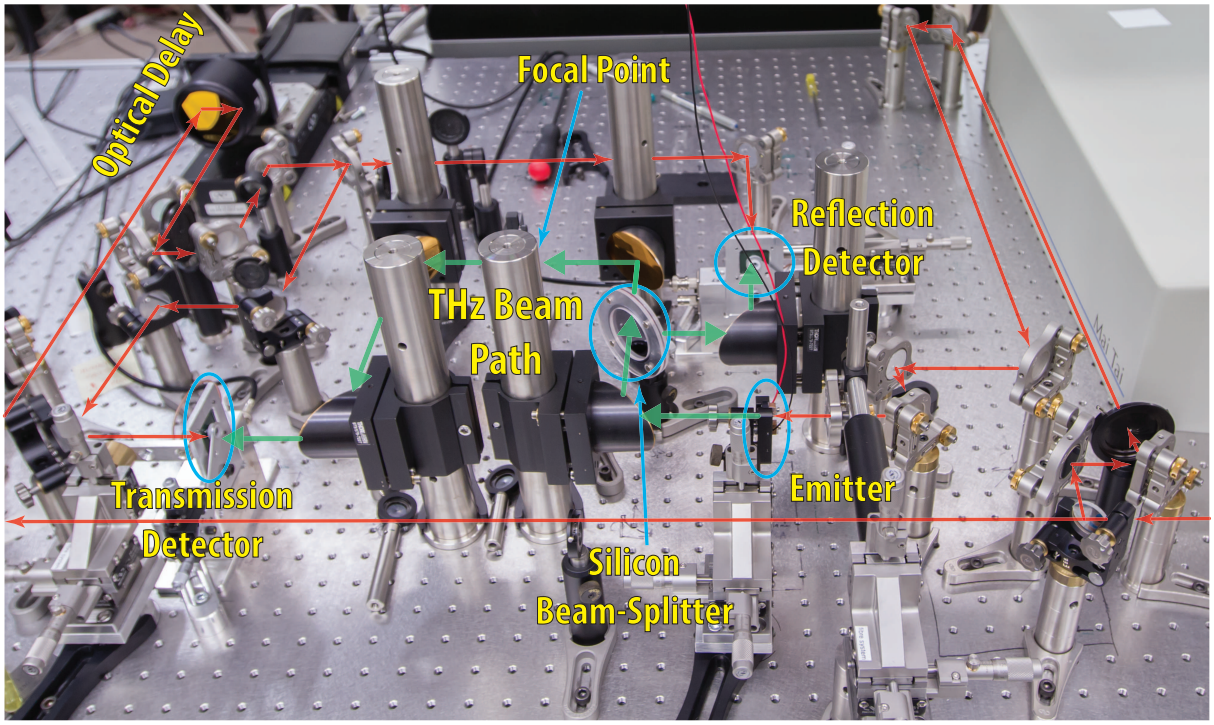

Figure 3.8. Photograph of the dual system setup. A photograph of the physical setup setup. The emitter and detectors for the transmitted and reflected THz beams are circled in blue, along with the silicon beam splitter. The laser and THz beam paths are shown in red and green respectively.

time-domain waveforms and spectra of both the reflection and transmission reference measurements.

The spectra of samples in both reflection and transmission can also be obtained in the same fashion, with the reflected waveform obtained by the reflected pulse, $E_{\text{ref,rx}}(\omega)$ from the sample surface and the transmitted spectra from the transmission through the sample, $E_{\text{sam,tx}}(\omega)$. Thus, the relative reflection and transmission spectra of the sample with respect to the reference can be determined by Equations 3.2 & 3.3. The refractive index and absorption coefficient can then be calculated using Equations 3.4 & 3.5, as outlined in Section 3.1.3.

Characterization of Float-zone Silicon

For verification that the spectroscopic data obtained from both detectors are accurate, a float-zone silicon wafer is measured, as it provides a known transmittance and reflectance from a pre-calculated refractive index of $n_{\text{silicon}} \approx 3.418$. From this

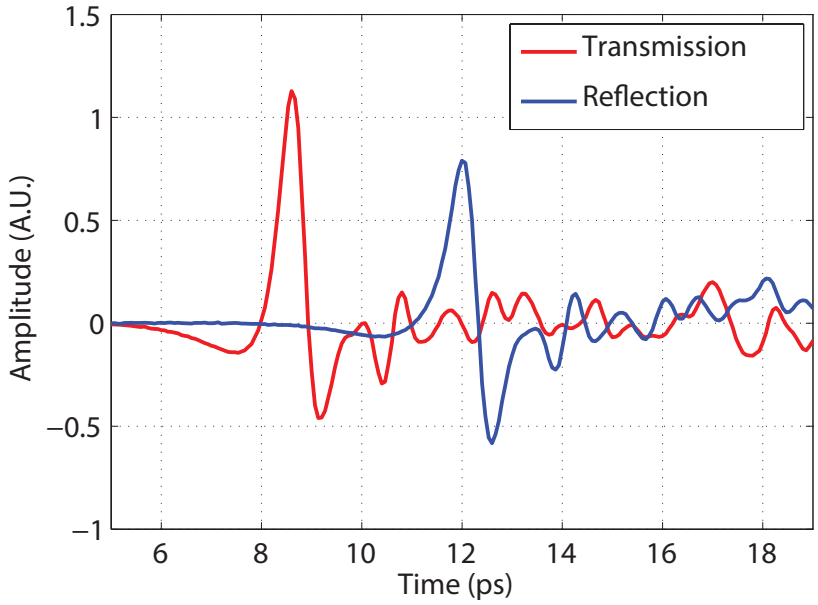

Figure 3.9. Time-domain pulses from the dual system. Time-domain representation of the measured air reference pulses. The red line shows the transmitted pulse, while the blue line shows the reflected pulse. The fluctuations after the main pulse are due to the water vapor present in the laboratory atmosphere. The pulses are offset for viewing ease.

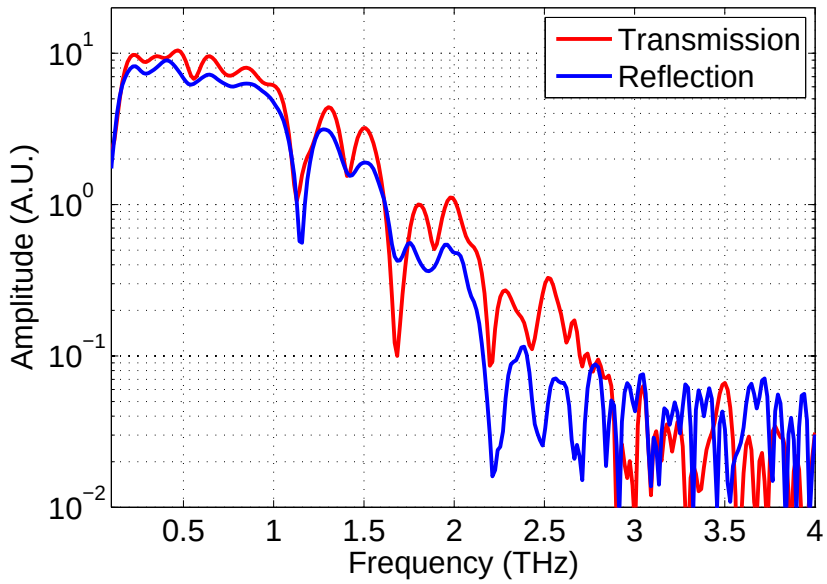

Figure 3.10. Frequency spectra from the dual system. Frequency spectra of the transmitted and reflected air reference pulses of in red and blue respectively. The maximum bandwidth achievable from this system in both reflection and transmission modes is approximately 3 THz. Water absorption can be clearly seen at approximately 1.1, 1.6 and 2.2 THz, as the measurements are conducted in a laboratory air environment.

refractive index, the transmission and reflection spectra can be calculated from standard Fabry-Pérot equations and their corresponding Fresnel coefficients given in Equations. 3.4 & 3.5 (Heavens 1955, Sakai 2005). As can be seen in Figures. 3.11 (a, b), the theoretical model is in good agreement with the measured data. The calculated thickness of the wafer is found to be 1052 μm, by varying the thickness until the modeled curves overlapped the measured data. This value differs slightly from the manufacturer quoted thickness of 1 mm. The good agreement between the theoretical model and the measured data shows that the system is operating as expected. Furthermore, the obtained transmission and reflection magnitudes in some instances are higher than unity due to long term laser drift in measurements (Withayachumnankul *et al.* 2008), which cannot be removed by averaging.

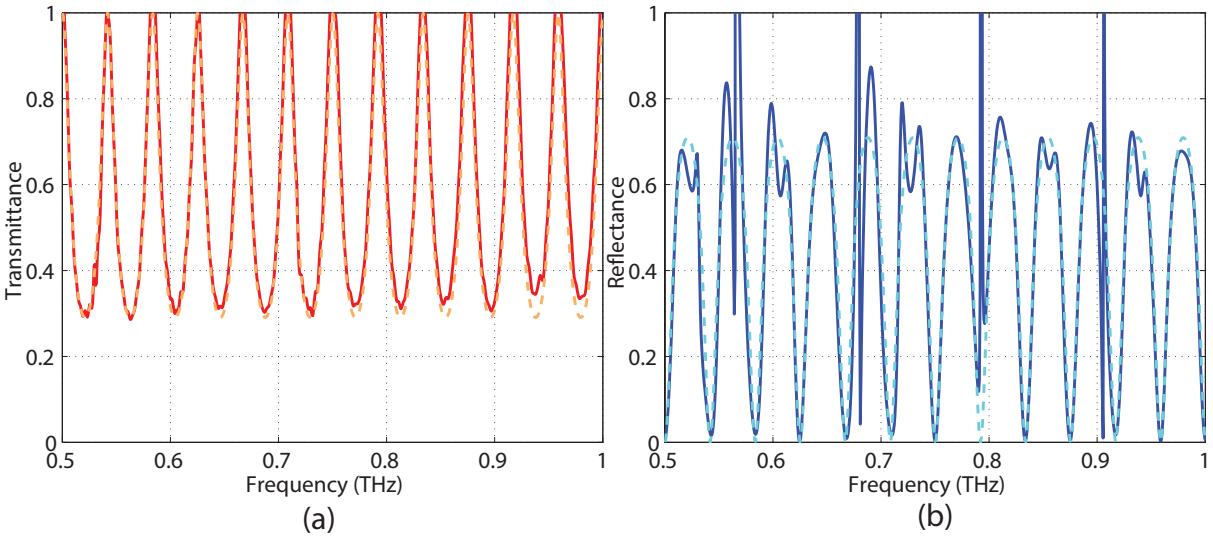

Figure 3.11. Transmitted and reflected spectra from a float-zone silicon wafer. (a) Transmitted & (b) Reflected terahertz power of a 1052 μm thick float-zone silicon wafer. The dotted lines denote the theoretical Fabry-Pérot model, while the solid lines show the measured data. It should be noted that the data in some instances differ slightly from the theoretical model due to laser drift. The figures have been limited to frequencies 0.5 to 1 THz for easier reading.

Characterization of Doped Semiconductor

In the literature, THz characterization of semiconductors (Jin *et al.* 2006, Piesiewicz *et al.* 2007, Grischkowsky *et al.* 1990, Zhang *et al.* 2003, Zhao *et al.* 2002a) is well-known, and this potentially benefits from our dual-mode system. To show this aspect of the system, a phosphorous-doped n-type silicon wafer of thickness 270 μm is measured in

this system for further verification. The spectra are presented in Figure 3.12, where it is possible to see that little to no transmission was measurable, and that most of the power is in fact reflected or absorbed in the wafer. The downward trend in reflectance is due to the increase in frequencies approaching the plasma frequency of the highly doped wafer, where the wafer becomes transparent due to the transition from metal to dielectric.

It is possible to characterize this n-doped silicon wafer to determine the intrinsic values of the carrier concentration and electron mobility. The measured transmission and reflection spectra are fitted with the calculation based on the Drude model, as depicted by the dashed curves in Figure 3.12. The plasma frequency and collision frequency of this silicon sample are determined by curve fitting the data, to be $\omega_p/2\pi = 7.87$ THz and $\Gamma/2\pi = 11.21$ THz, respectively. This is equivalent to the doping concentration of 2.0×10^{17} cm^{-3}, the electron mobility of 603 cm^2/V·s, and the DC conductivity of 0.05 Ω·cm, well within the range specified by the manufacturer.

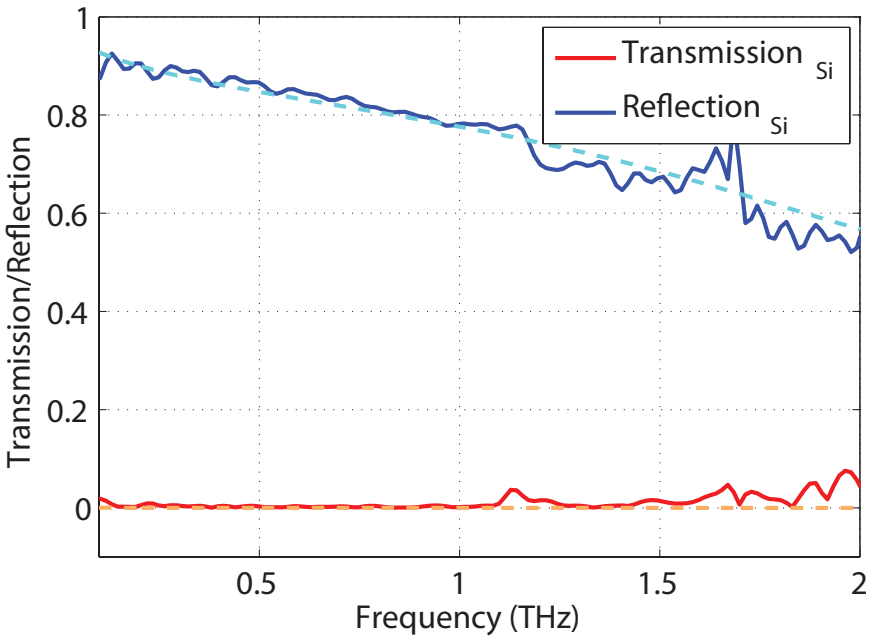

Figure 3.12. Transmitted and reflected spectra from a highly doped silicon wafer. The reflection and transmission spectra of a highly doped n-type silicon wafer. The transmission of the wafer plotted in red is close to zero, while the blue plot shows that wafer to be mostly reflective, with decreasing reflection until the plasma frequency of 7.87 THz is reached. The dotted lines show the modeled curves of the silicon wafer for transmission and reflection respectively in cyan and orange.

3.4 Chapter Summary

Terahertz TDS offers the ability to characterize materials by extraction of refractive index and absorption coefficients through measurements in systems in both transmission and reflection modes. A new original contribution of a system that is able to perform both transmission and reflection mode measurements simultaneously is presented, and will aid characterisation of materials that have permitivities or permeabilities that are non-unity values. Added benefits of this new design are a decrease in measurement times by capturing both the transmission and reflection measurements of samples simultaneously and reduced noise in measurements, as the sample does not need to be moved.

This new system does however have a limitation, similar to that of reflection mode systems where a silicon beam splitter is used. This presents a number of problems common to all beam splitters in the THz range of frequencies. Techniques to address these problems will be discussed in Chapters 4 & 5.

Chapter 4

Terahertz Beam Splitters

THE previous Chapter showed the development of a simultaneous dual scanning THz-TDS system and reflection mode based THz-TDS systems, which require a silicon beam splitter to capture data. This Chapter details a low-cost ultra-thin broadband THz beam splitter based on a thin conductive layer, as an improvement over the existing current state of the art. This newly developed beam splitter along with the development of ever increasing generated power in THz systems enables flexible usage of available power, particularly with the ability to create any desired splitting ratio via rapid prototyping.

4.1 Conventional Beam Splitters

Conventional beam splitters in the optical range are well understood and are commonly available, off the shelf items with various splitting ratios available. These splitting ratios of reflection to transmission commonly range from 10:90, 30:70, 50:50, 70:30 to 90:10, however other ratios can be manufactured accordingly. Optical beam splitters are generally low-loss and operate from the infrared to visible and ultra-violet ranges, but require specific dielectric coatings for each range due to the reliance on $\lambda/4$ wavelength interference to enable accurate adjustment of splitting ratios. This dielectric coating is applied on a base substrate, usually silica, which if too thick causes an undesirable ghost beam to be formed due to reflections from the rear surface of the base substrate. Thinner substrates can be manufactured from Mylar, and do not exhibit this ghosting effect, but are much more fragile. Cube beam splitters are also commonly used in the field of optics, however for ultra-fast pulsed systems, they typically are not the best choice of beam splitter as the two prisms employed are quite large and thus reflected and transmitted beams suffer greatly from dispersion. Ideally, creating a beam splitter for the THz range should avoid these pitfalls.

4.1.1 Current State-of-Art

High impedance silicon (HiZ-Si) wafers are currently the most well established form of beam splitting in the THz range (Homes *et al.* 2007). These HiZ-Si wafers have a fixed splitting ratio of 50:50, and are employed in various thicknesses to delay the large Fabry-Pérot interference caused by the HiZ-Si wafer's high refractive index at THz frequencies, as to not interact and disturb measurements. Other beam splitters in the THz range are polarization dependent (Berry and Jarrahi 2012). The following sections describe a beam splitter designed for the THz range of which any splitting ratio can be created during the rapid prototyping process, non-polarization dependent and free from Fabry-Pérot interference.

4.1.2 Conductive Layer Concept

Walther *et al.* (2007) first described the characteristics of thin metal films at THz frequencies. In particular, it can be noted that the thin metal films of nanometer thicknesses where partially translucent to incident to normal incident THz radiation. This then led

Ung *et al.* (2012) to design and fabricate a beam splitter based on the property that THz radiation is reflected by metallic surfaces. A thin transparent substrate, low-density polyethylene (LDPE) was then chosen to apply coatings of silver conductive paint to fabricate the beam splitter. The following section describes in detail the theoretical principle of the fabricated beam splitter.

4.2 Theoretical Model

Conventional beam splitters for terahertz applications rely on the partial reflection arising from the dielectric contrast at material interfaces. Broadband applications preclude the use of $\frac{\lambda}{4}$ interference coatings to achieve a better control over the partial reflection and transmission ratio. In contrast to the traditional dielectric terahertz beam splitters, the proposed beam splitter is based on reflection from a thin metal coating applied to the surface of an ultra-thin dielectric LDPE substrate. To model this arrangement, we consider a thin conductive layer, with a complex index of refraction and finite conductivity. It is also necessary to estimate the skin depth required at terahertz frequencies, as a substantial amount of transmission will only be possible for conductor thicknesses below the skin depth. The skin depth δ can be calculated (Maier 2007) as,

$$\delta = \sqrt{\frac{2}{\mu_0 \mu_r \sigma_0 \omega}}, \tag{4.1}$$

where μ_0 is the magnetic permeability of free space, σ_0 is the DC conductivity, μ_r is the relative permeability of the medium and ω is the angular frequency.

For the silver conductive paint used in this paper, the skin depth calculated in the range of frequencies from 0.1 to 3.5 THz decreases from approximately 72 to 12 μm, using values of μ_r = 1 and σ_0 = 500 S·m^{-1} (this value will be discussed later in Section 4.5). As it is possible to fabricate the beam splitters with coatings below these thicknesses, the transmissive properties can be accurately determined. For a theoretical calculation of the relative transmission of the metallic coating, with respect to thickness and frequency, the Tinkham formula (Cooke *et al.* 2006, Hegmann *et al.* 2006, Tinkham 1956, Walther *et al.* 2007) can be used,

$$T(\omega) = \left| \frac{E_{\text{sample}}(\omega)}{E_{\text{reference}}(\omega)} \right| = \frac{1}{\left| 1 + \tilde{\sigma} d \cdot \frac{Z_0}{n_{\text{substrate}}+1} \right|^2}, \tag{4.2}$$

where $T(\omega)$ is the transmission calculated with respect to frequency, $\tilde{\sigma}$ is the complex conductivity of the metal, d is the thickness of the metallic layer, $n_{\text{substrate}}$ is the refractive index of the substrate and Z_0 is the impedance of free space.

The dispersion of the complex conductivity $\tilde{\sigma} = \sigma_1 + j\sigma_2$, is calculated as,

$$\sigma_1 = \frac{\sigma_0}{1+(\omega\tau)^2}, \quad \sigma_2 = \sigma_0 \cdot \frac{-(\omega\tau)}{1+(\omega\tau)^2}, \quad \text{with} \quad \tau = \frac{m_0\sigma_0}{Ne^2}, \tag{4.3}$$

where m_0 is the electron rest mass, N is the free electron density, e is the electron volt charge and τ is the damping time constant (Maier 2007).

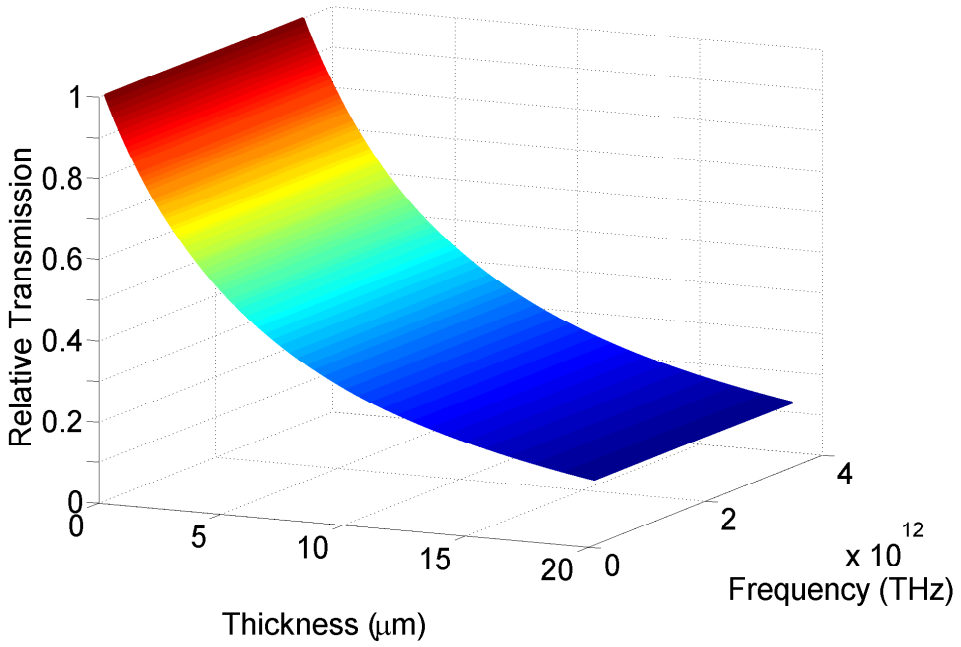

Figure 4.1. A 3-D plot of thickness, frequency and relative transmission for thin conductive layers. The transmission appears to be nearly invariant over the frequency range, due to the small layer thickness well below the skin depth. Simplified frequency-invariant model of transmission is dependent only on the thickness of the paint.

Using a LDPE substrate, which has a constant refractive index of $n = 1.51$ from lower terahertz frequencies up to 5 THz, and silver conductive paint as the metallic layer, the relationship between the thickness and the relative transmission for all frequencies in the considered range can be calculated using Equation (4.2). The result of this computation is shown in Figure 4.1 for silver paint thicknesses between 0 and 20 μm, in

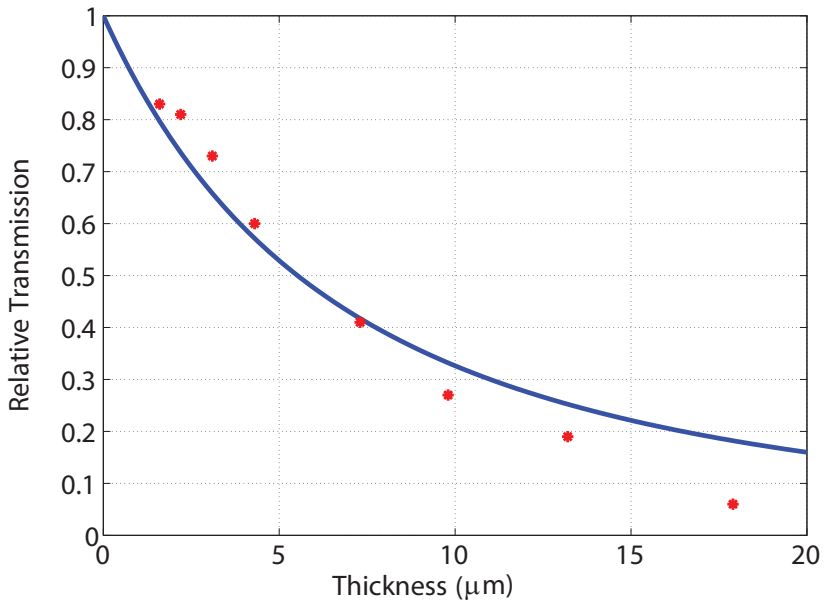

Figure 4.2. A 2-D plot of thickness against relative transmission for thin conductive layers at 1 THz. A plot of thickness and frequency against relative transmission. Simplified frequency-invariant model of transmission dependent only on the thickness of the paint. The blue curve is plotted according to the theoretical model and fitted with a DC conductivity of 500 $S{\cdot}m^{-1}$, while the red points represent the measured data.

the frequency range of 0.1 to 3.5 THz. Of particular note, it is observed that the relative transmission calculated from the given frequency range shows that transmission is in fact nearly frequency independent for very thin conductive layers, which follows the calculations by Walther *et al.* (2007). Therefore, the frequency dependence can be removed from consideration to simplify the model. This results in a transmission dependence based only on the thickness, as plotted in Figure 4.2. This plot shows that in order to obtain a 50:50 ratio of reflection to transmission, a metallic coating of approximately 5.5 μm needs to be obtained assuming a DC conductivity of 500 $S{\cdot}m^{-1}$. Other ratios can be similarly determined from this data. It is noted that this approximation does not take into account absorption from the thin substrate, as its absorption is negligible.

The presented theoretical model has so far only considered the case of normal incidence. For practical scenarios, the beam splitter might need to be placed at different angles of incidence, for example 45° degrees in interferometric applications. This requires the use of Fabry-Pérot equations (Bauer 1992, Born and Wolf 1997, Heavens 1955, Heald and Marion 1994) for determining the angular dependence for the reflectance and

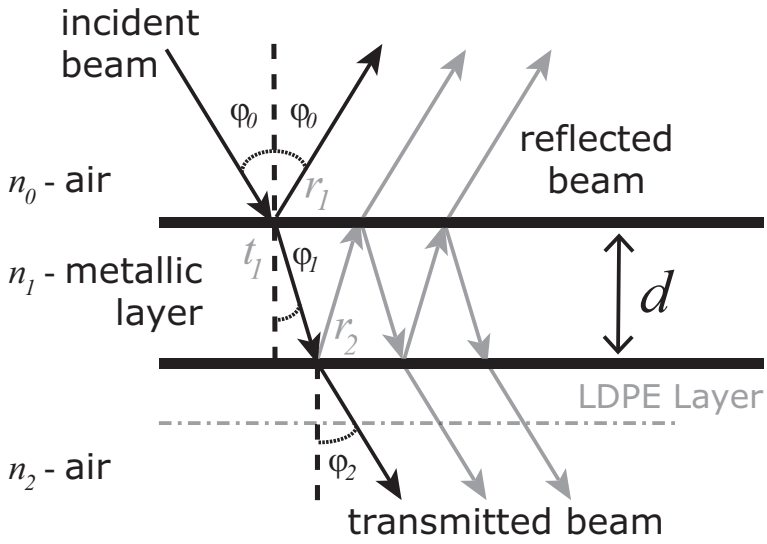

Figure 4.3. Schematic diagram of the Fabry-Pérot effect in the layers of the beam splitter. The very thin LDPE layer can be neglected here as it does not exhibit any measurable time delay or losses at terahertz frequencies. The Fresnel coefficients used in (4.4) are denoted here by t_1, r_1 and r_2.

transmittance of beam splitter samples at varying angles of incidence. To set-up these equations, the first medium where the beam is incident is air, the second medium is the silver conductive paint, followed by air again. The very thin low-permittivity substrate sheet of LDPE is ignored here, as it has negligible effects at terahertz frequencies. The arrangement is shown in Figure 4.3, where air, silver conductive paint and air are denoted by the subscripts, 0, 1 & 2 respectively and δ_1 is the phase delay between media. The relative reflection can be calculated by,

$$R(\omega) = r_1 - t_1^2 r_2 e^{-2i\delta_1} + t_1^2 r_1 r_2^2 e^{-4i\delta_1} - t_1^2 r_1^2 r_2^3 e^{-6i\delta_1} + \dots \tag{4.4}$$

Standard Fresnel coefficients t_1, r_1 and r_2 in (4.4) are defined in Figure 4.3, can be calculated for both horizontal (P) and vertical (S) polarizations as below (Heavens 1955),

$$t_{1P} = \frac{2n_0(\omega)\cos\varphi_0}{n_0(\omega)\cos\varphi_1 + n_1(\omega)\cos\varphi_0} \tag{4.5a}$$

$$t_{1S} = \frac{2n_0(\omega)\cos\varphi_0}{n_0(\omega)\cos\varphi_0 + n_1(\omega)\cos\varphi_1} \tag{4.5b}$$

$$r_{1P} = \frac{n_0(\omega)\cos\varphi_1 - n_1(\omega)\cos\varphi_0}{n_0(\omega)\cos\varphi_1 + n_1(\omega)\cos\varphi_0} \tag{4.5c}$$

$$r_{1S} = \frac{n_0(\omega)\cos\varphi_0 - n_1(\omega)\cos\varphi_1}{n_0(\omega)\cos\varphi_0 + n_1(\omega)\cos\varphi_1} \tag{4.5d}$$

$$r_{2P} = \frac{n_1(\omega)\cos\varphi_2 - n_2(\omega)\cos\varphi_1}{n_1(\omega)\cos\varphi_2 + n_2(\omega)\cos\varphi_2} \tag{4.5e}$$

$$r_{2S} = \frac{n_1(\omega)\cos\varphi_1 - n_2(\omega)\cos\varphi_2}{n_1(\omega)\cos\varphi_1 + n_2(\omega)\cos\varphi_2}, \tag{4.5f}$$

where, $\frac{n_0(\omega)}{n_1(\omega)} = \frac{\sin\varphi_1}{\sin\varphi_0}$, $\frac{n_1(\omega)}{n_2(\omega)} = \frac{\sin\varphi_2}{\sin\varphi_1}$ and $\delta_1 = (2\pi n_1 d_1 \cos\varphi_1)/\lambda$.

The terms of the series after the third order can be neglected, due to the rapid convergence of the model.

The relative ratio A of power absorbed in the lossy paint, can be calculated from Bauer (1992)

$$A(\omega) = \frac{\frac{4y}{\tilde{n}(\omega)}\cos\varphi_0}{(2 + \frac{y}{\tilde{n}(\omega)}\cos\varphi_0)^2}, \tag{4.6}$$

where $\tilde{n}(\omega)$ is the complex refractive index of the silver conductive paint, $y = (\sigma_0 d)/(\epsilon_0 c)$ with ϵ_0 the permittivity of vacuum and c the speed of light. Now, applying the conservation of energy, the theoretical transmittance can be calculated as

$$\mathcal{T}(\omega) = 1 - \mathcal{R}(\omega) - A(\omega) \quad , \tag{4.7}$$

where $\mathcal{T}(\omega)$ and $\mathcal{R}(\omega)$ equal $T^2(\omega)$ and $R^2(\omega)$ respectively.

The modelled $\mathcal{T}$, $\mathcal{R}$ and $A(\omega)$ for both P and S polarizations will be compared to the measured data in the results section.

4.3 Fabrication

Low cost off-the-shelf materials are used for fabrication of the beam splitter. Initially, a 50 mm inner diameter aluminum ring is fabricated as the frame structure for the

beam splitter. The substrate material used is common generic branded supermarket purchased LDPE cling-wrap, with a thickness of approximately 6.5 μm—this thickness is lower than that of Theuer *et al.* (2010) as the LDPE is stretched over the aluminum ring. This low cost material presents a low terahertz absorption and is relatively easy to handle. The aluminum ring is heated in an oven for 5 minutes at a temperature of 160°C. The LDPE sheet is stretched over the ring, and slightly melts thereby forming a bond onto the metal surface. The ring is allowed to return to room temperature in a minimal dust environment. The ring with the LDPE sheet is weighed to provide a reference point. Common silver paint (Electrolube ESCP03B) is thinned out using ethanol to obtain sufficiently small paint droplets. This mixture is then placed into an airbrush with a minimum nozzle size of 200 μm, and sprayed at an arm's length to the stretched LDPE sheet, providing a uniform coverage (fabricated samples are shown in Figure 4.4).

The paint is allowed to dry at room temperature for 30 minutes and the ring with coated sheet is weighed again. The increase in weight from the initial value is then used to determine the thickness of the layer of paint applied to the beam splitter, given the known density of silver. Optical profilometry (Ambios Profilometer) is used to check the density, thickness, uniformity and surface roughness of the coatings, providing verification for the calculations. The optical profilometry shows that samples have good uniformity of with a standard deviation of approximately 1.7 μm for a sample with average conductive silver paint thickness 9.8 μm. The average value of the thickness in this case shows good agreement with the calculated values based on paint density, area and weight difference.

The paint shows good adhesion with the LDPE film, requiring targeted damage to scratch the paint from the surface. Moreover, the LDPE film requires significant force to dislodge it from the aluminum ring. With due care, the conductive paint coating remained intact for well over 9 months.

4.4 Experimental Characterisation

The experimental set-up for the measurement of transmittance and reflectance from the beam splitter for incidence is performed with a Picometrix T-Ray 2000XP THz-TDS system as shown in Figure 4.5. This system is advantageous as the fibers coupled to the emitter and detector heads enable them to be moved around an optical table

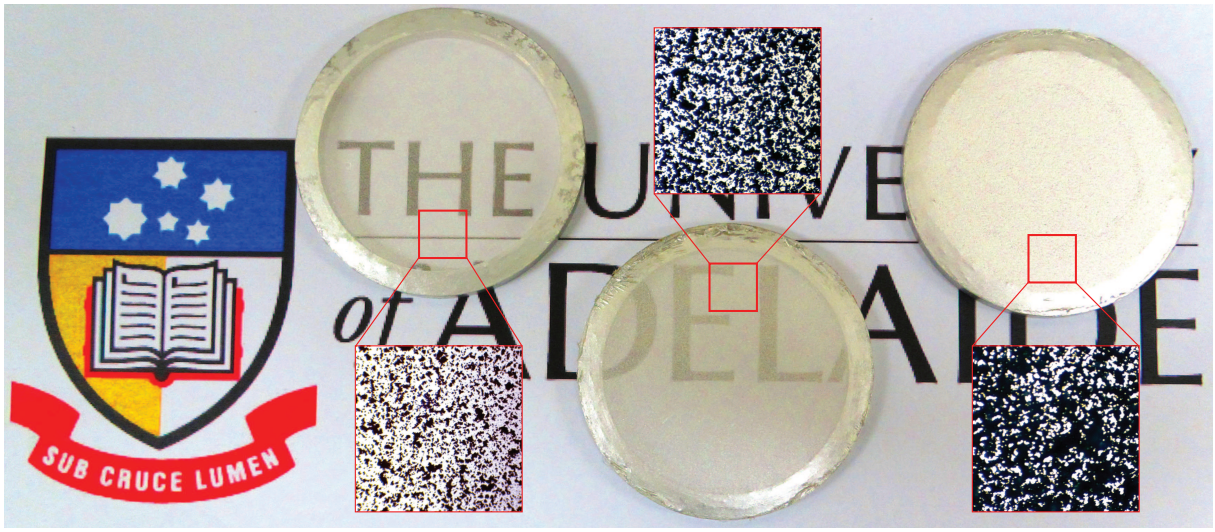

Figure 4.4. Photograph of the fabricated beam splitters. From the left, beam splitters are shown with a terahertz reflection/transmission ratio of 10:90, 50:50 & 90:10. The expanded views show photos from a microscope camera showing the surface of the silver conductive paint layer at a magnification of 60×. These microscope photos show that the area of the LDPE is covered more than 10% and 50% for the 10:90 and 50:50 ratio beam splitters respectively, demonstrating that they are not area based polka-dot beam splitters.

freely, thus permitting measurements to be conducted at varying angles of incidence. The limitation of the system however does not allow reflection measurements to be performed at normal incidence. Therefore, as an exception, a reflection based THz-TDS (Rønne *et al.* 1997) has been used for this particular case.

An initial measurement on an uncoated LDPE film confirmed that this layer can be neglected. Coated samples were then measured to characterize their transmission and reflection profiles. The measurements were performed in air atmosphere for angles of incidence φ_0 varying from 25° to 50° in both P and S polarizations. Transmission measurement of a 9.8 μm coated sample at normal incidence demonstrates that the transmitted pulse is attenuated compared to the reference pulse, however without any delay in the time-domain pulse (Figure 4.6) or added spectral features on the frequency spectrum (Figure 4.7).

4.5 Results

Data is obtained from transmitted pulses of multiple beam splitter samples at normal incidence and are plotted in comparison with the modelled data in Figure 4.2. This

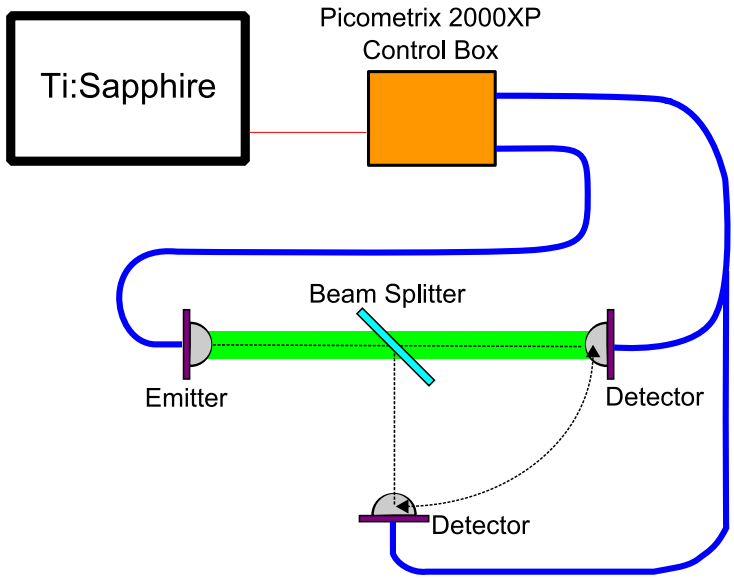

Figure 4.5. Schematic diagram of the Picometrix 2000XP THz-TDS system. The output of a Ti:Sapphire laser (Spectra-Physics Mai-Tai with a pulse-width of < 100 fs) is coupled into the control box of the Picometrix 2000XP system which is fiber-coupled to movable emitter and detector heads, allowing transmission and reflection from the beam splitter to be be measured for varying angles of incidence.

measured data is curve-fitted to the theoretical model of Equation (4.2) (Figure 4.2), yielding the DC conductivity of the silver conductive paint of $\sigma_0 = 500\ \mathrm{S{\cdot}m^{-1}}$, this DC conductivity is much lower than that of Laman and Grischkowsky (2008), due to the difference between the silver conductive paint and pure metal. This value fits the data to a correlation factor of $R = 0.9965$, showing close conformity to the curve fitted DC conductivity. The discrepancy between the model and the measurements observed for the thinnest and thickest samples are attributed to the effects related to the uniformity of the paint layers: Non-uniformities, which are more pronounced for thinner layers, tend to decrease the conductivity of the film. It can be observed in the microscope photographs shown, as insets in Figure 4.4, that the paint particles tend to clump together as the thickness increases.

Measurement data for the transmittance at normal incidence are presented in Figure 4.10 for beam splitters fabricated for different splitting ratios averaged over the frequency range of 0.5 to 1.5 THz. The ratios of reflectance to transmittance are varied in steps from approximately 10:90 to 90:10. An interesting observation is that, as the frequency decreases and the thickness approaches one fifth of the skin depth (at

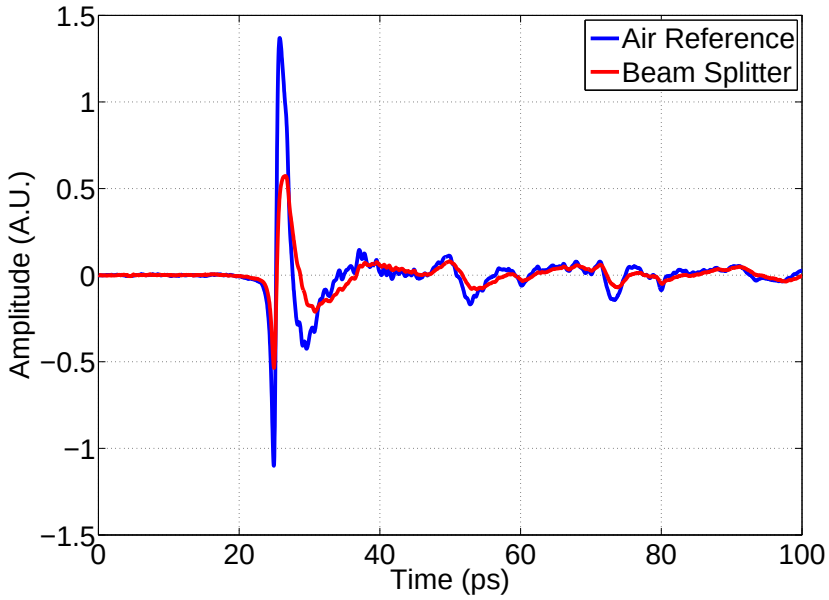

Figure 4.6. Time-domain plot of the reference pulse and LDPE beam splitter in lab air. The shape of the time-domain pulse is not affected by the transmission through the beam splitter. The splitting ratio of the beam splitter used here is 60:40.

approximately 0.8 THz), higher transmission can be observed. This is consistent with the work presented by Walther *et al.* (2007), where thinner metal films exhibited higher relative transmission than the theoretical model used due to the lower conductivity arising from the mentioned inhomogeneities. The thicker coatings in contrast, show fewer voids, and thus exhibit a higher conductivity closer to the quoted DC conductivity of the silver conductivity paint. Back calculations from the data show that the conductivity drops to 150 $S{\cdot}m^{-1}$ for the thinner coatings from 500 $S{\cdot}m^{-1}$ of the thicker coatings. The measurements for 45° incidence are shown in Figures 4.8 & 4.9 only for a specific sample for brevity. These curves illustrate the behaviour of the beam splitters at 45° in both polarizations, and as expected, do not exhibit a strong frequency dependence. The selected sample has an approximate thickness of 9.8 μm and a modelled splitting ratio of approximately 60:40 reflection to transmission. Due to the physical constraints of the system and to the finite size of the beam splitter's aperture, the angular range is limited to φ_0 equaling 25° to 50° for both reflection and transmission. The experimental results at 1 THz are plotted in Figures 4.11 & 4.12 for the polarizations P and S respectively. A close agreement of the experimental data with the theoretical model is observed in both polarizations. In particular, an increase in transmittance is

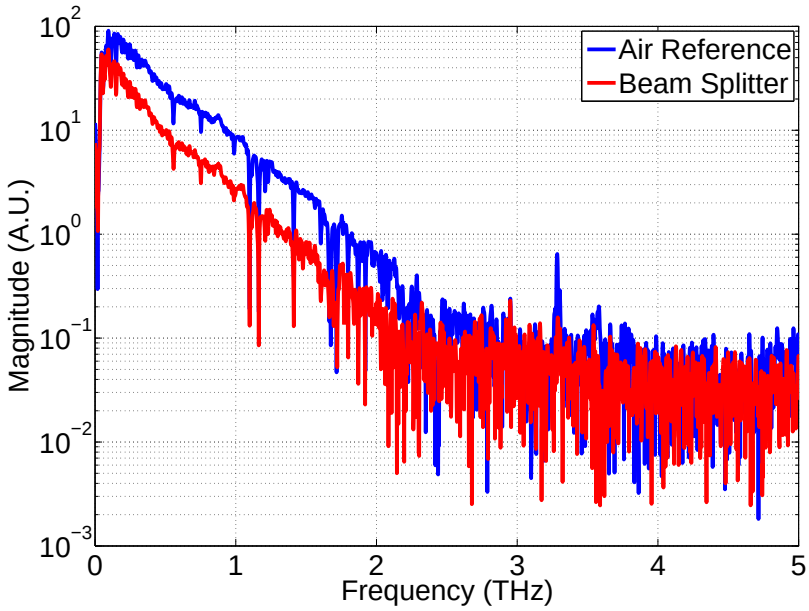

Figure 4.7. Frequency-domain of the reference pulse and LDPE beam splitter in lab air. Frequency plot of the reference pulse and of the pulse transmitted through the beam splitter. The beam splitter does not contribute additional absorption peaks, while the broadband attenuation appears to be approximately uniform. The splitting ratio of the beam splitter used here is 60:40.

observed in Figure 4.11, as the angle of incidence increases towards the Brewster angle of the silver conductive paint, at 72°. In contrast for the S polarization, a steady increase in reflectance is observed together with a decrease in the transmittance as the angle of incidence increases. The estimated losses in both polarizations are also consistent with the error range calculated from the standard deviation of the thickness of the silver conductive paint (in this case approximately ±5.5%). For both polarizations, the efficiency at 1 THz of the beam splitter is approximately 90%.

4.6 Comparison with Silicon Beam splitters

Commonly, Hi-Z Si wafers are employed in THz-TDS systems as beam splitters (Homes *et al.* 2007) and as mentioned for reflection mode based systems in the previous Chapter. The frequency-dependent performance of two such beam splitters with different thicknesses (200 μm and 1 mm) have been measured for comparison with the proposed thin-metal-film beam splitter. The results are plotted in Figure 4.13 and show that Hi-Z Si wafers (without time-domain echos removed), suffer greatly from

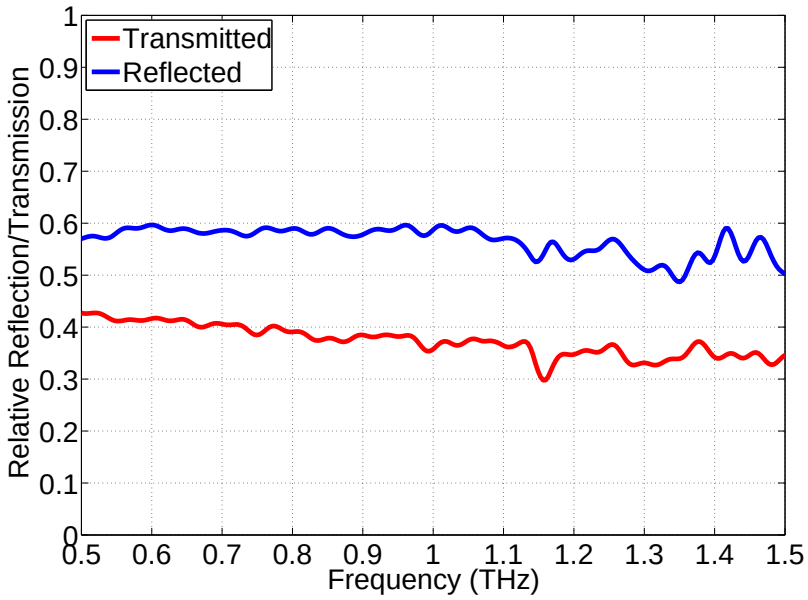

Figure 4.8. Relative reflection & transmission of a beam splitter for 45° P polarization.. Plot of P polarization plot for relative reflection and transmission of a beam splitter with splitting ratio of 60:40 at 45° incidence. It can be noted that the P polarization reflectance is lower than that of the S polarization in agreement with the modelled results shown in Figure 4.10.

strong frequency-dependent oscillations of the splitting ratio, arising from Fabry-Pérot interference effects. This is particularly critical for thicker samples, whereas it can be noted that the thinner sample exhibits slower oscillations, but is difficult to handle. Removing the interferences through time-gating requires thick samples, which are bulky and expensive. For a similar averaged ratio of reflection to transmission, the proposed thin conductive film beam splitter has a much smoother transmission curve and avoids Fabry-Pérot interference effects, due to the low refractive index and very thin substrate. An additional advantage of the thin-metal-film beam splitters are that the ratios of reflection and transmission can be adjusted and optimized for particular systems unlike the fixed ratio provided by Hi-Z Si.

4.7 Power Scaling

To verify the linearity of this beam splitter for use in both low and higher power THz systems, it was necessary to compare the beam splitter's performance from the previous sections performed with a low power system, to that of measurements performed

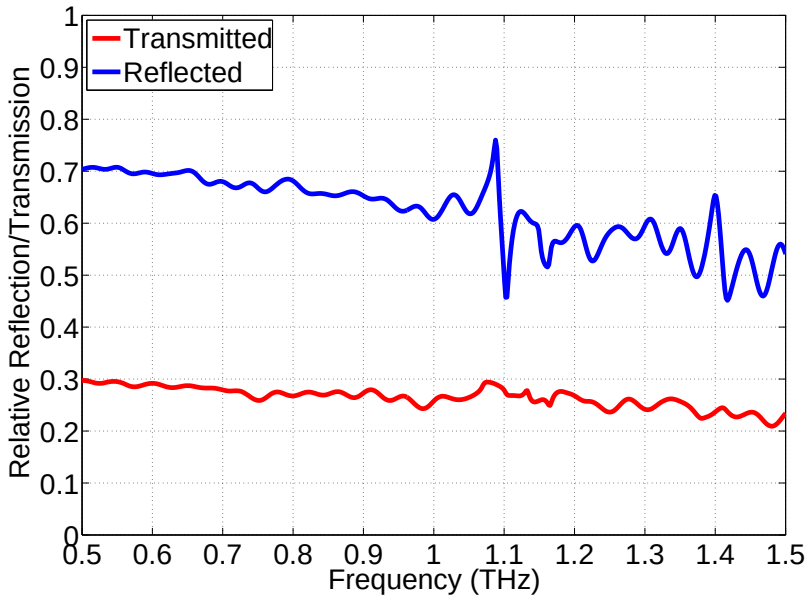

Figure 4.9. Relative reflection & transmission of a beam splitter for 45° S polarization.. Plot of S polarization for relative reflection and transmission of a beam splitter with splitting ratio of 60:40 at 45° incidence. It can be noted that the P polarization reflectance is lower than that of the S polarization in agreement with the modelled results shown in Figure 4.10.

with a high power THz system. In this case, an amplified Ti:sapphire laser pumping a $LiNbO_3$ crystal for high power EO emission along with EO detection from a ZnTE crystal was used to characterise the transmission performance of the beam splitter at μW power levels. It can be seen that there is good agreement between both low and high power THz systems, showing that the properties of the beam splitter at scale accordingly from low-power systems to higher-power systems.

As the bandwidth of the high-power THz-TDS system used for measurements was limited to approximately 0.8 THz, the samples show some discrepancies to the measurements performed in low-power systems. In addition, the transportation of the samples from Australia to Japan may have affected the silver paint coatings while in transit, thus showing differences in results.

4.8 Chapter Summary

A low cost ultra-thin LDPE beam splitter has been presented for low-dispersion splitting for reflection and transmission in THz-TDS systems. Several fabricated samples

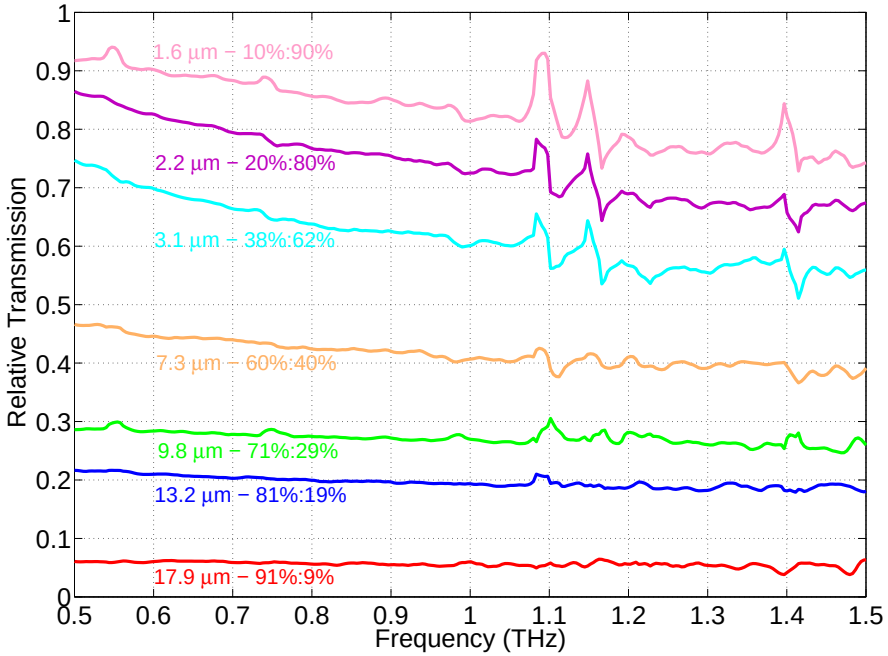

Figure 4.10. Multiple transmission plots of varying beam splitters. Terahertz transmission plots of beam splitters with varying thickness at normal incidence. The increase in the conductive layer thickness led to decreased transmission. The peaks in the curves are due to the water absorption in lab air. The modelled values of splitting ratios are depicted next to each curve.

have been characterized physically and optically, and the transmission/reflection properties have been compared to a theoretical model. In addition, the angular characteristics for practical applications of the beam splitter have been demonstrated at both horizontal and vertical polarizations, as well as for both low and high power THz-TDS systems. Finally, the performance of this beam splitter has been compared to the traditionally used Hi-Z Si wafers. Potential applications for this beam splitter include a beam sampler for real-time monitoring of high-power sources, as well as a potential replacement for Hi-Z Si wafers in reflection mode terahertz spectroscopy systems or in operating at terahertz frequencies. Chapter 5 follows on from this work, detailing the use of conductive polymers as the conductive layer as an alternative to the silver paint employed in this Chapter.

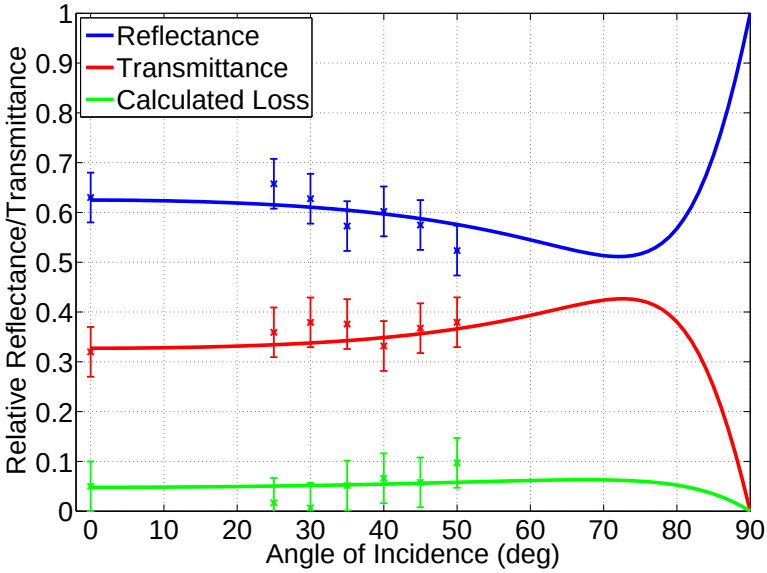

Figure 4.11. Plots of P polarization for beam splitter against angle. Relative transmission, reflection and loss in P polarization. Relative transmission, reflection and loss in S polarization. The error bars in and are calculated from the standard deviation of the thickness of coatings for a sample with a beam splitting ratio of 60:40. The solid lines denote the model used, while the points show the measured data.

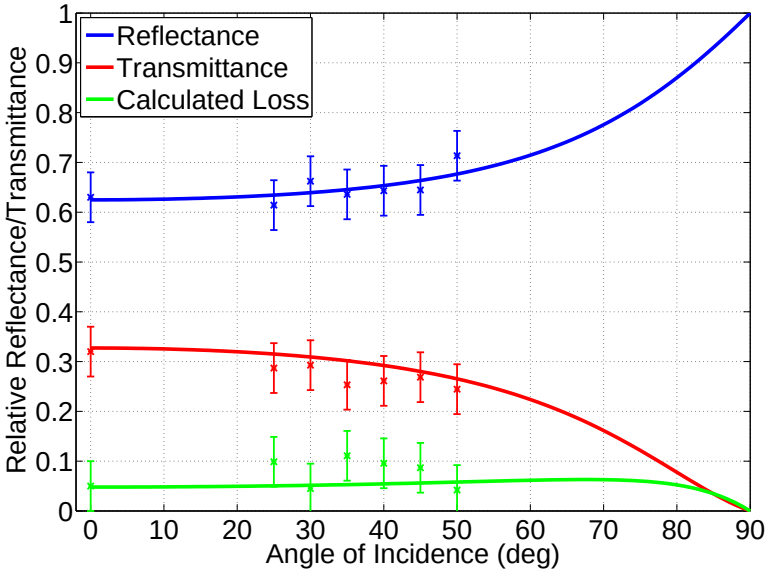

Figure 4.12. Plots of S polarization for beam splitter against angle. Relative transmission, reflection and loss in P polarization. Relative transmission, reflection and loss in S polarization. The error bars in and are calculated from the standard deviation of the thickness of coatings for a sample with a beam splitting ratio of 60:40. The solid lines denote the model used, while the points show the measured data.

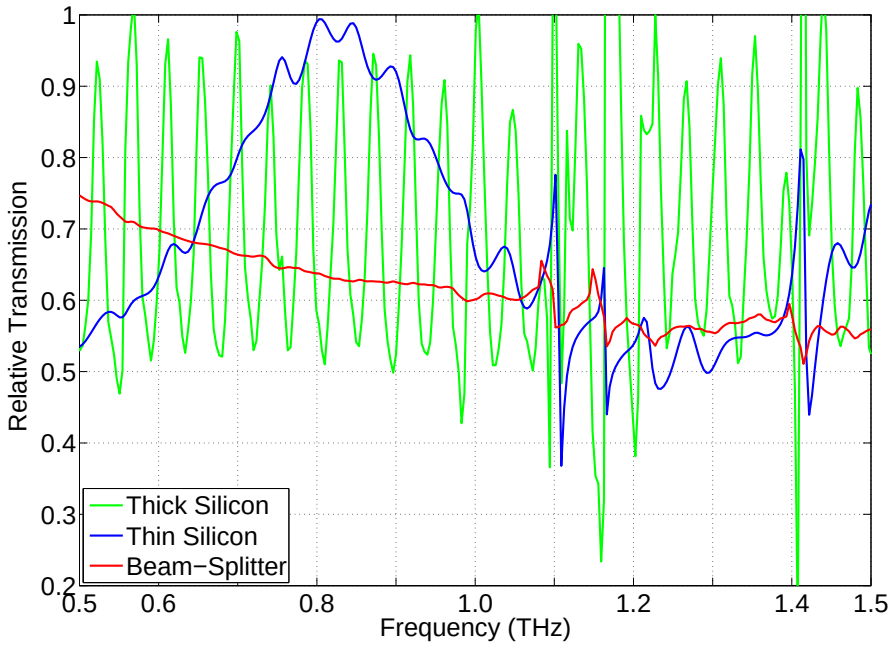

Figure 4.13. Comparison of beam splitters. Comparison of the transmittance curves for a 1 mm thick Hi-Z Si wafer (green), a thin 200 μm wafer (blue) and a silver painted beam splitter with a splitting ratio of 38:62. Note that the LDPE beam splitter exhibits a smoother transmission as a function of frequency, compared to the two Hi-Z Si wafers without Fabry-Pérot interference being removed within the time-domain.

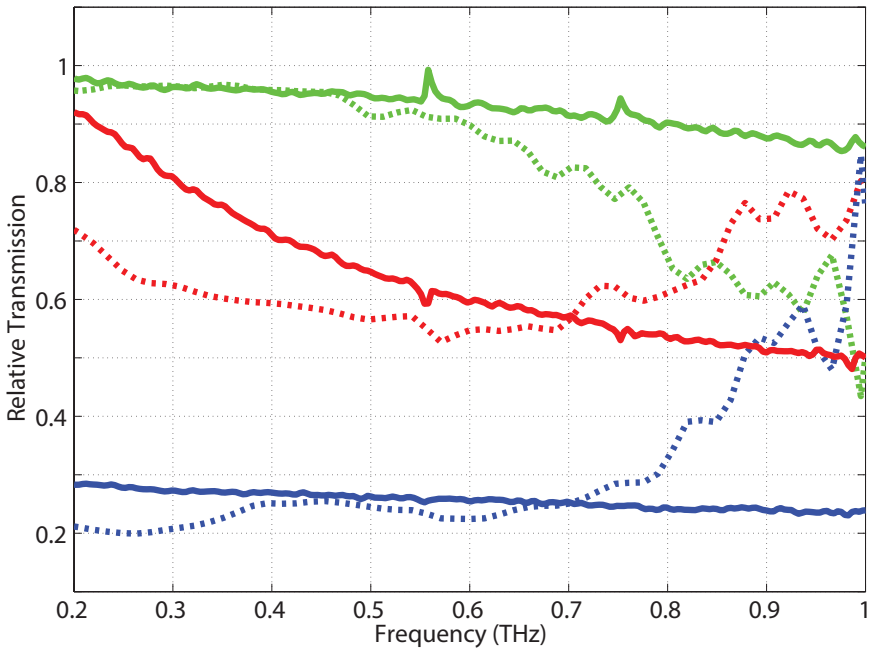

Figure 4.14. High power performance at normal incidence. The relative transmission of three samples in green, red and blue depicting samples of 90%, 50% and 20% transmission at 1 THz, respectively, for normal incidence. The solid lines denote measurements taken with a low power system, while the dotted lines denote measurements taken with a high power system. The trend present in the plots is due to the frequency approaching roughly one fifth of the skin depth for frequencies above 0.8 THz (Walther *et al.* 2007).

Chapter 5

Conductive Polymer Beam Splitters for Terahertz

CONDUCTIVE polymers are a recently new area of research and have many new applications that have yet to be discovered. Chapter 4 covered the use of a thin conductive metallic layer as a beam splitter for THz applications. This Chapter details the use of two common conductive polymers, PEDOT[a] and PPY[b] as an advancement to the silver conductive paint previously used. A novel fabrication method based on inkjet printing is also described, which also provides a more accurate prototyping method.

[a] poly(3,4-ethylenedioxythiophene)
[b] polypyrrole

5.1 Introduction

The previous Chapter presented a new technique to fabricate and implement beam splitters for use in the THz frequency range. The beam splitter employed in this case, exploited the skin depth of a conductive layer, such that an incident beam may be partially transmitted and reflected, with the thickness of the layer determining the splitting ratio. Conductive polymers present another possibility for exploiting skin depth in controlled power splitting. The use of inkjet printing of these polymers enables more accurate fabrication in terms of thickness than the spray painting technique discussed in the previous Chapter. A recent publication has already demonstrated polarizers for the THz range fabricated using conductive polymers (Das *et al.* 2012).

5.2 Background

Plastics and polymers are generally not associated with electrical conduction, but rather as insulators. During the 1970s, breakthroughs by Shirakawa *et al.* (1977) saw the fabrication of the first polymers with high electrical conductivities. This breakthrough earned Heeger, MacDiarmid and Shirakawa the Nobel Prize in Chemistry in 2000 (Inzelt 2008).

The flow or transport of electrons is not as conceptually simple as that within metal conductors, rather it can be described as electron exchange reactions or electron hopping. This occurs as a process of reduction and oxidation (redox) between redox sites in redox based conductive polymers and also by the movement of de-localised electrons in conjugated systems of intrinsically conductive polymers (Inzelt 2008). A greatly simplified process of redox is shown in Figure 5.1. A very interesting aspect of conductive polymers is that they are able to switch between both conductive and insulating states with changes in an applied voltage, leading to many possible applications, such as corrosion prevention, producing artificial muscles and flexible sensors (Vernitskaya and Efimov 1997, Groenendaal *et al.* 2000, Inzelt 2008). However in this case, the relatively high conductivity can be used much like the silver paint coating for THz beam splitters in Chapter 4.

Conductive polymers can be grouped in three types; Redox Polymers, Intrinsically Conducting Polymers (ICPs) and Composite Materials (Inzelt 2008). Redox conductive polymers contain localized redox sites that can either be oxidized or reduced allowing

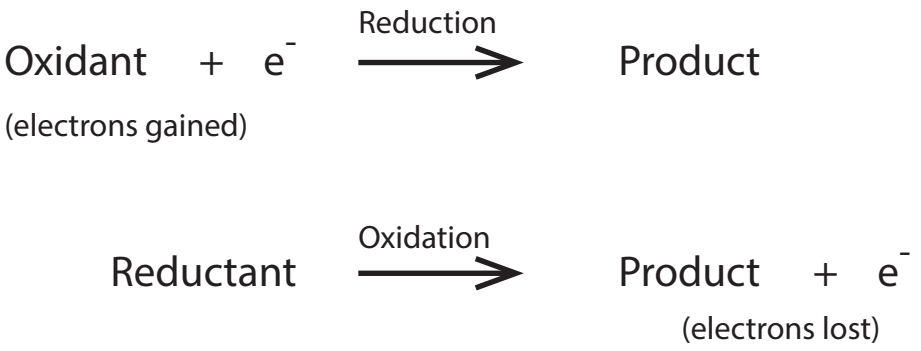

Figure 5.1. The redox process. The general chemical equations of the process of redox. The exchanging of electrons by the gain and loss in oxidation and reduction reactions allows for current flow in conductive polymers.

electrons to flow by the process of electron hopping, where electrons are exchanged as the reactions take place. Intrinsically Conducting Polymers contain conjugate systems, which contain either benzoid and heterocyclic compounds joined together in chains. As can be seen in Figure 5.2, this type of conductive polymer contains alternating structures that allow electrons to flow across within a chain. Of particular interest in this Chapter is PPY, which is an ICP. Finally, composite materials are similar to ICPs, but they are composed of both ICPs and nano metal particles to facilitate and control conduction. PEDOT belongs to composite material type conductive polymers (Selvaganesh *et al.* 2007) and is also a material of interest in this Chapter. The molecular structure of PEDOT with a gold nanocomposite can be seen in Figure 5.3. PEDOT has also been recently characterised at THz frequencies by Yamashita *et al.* (2011).

5.3 Theoretical Model

The theoretical model to calculate the transmittance $T^2(\omega)$ of three samples, PPY of 1 μm thick, and two PEDOT samples 1 and 2 μm in thickness, uses standard Fabry-Pérot equations (Heavens 1955) over air, conductive polymer and substrate layers. The loss $A(\omega)$ is then calculated according to Bauer (1992), from Equation 4.6 from Chapter 4, where $\tilde{n}$ is the frequency dependent complex refractive index, φ_0 the angle of incidence and $y = (\sigma_0 d)/(\epsilon_0 c)$, where σ_0 is the DC conductivity of the conductive polymer, d the thickness of the conductive polymer, ϵ_0 the permittivity of vacuum and c the speed of light. Thus, the reflectance can be calculated from Equation 4.7.

The complex refractive indices of both the PEDOT and PPY samples used in the theoretical model are calculated, by first measuring the samples in transmission mode, then

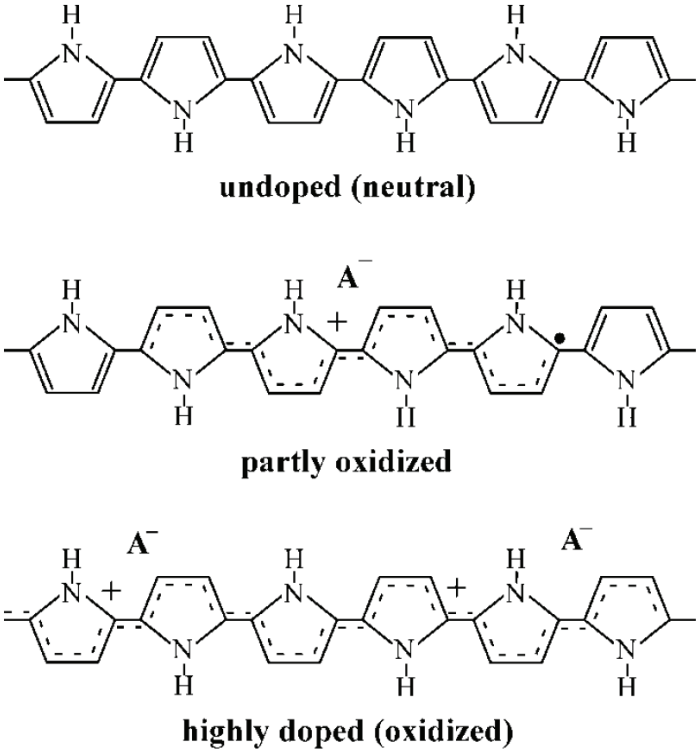

Figure 5.2. Molecular structure of PPY. The molecular structure of PPY at different oxidation levels. Anionic dopants are incorporated for charge neutrality to be maintained. After Smela (2003).

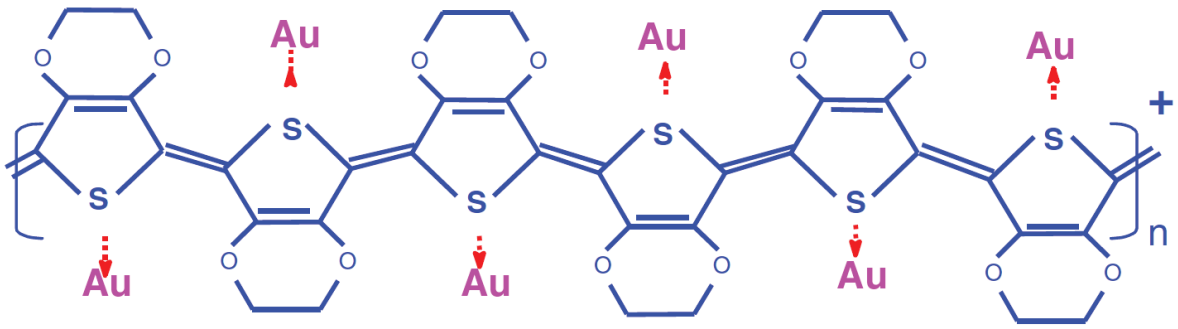

Figure 5.3. Molecular structure of PEDOT. The molecular structure of PEDOT with a gold nanocomposite. After Smela (2003).

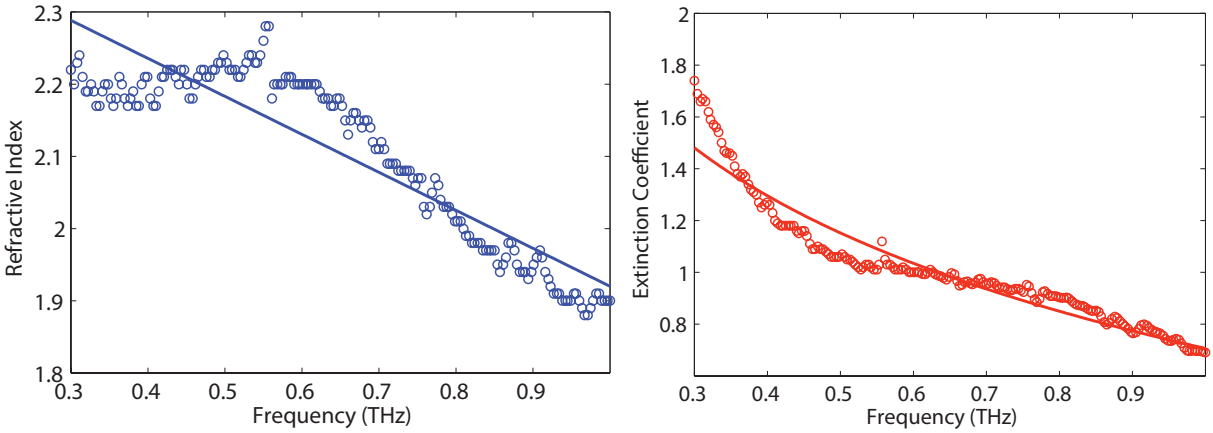

Figure 5.4. The complex refractive index of PEDOT. The real (n) and imaginary (κ) curve fits of the PEDOT samples fitted using SVMAF. The dots depict the calculated refractive index and extinction coefficient from the *Teralyzer* software, while the solid line shows the fitted curve used in the theoretical model for transmission, reflection and losses.

applying the Spatially Variant Moving Average Filter (SVMAF) in the implementation of the commercially available software *Teralyzer* (Pupeza *et al.* 2007). The *Teralyzer* software allows for material parameters of samples with thicknesses of less than 100 μm to be accurately extracted from data. A curve fit is then applied to the acquired data for both the real and imaginary parts of the frequency-dependent refractive indexes for both the PEDOT and PPY samples, with an R-factor of approximately 0.9. These values are then back substituted into the Fabry-Pérot equations. The curve fits for the complex refractive index of PEDOT can be seen in Figure 5.4, and Figure 5.5 for PPY. A linear curve fit is applied to the real part of the complex refractive index to simplify calculations and model the general trend of data points acquired from measurements, while the imaginary part is fitted with a simple exponential curve, again to model the general trend from data points.

The PEDOT samples use the same refractive index, while the PPY has a different refractive index. The DC conductivities of the PEDOT and PPY are known from fabrication. The behaviour of the samples can then be calculated in the frequency domain as a function of both the angle of incidence and the specific frequency of operation. The predictions form this theoretical model are discussed in Section 5.6 and compared to the acquired reference, transmittance and reflectance data.

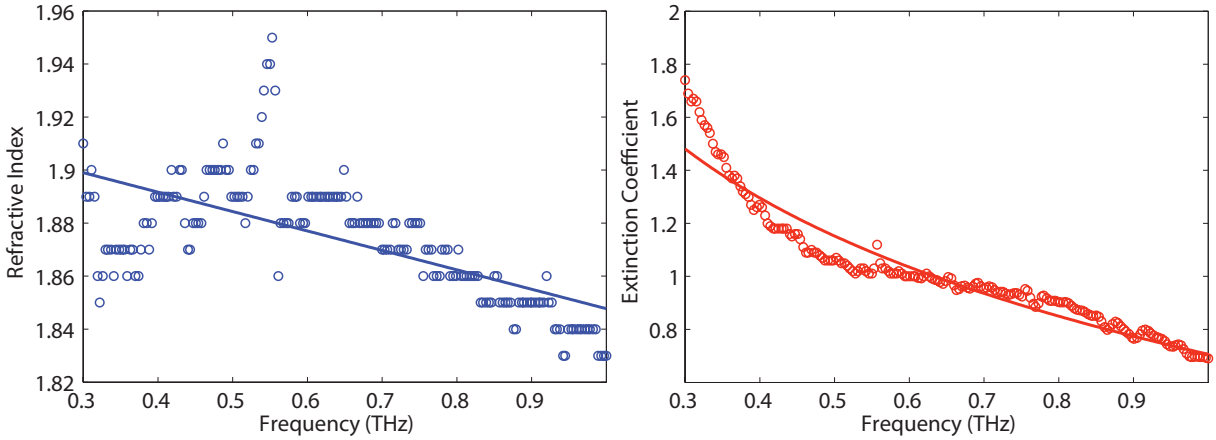

Figure 5.5. The complex refractive index of PPY. The real (n) and imaginary (κ) curve fits of the PPY samples fitted using SVMAF. The dots depict the calculated refractive index and extinction coefficient from the *Teralyzer* software, while the solid line shows the fitted curve used in the theoretical model for transmission, reflection and losses.

5.4 Fabrication

The PEDOT and PPY samples were fabricated using a Dimatix DMP2800 piezoelectric inkjet printer to deposit successive layers on an optically transparent acetate over-head projector film of 100 μm thickness. Both polymers were processed as aqueous dispersions and were passed through 3.1 micron filters prior to printing to minimise the likehood of blocked nozzles. For the printing process, CLEVIOS^{TM} P Jet HC V2 PEDOT ink was purchased from HC Starck, Germany and the PPY ink was developed in-house specifically for processing with Dimatix piezoelectric printheads (Weng *et al.* 2011). Two thicknesses of PEDOT are fabricated (1 & 2 μm), while a single 1 μm thick sample of PPY is also fabricated. The fabricated samples can be seen in Figure 5.6, with the DC conductivities of the PEDOT and PPY being $\sigma_0 = 160$ S·cm^{-1} and 1 S·cm^{-1} respectively.

The resulting samples were non-uniform with obvious stripes in the films caused by the inkjet printing procedure employed. Much more uniform films are feasible using these materials and printing process but requires more optimisation and is beyond the scope of this thesis. A micrograph taken of the surface of the 1 μm thick PPY sample using a Philips XL40 scanning electron microscope (SEM) in secondary electron detection mode and a beam voltage of 20 kV is shown in Fig. 5.7. The stripes and gaps from the inkjet printing process can clearly be seen, with widths of approximately 120 and 55 μm, respectively.

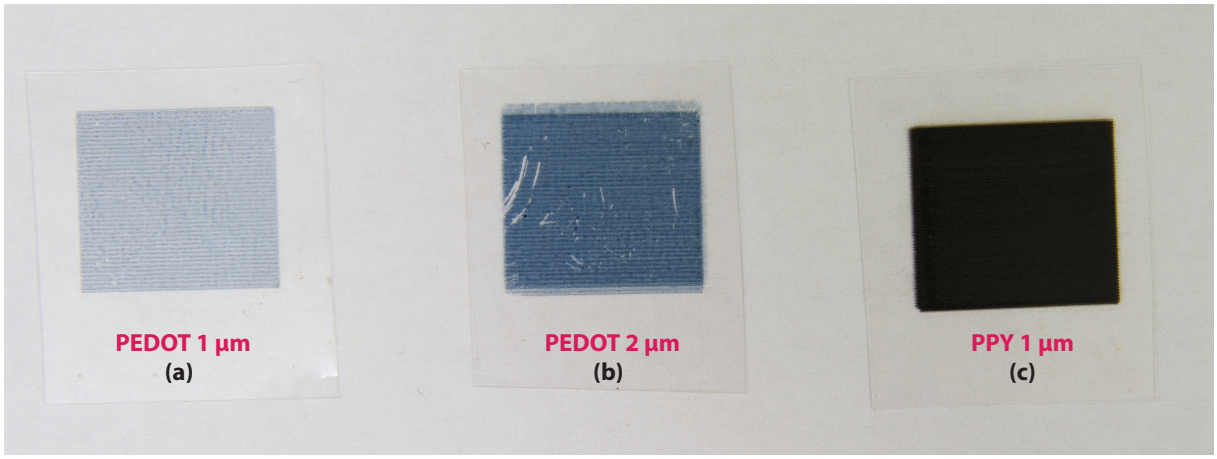

Figure 5.6. Photograph of the fabricated conductive polymers. From left to right, 1 μm and 2 μm thick PEDOT samples and PPY 1 μm in thickness. The conductive polymers are inkjet printed on top of a 100 μm thick acetate overhead projector sheet substrate. The printed squares of conductive polymers have 15 mm side length. The two PEDOT samples show slight non-uniformity, due to the inkjet printing process, and thus appear as an array of striped horizontal lines.

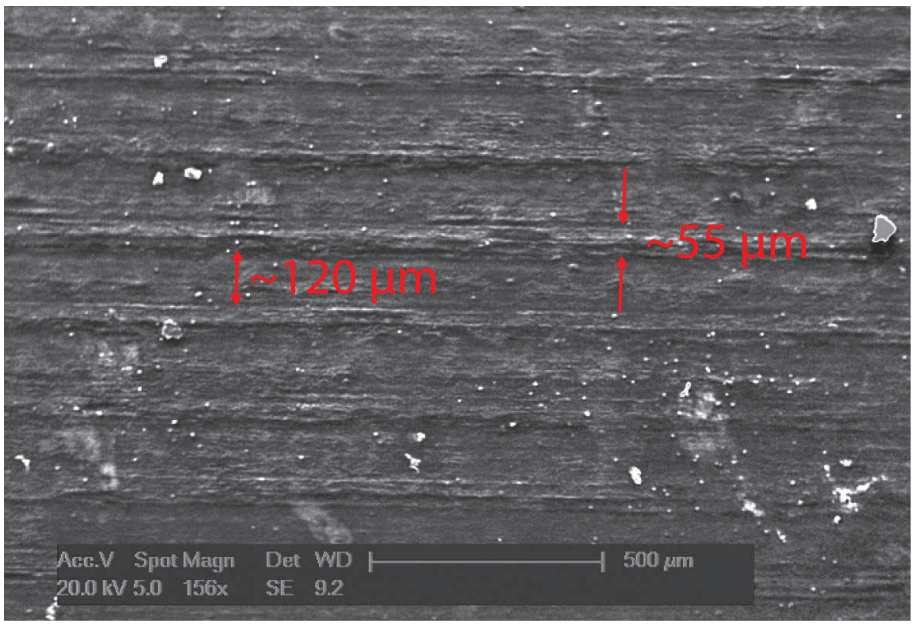

Figure 5.7. A SEM micrograph of the surface of the 1 μm thick PPY sample. As with the PEDOT samples, the stripes have a width of approximately 120 μm and gaps between stripes of approximately 55 μm. The micrograph is taken using a Philips XL40 SEM at a magnification of 156×.

5.5 Experimental Setup

All reflection and transmission experiments are performed in laboratory atmosphere at room temperature on a Menlo Systems TERA K15, fibre-coupled THz-TDS system, in the arrangement represented in Figure 5.8, which is similar to the Picometrix T-Ray 2000XP system discussed in Chapter 4 (Figure 4.5).The difference with the TERA K15 and the T-Ray 2000XP systems is that the TERA K15 system is not pumped with a 800 nm Ti:Sapphire laser, but rather an ultra-fast Erbium doped fibre laser operating with a center wavelength of 1.55 μm.

The TERA K15 allows for the tight focusing of the THz beam down to approximately 1 mm in diameter via four plano-convex lenses. A customized rotating stage is fabricated to allow for the detector and associated lenses to be swiveled together to the appropriate angle of incidence required by the sample orientation to measure either reflected or transmitted spectra. A sample holder is then mounted on top of the pivoting point of this mechanism. The samples are held in place in this holder using magnets, to ensure that each sample is mounted as flat as possible and that the error due to alignment is minimized when samples are swapped.

All subsequent measurements are performed with a horizontally polarized THz beam, and data is acquired for angles of incidence of $\varphi_0 = 35^\circ$ to 55°, in 5° increments with the angular position accurate to 0.1°.

5.6 Results

The measured transmission and reflection spectra for the different samples are shown in Figures 5.10-5.12 for the three samples considered, and compared to the theoretical model. The left-hand side graphs show the spectral variation of the transmission, reflection and absorption properties, whereas the graphs on the right-hand side illustrate the variations as a function of the angle of incidence, for a fixed frequency of 0.5 THz. The theoretical model obtained *a priori* from the measured refractive index of the samples can be compared to the frequency response of the samples and can predict the performance at varying angles of incidence at a fixed frequency (selected here as 0.5 THz). In particular, the measured data in transmittance shows a close match with the theoretical model for all three samples. In reflectance however, the 1 μm thick PEDOT and PPY samples show a noticeable divergence from the theoretical model at

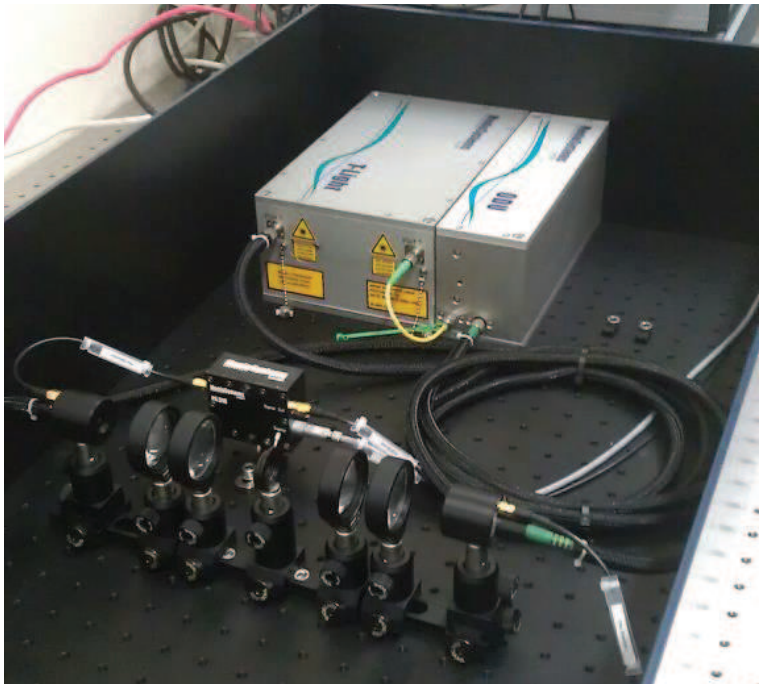

Figure 5.8. The Menlo Systems TERA K15 terahertz spectrometer. The aluminium box in the background consists of the 1.55 μm centre wavelength ultra-fast Erbium doped fibre laser with two output ports and an integrated optical delay stage. The foreground shows the THz detector and emitter on the far left and right respectively. Four lenses are used to focus the THz beam to a spot size of $\leq$ 10 mm in diameter, while the iris in the center denotes the point of focus where samples are placed. The fibre coupled heads allow for them to be configured at various angles of incidence to samples.

high frequencies. This discrepancy can be attributed to the surfaces of the samples not being perfectly optically flat, causing the reflected beam to be partially deflected and scattered away from the detector (Bandyopadhyay *et al.* 2007, Zurk *et al.* 2007).

The scattering can be explained by the stripes of the two 1 μm samples of both the PEDOT and PPY polymers. As shown in Figure 5.7, the stripes have a width of approximately 120 μm, while the gaps between stripes are approximately 55 μm wide. Optically, these stripes are visible for all the samples, however, the height of the stripes to the gaps is unknown, and could not be accurately measured. It is therefore assumed, that the 2 μm thick PEDOT sample has a more uniform coating than the other two samples. From Bandyopadhyay *et al.* (2007) and Zurk *et al.* (2007), the non-uniformity of samples, particularly with microscopic granularity can lead to higher than expected extinction even from the frequency range of 0.2 to 1.2 THz for certain samples, leading

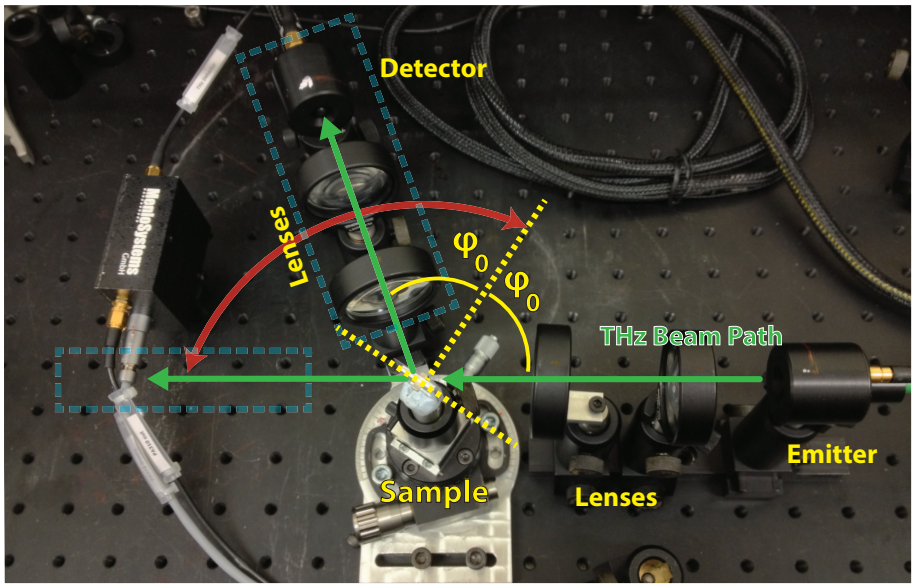

Figure 5.9. The Menlo Systems TERA K15 system with swivel mount. Photograph of the Menlo Systems THz-TDS system used for measurements. A special sample holder is fabricated, allowing the detector to be swivelled at the appropriate angle to measure both the reflected and transmitted spectra, depending on the angle of incidence on the sample. These positions are highlighted by the blue dashed boxes. The sample is also easily adjusted with a rotational stage accurate to 0.1°

to the scattering oberserved from the two 1 μm thick samples, which exihibit a higher than expected extinction from 0.4 THz onwards.

Also shown in Figures 5.10–5.12, the angular measurements from 35° to 55° angles of incidence (in 5° increments) at a frequency of 0.5 THz show a match with the theoretical model in transmittance. The transmittance and reflectance increases and decreases respectively as the angle of incidence approaches the Brewster angle near 70°.

The change in thickness of the PEDOT samples from 1 to 2 μm illustrated in Figures 5.10 & 5.11 shows the expected dependence on the layer thickness for a fixed DC conductivity, with the transmittance decreasing and the reflectance increasing for thicker both transmittance and reflectance (Ung *et al.* 2012, Walther *et al.* 2007, Tinkham 1956). Comparing now the 1 μm PEDOT sample to a PPY sample with the same thickness, but lower conductivity, an increase in transmittance and decrease in reflectance is observed, again conforming with theory. The polystyrene substrate itself presents a loss of approximately 5% across the measured frequency range, as well as a minor Fabry-Pérot interference component. Slight misalignment of the the sample in reflection causes the estimated loss to be greater than 5% per degree off from the exact angle

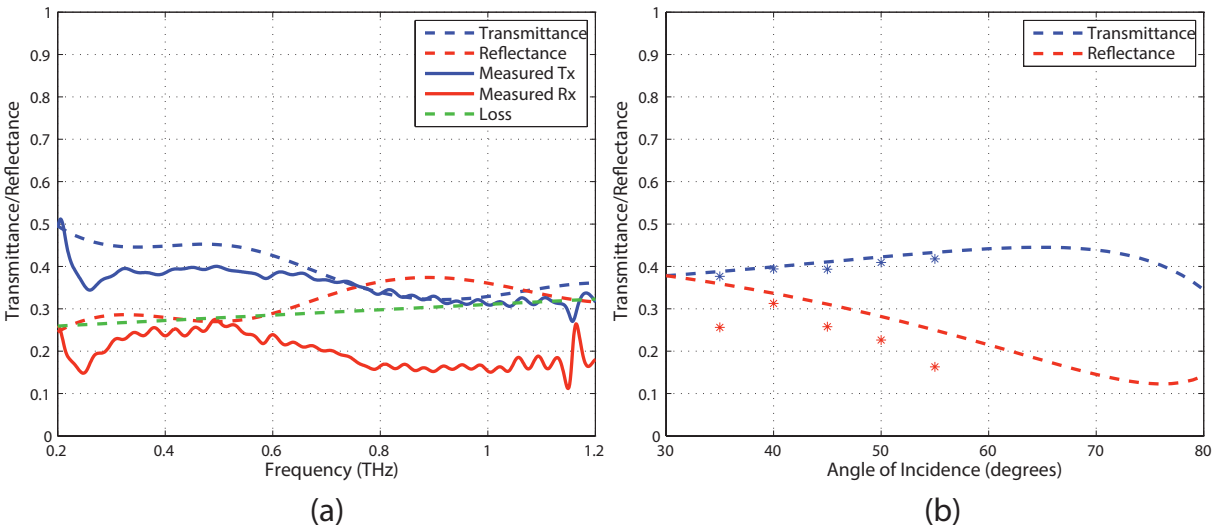

Figure 5.10. Reflection and transmission spectra of 1 μm thick PEDOT. Transmittance & reflectance plots of the PEDOT 1 μm thick sample. (a) Shows the transmittance & reflectance plot of the sample at 45° incidence, including the calculated loss, while (b) shows the angular dependence of the sample at varying angles of incidence at a fixed frequency of 0.5 THz. (a) Shows a slight variance from the reflectance theoretical model at frequencies above 0.6 THz, due to the non-uniformity of the sample and the substrate not being perfectly optically flat.

of incidence when optimising the experimental setup. A horizontal or vertical tilting of the sample results in a similar additional loss to the recorded data and therefore, multiple measurements are taken to ensure the maximum reflectance is recorded. The effect of the non-uniformity of the film (Figure 5.7) can be neglected in a good approximation, as orienting the samples horizontally or vertically in normal incidence transmission mode measurements show no significant differences, as shown in Figure 5.13.

5.7 Potential Improvements

As can be seen from the results, the conductive polymers yield higher losses than the silver coated beam splitter presented in Chapter 4. This combined with the small influence of Fabry-Pérot interference exhibited by the polystyrene film substrate are the major factors limiting its of use as a beam splitter for the THz range. Potential improvements can be made to the composition of both the PEDOT and PPY polymers used such that they yield less absorption in the THz range.

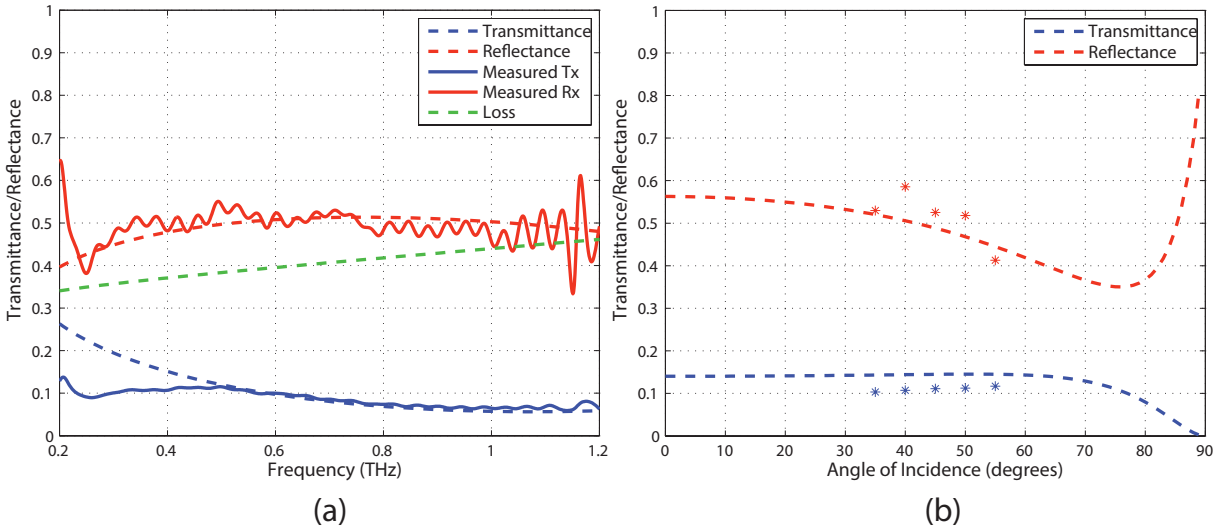

Figure 5.11. Reflection and transmission spectra of 2 μm thick PEDOT. Transmittance & reflectance plots of the PEDOT 2 μm thick sample. (a) Shows the transmittance & reflectance plot of the sample at 45° incidence, including the calculated loss, while (b) shows the angular dependence of the sample at varying angles of incidence at a fixed frequency of 0.5 THz. The measured data shows good agreement with the theoretical model, however the thicker 2 μm PEDOT coating shows a significantly higher loss than the 1 μm sample.

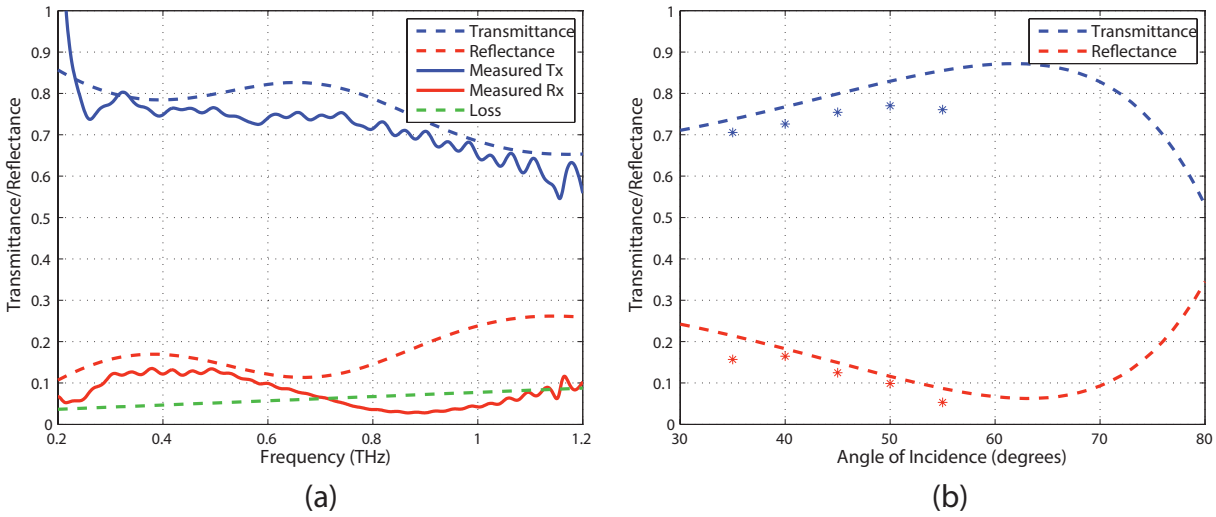

Figure 5.12. Reflection and transmission spectra of 1 μm Thick PPY. Transmittance & reflectance plots of the PPY 1 μm thick sample. (a) Shows the transmittance & reflectance plot of the sample at 45° incidence, including the calculated loss, while (b) shows the angular dependence of the sample at varying angles of incidence at a fixed frequency of 0.5 THz. Again, as for the 1 μm PEDOT coating, the 1 μm thick PPY coating show a degradation of the reflectance compared to expectations because of the imperfect flatness of the sample.

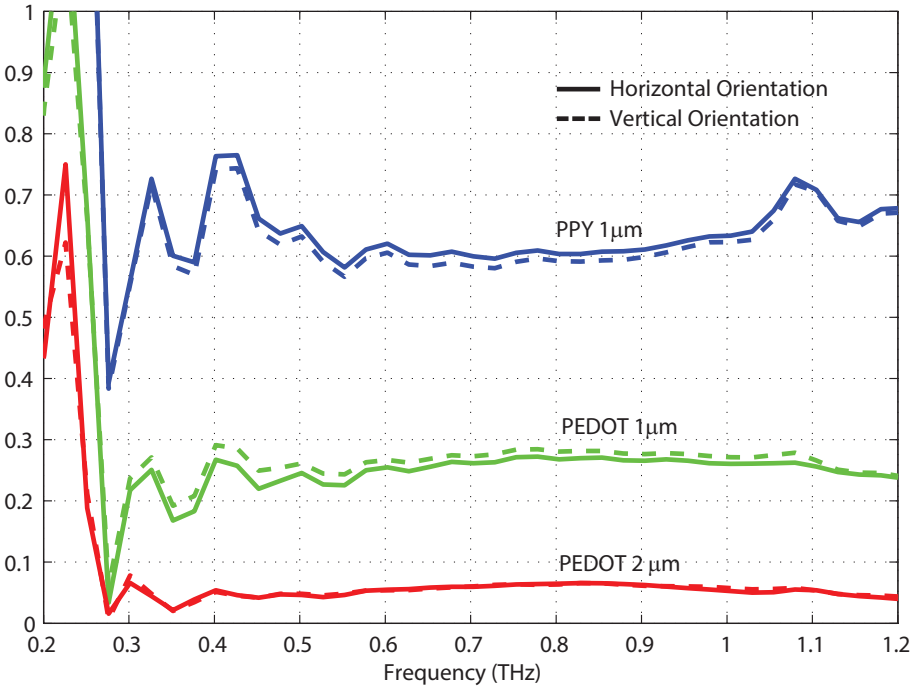

Figure 5.13. Transmittance of conductive polymers. Normal transmittance measurements of the three samples, PEDOT 1 & 2 μm and PPY in both horizontal and vertical sample orientations (solid and dashed curves respectively). The two differing orientations show no observable differences.

Further improvements of the printing procedure, or the use of alternative processing procedures such as bar-coating can provide decisive improvements over the proof-of-concept prototypes presented in this investigation to produce uniform coatings. The DC conductivities can also be controlled by varying the doping of the polymers, which adds additional control for splitting ratios, if the thickness is to be kept constant. There are some drawbacks to the currently available polymers, as they are not optimized for use at terahertz frequencies. As can be seen from the results in Figures 5.10-5.12, a light Fabry-Pérot interference component is arising from the 100 μm thick substrate, which also partially absorbs the incident terahertz radiation, leading to higher losses. These detrimental effects associated with the substrate can be mitigated by using a very thin substrate of *Teflon*, LDPE (low-density polyethylene) or Topas (cylic olefin copolymer), all of which show low absorption coefficients up to 3 THz (Ung *et al.* 2011). However changes in the fabrication process are required to achieve this. A further challenge is to keep the free-standing substrate optically flat, as minor changes to the flatness of the surface can cause higher than expected reflection loss through scattering, particularly at higher frequencies. Finally, an alternative to using a thin conductive layer coating

can use the techniques presented in a recent publication from Walker and Lewis (2012), where metallic inks could be deposited in a similar fashion to the presented method.

5.8 Chapter Summary

Here, PEDOT and PPY conductive polymer based beam splitters suitable for the THz spectrum are presented. The fabrication process, results together with potential improvements for the beam splitters are also discussed and provide a promising alternative to the previously presented silver conductive paint coated beam splitters, while still providing the same advantages of ratio-selectability and quick prototyping via inkjet printing, which accomodates finer tuning of layer thicknesses.

Once fabrication issues can be solved, where optically flat surfaces can be produced, and the conductive polymer is optimally selected for splitting ratios, conductive polymer based beam splitters show significant advantages. These include; more accurate control during fabrication over silver conductive paint based beam splitters, as well as, reduced Fabry-Pérot interference and predefined adjustment of power splitting ratios over HiZ Si wafers.

The use of conductive polymers are also an emerging field to build various THz based optical devices, which include filters, polarizers, beam splitters and also metamaterials. Metamaterials fabricated using the techniques discussed in this Chapter are also of great interest, as resonant structures can be easily fabricated using the inkjet printing process.

Chapter 6

Thesis Summary

THIS Chapter concludes the work covered in this Thesis. The continual development of THz-TDS systems, along with generation and detection techniques, particularly with higher power sources leads to a greater need for developing optics suitable for the THz range of frequencies. An additional need to decrease acquisition times and achieve higher SNRs in THz-TDS systems has led to the development of a simultaneous transmission and reflection system discussed in Chapter 3. Finally, two types of beam splitters have been developed, making use of thin conductive layers in Chapters 4 & 5. This Chapter also summarizes all the original contributions of this thesis.

6.1 Thesis Conclusions

This Thesis is aimed at developing a simultaneous dual-mode THz-TDS system and beam splitters for use in the THz range of frequencies. The initial introductory Chapter provides a background, motivation and some applications of THz radiation. This is followed by Chapter 2, which then details common generation and detection techniques used in THz-TDS systems, including high power techniques.

6.1.1 Review of THz-TDS

Chapter 3 details THz-TDS systems in both transmission and reflection geometries, built using the generation and detection techniques outlined in Chapter 2. Examples of common table-top transmission and reflection geometry systems are detailed, along with details on the system components and their functions in order to obtain data for THz-TDS. Along with this, equations used to calculate the complex refractive index from samples measured in both geometries are discussed.

6.1.2 Dual-Mode THz-TDS System

Chapter 3 details a novel dual-mode THz-TDS system, which improves upon common singular transmission and reflection mode systems. This new system is able to acquire both transmission and reflection spectra simultaneously, thus increasing SNR of the obtained signals and decreasing measurement times of samples. This system also enables samples with non-unity permeabilities, particularly with samples that contain sub-wavelength structures, such as metamaterials.

6.1.3 An Ultra-Thin Beam Splitter for the THz Range

Chapter 4 details the theoretical model of an ultra-thin conductive layer for the use as a THz beam splitter. A theoretical model detailing the relationship between the thickness of the conductive layer to the splitting ratio is presented. The design and fabrication is then discussed, with silver conductive paint used as the conductive layer, followed by the experimental measurements to confirm the theoretical model are then detailed. The results of the experiments are then compared with the silicon beam splitters that are in current use.

6.1.4 Conductive Polymer Based Beam Splitters for the THz Range

Building upon the methods and theory used in Chapter 4, Chapter 5 presents an evolution to the use of silver conductive paint as the conductive layer. The novel technique utilises conductive polymers as the conductive layer and varying its thickness enables adjustment of the power splitting ratios. An investigation of two conductive polymers, PEDOT and PPY are presented, along with two differing thicknesses for PEDOT. These conductive polymers add another layer of configuration, where their conductivities can be varied according to their fabrication, while also allowing for a more accurate thickness to be fabricated via inkjet printing.

6.1.5 Summary

This Thesis has presented an overview of THz radiation, including possible real-world applications. Generation and detection methods are detailed, and then used in TDS setups, which are also outlined.

6.2 Summary of Original Contributions

The key contributions for this Thesis as summarised below:

1. **Simultaneous dual-mode THz-TDS system**
   As an advancement of THz-TDS systems to decrease both measurement times and to increase measured SNR, a dual-mode THz-TDS system where both transmitted and reflected spectra are measured simultaneously is presented as part of the main contributions of this thesis (Ung *et al.* 2013b). This system is validated by experimental results in multiple test scenarios.

2. **An ultra-thin THz beam splitter**
   Silicon wafers have traditionally been used as beam splitters in the THz range of frequencies. These beam splitters have fixed splitting ratios and suffer greatly from Fabry-Pérot interference due to their high refractive index. One of this thesis' contributions is a novel and inexpensive method for fabricating THz beam splitters using silver paint layers with thicknesses less than the skin-depth

(Ung *et al.* 2012). Any desired splitting ratio can be easily obtained according to the thickness of the silver paint layer, which can be produced using rapid prototyping techniques. The ultra-thin layer of paint and substrate also improves on the silicon beam splitters by having minimal Fabry-Pérot interference.

3. **Conductive polymers for the THz range of frequencies**
   A further contribution and improvement over the presented ultra-thin THz beam splitters is the possibility of using conductive polymers as an alternative to silver conductive paint (Ung *et al.* 2013a). Conductive polymers provide a more versatile material for fabrication as their conductivities can be altered, while the thickness of layers can be more accurately controlled by the use of inkjet printing.

The ancillary contributions of this Thesis presented in the Appendix are summarised by the following:

1. **Dual scanning THz-TDS system**
   A two-fold decrease in acquisition times of both the reference and sample in transmission mode THz-TDS systems is achieved by the combining of two THz-TDS systems with a single optical delay stage (Ung *et al.* 2008). This work also has additional benefits of lowering the overall cost of two separate transmission mode systems and allowing more flexible use of the two systems.

2. **Mini-investigation into food quality control using THz-TDS**
   Health scares with food products are ever increasing. Here, this contribution looks into baby milk powder (Ung *et al.* 2010), and the hydrogenation of cooking oils (Ung *et al.* 2009). Baby milk powder has previously shown signs of lacing with two chemicals, melamine and cyanuric acid, which if injested in a large enough quantity may be potentially fatal. Preliminary work is conducted to investigate detection of mixtures of these chemicals in baby milk powder and the minimal amounts of lacing for detection. Various preceived healthy and unhealthy saturated and unsaturated cooking oils are also investigated via THz-TDS both before cooking in a conventional frying pan and afterwards. Distinct differences can be observed between the oils following that of published literature (Li *et al.* 2008, Li 2010).

3. **Mini-investigation into security applications for THz-TDS**
   Finally, a complementary contribution for possible security applications of THz-TDS is investigated. A simulation of a physical plastic suitcase with clothing

is contaminated with a detectable chemical and investigated in measurements (Ung *et al.* 2006). Various plastic materials are also investigated, each showing the same similar spectra when contaminated with the chemical.

These contributions enable a decrease in scanning time with lower noise, along with the possibilities to image, characterise and investigate materials that would otherwise require separate transmission and reflection mode systems. The beam splitters presented enable high-power sources to monitor the quality and power of their signal outputs and power multiple systems, while also providing more flexibility in building THz systems. Finally, practical applications of using THz-TDS in both testing food quality and possible security screening can be further developed with the body of work presented in this thesis.

6.3 Future Work

6.3.1 Dual-Mode THz-TDS System

Currently, the limiting factor of the presented dual-mode system is the dumping of 50% of the generated THz radiation when using the silicon beam splitter. Further work can be performed by manipulating the currently used beam splitter to be polarization dependent. Then, if the polarization of the reflected radiation from a sample or reference mirror is rotated, losses can also be reduced. Additionally, this current system only uses PCAs for both generation and detection. Greater sensitivity can be obtained by the use of EO detection for both the transmission and reflection detectors, while the emitter can be adapted for a high power generation source.

6.3.2 Beam Splitters for the THz Range

Further work in increasing the accuracy of fabrication for the silver conductive paint coated beam splitters is necessary, with a possible alternative to spray coating being inkjet printing the paint onto a suitable substrate. This allows for more accurately fabricated splitting ratios. The conductive polymers also require more development to be suitable for use in the THz range of frequencies. The substrate thickness needs to be decreased and less absorptive, while the polymers can also be adapted to vary their conductivities.

Appendix A

Dual Scanning THz-TDS System

TO decrease acquistion times and improve flexibility from a transmission mode THz-TDS system, two independent THz-TDS systems are combined using a single time delay stage. This allows for both systems to operate simultaneously, where either a reference and sample measurement or two differing samples can be measured. This potentially gives rise to a higher SNR when the spectra of both systems are normalized.

A.1 Introduction

Chapter 3 presented an in depth review of THz-TDS systems. These systems are limited by the optical delay stage, where this mechanical delay stage limits the speed of acquisition as well as trade-offs with SNR (Jepsen and Fischer 2005, Withayachumnankul *et al.* 2008). The presented system here aims to decrease acquisition times, improve SNR and lower the overall cost of implementing two transmission mode THz-TDS systems by using a single delay stage for both systems.

As it is preferable to gather many averages of both samples and reference data to minimise noise due to laser fluctuations and imprecisions from the delay stage, a longer time interval is needed for each data point captured on the delay stage. The presented simultaneous dual scanning system configuration enables both measured data of the sample and reference to be acquired simultaneously by using both systems, or adds additional flexibility during measurements for two separate samples to be measured simultaneously. The acquired data is then normalized to the system with the lowest amplitude spectra.

A.2 Experimental Setup

A single optical delay stage is used, with both systems designed around this stage. Space constraints from the optical table are taken into account when designing the overall layout of the system, such that the optical path lengths of both systems are equal. For this design, two transmission mode systems are used. However, it may be also be possible to design a setup where two reflection mode systems are used. Once the placement of the optical delay stage is defined, the same optical components are then arranged in the same manner as that outlined in Chapter 3 for transmission mode systems. The difference is that an additional optical beam splitter is added to the probe beam path near the optical delay stage, such that it can be shared between both systems. The choice of emitters and detectors for the two combined systems is arbitary, as the captured spectras are normalized to the spectra with the lowest amplitude.

With the presented setup, one system makes use of dipole antennas for both emission and detection, while the complementary system makes use of a bow-tie antenna for emission and EO detection (Figure A.1). Figure A.2 shows the overal setup, with both systems using a single optical delay stage, while Figure A.3 shows a schematic diagram of the setup.

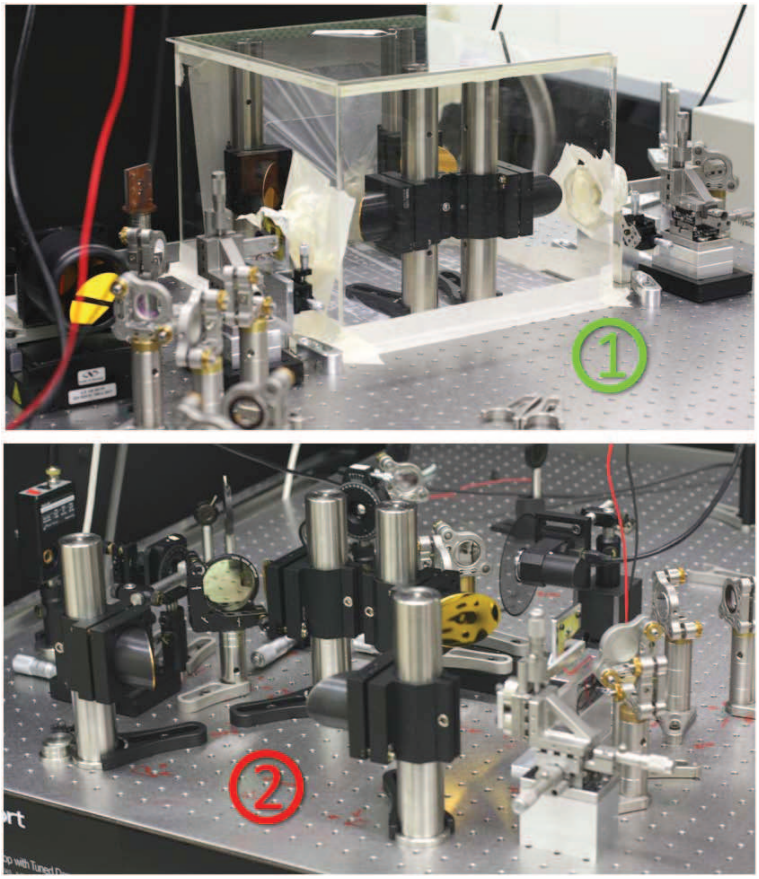

Figure A.1. Photograph of the two individual systems in the dual scanning setup. (1) Shows one system that has two PCAs used as both as an emitter and detector, while (2) shows the complementary system using a bow-tie PCA as an emitter and EO detection. (2) Also contains an additional manual optical delay path to fine tune the overlap of the pulses generated by both systems.

To control the setup, a LabView script is used to control both the movement of the optical delay stage, which is synchronised with the output from a lock-in amplifier connected to the detectors.

A.3 Results

The overall setup performs as expected, both systems have the ability to operate either independantly or in parallel, allowing for a two-fold decrease in acquisition time. Although there is an obivous observable difference between the two captured spectra of both systems, this difference in sprectral amplitudes are due to the differing emitters and detectors used by both systems, particularly with the bandwidth limitation of the bow-tie PCA used in one of the systems. The captured time-domain pulses and spectra

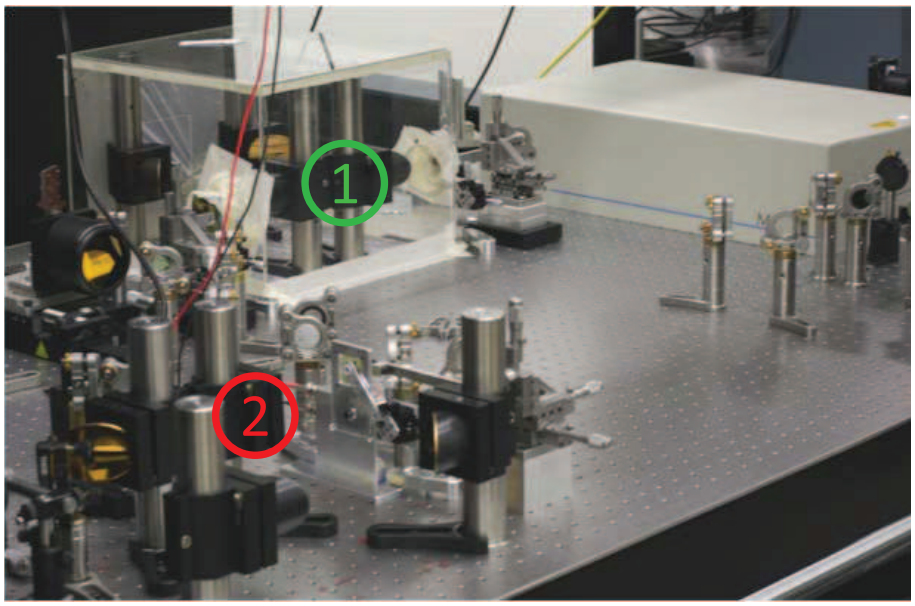

Figure A.2. Photograph of the dual scanning THz-TDS system setup. This photo shows two transmission mode THz-TDS systems (labeled as (1) & (2)), sharing a single delay stage, allowing for faster acquisition times, lower costs and greater measurement flexibility.

of the two systems can be seen in Figure A.4. The frequency spectra of the setup needs to be normalised to that of the lowest performing system.

As the overlap of both generated pulses of systems can be adjusted to a high precision, the phase data for samples can be retained, thus allowing for a real-time output of the refractive index and absorption coefficient if the thickness of the sample is known. This then allows for the possibility of real-time classification of measured samples.

A.4 Future Work

As the major limitation of this setup is the weakest spectral amplitude of either system employed, both systems should ideally use the same emitters and detectors, which will help in minimising the differences in amplitude and dispersion of the captured THz pulses. This will then remove the need for normalising the spectra accquired by both systems and remove additional computational overheads.

A.5 Chapter Summary

This Chapter has presented a simultaneous dual scanning THz-TDS setup, where two transmission mode THz-TDS systems share a single optical delay stage. The results

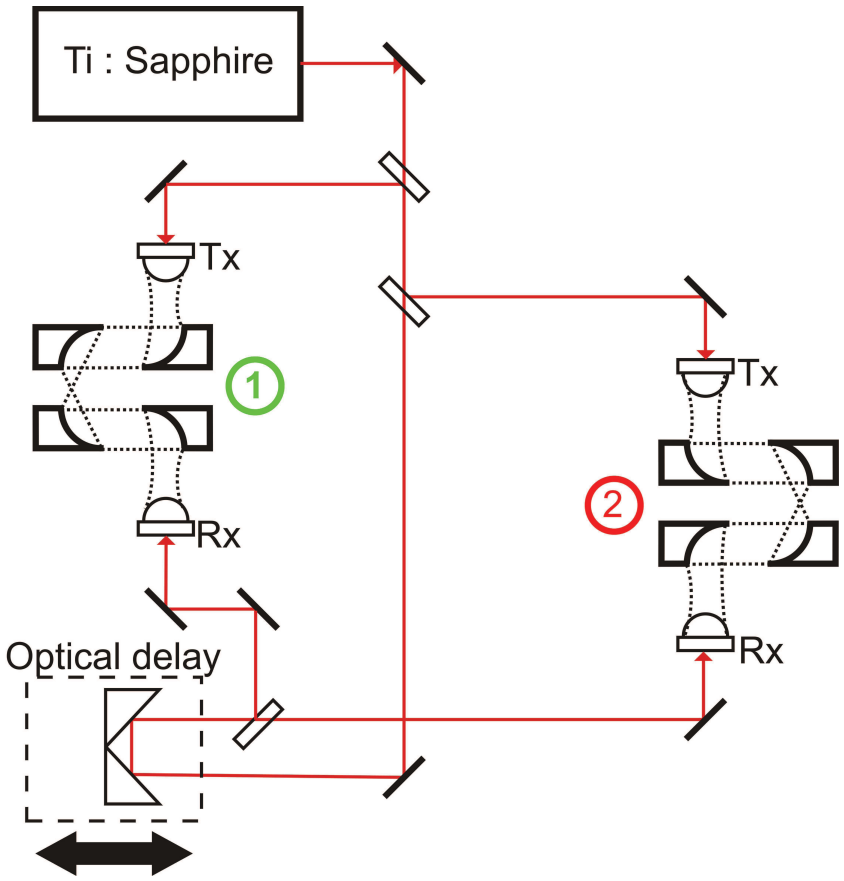

Figure A.3. Schematic of the dual scanning THz-TDS system setup. This schematic shows a simplied layour of the dual scanning setup, where two individual THz-TDS systems share the same optical delay stage. An additional optical beam splitter is used to share the two laser probe paths between the two systems.

show a two-fold decrease in acquisition time of samples and references due to parallel scanning, while lowering the costs of building two individual THz-TDS systems and adding additional flexibility for measurements.

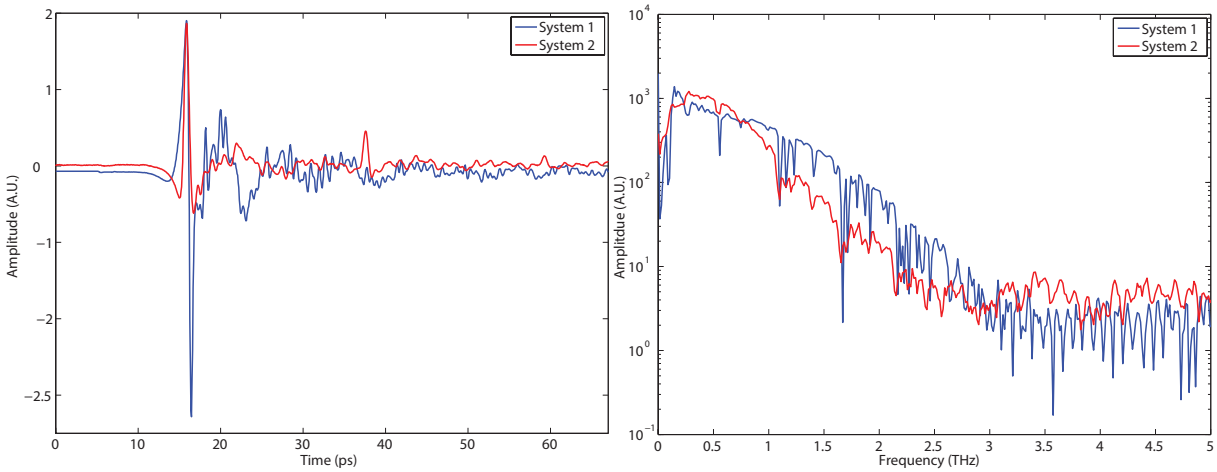

Figure A.4. The time-domain and frequency reference spectra of the dual scanning system. The time-domain pulses overlap with a high precision, allowing the accurate retention of phase data. The frequency spectra of the two systems have an observable difference, due to the different emitters and detectors used in both systems. To make use of the systems in parallel, the acquired frequency spectra is normalised to the lowest amplitude.

Appendix B

Food Quality Control using THz-TDS

RECENTLY, there have been many reports of contamination in the food industry, particularly with baby milk powder. This Chapter explores the possibility of using THz-TDS to detect contamination of baby milk powder. In addition, the hydrogenation of saturated and unsaturated oils and fats used in common household cooking is investigated.

B.1 Introduction

Terahertz time-domain spectroscopy has shown significant promise in characterising biomolecules, proteins and pharmaceuticals (Markelz 2008, Parrott *et al.* 2011). This shows potential to be adapted to the food industry, where products may be manufactured into dry powders. In particular, for baby milk powder, where the produced powder is dry and consumers are concerned about possible contamination. In addition, an investigation into saturated and unsaturated oils and fats for cooking shows promise, as they are relatively transparent to THz radiation. Preliminary investigations into THz applications as a technique for food quality control of both baby milk powder and oils and fats are explored in the following sections.

B.2 Milk Powder

B.2.1 Motivation

Recent contamination of baby milk powder in China in 2008 (MacLeod 2007, Wang 2008), has lead to widespread concern. The contaminants, melamine and cyanuric acid, were added to the milk powder to increase protein counts, which are typically measured by nitrogen content (MacLeod 2007, Wang 2008). These contaminants in high enough dosages can lead to acute renal failure (Turnipseed *et al.* 2008), and thus is of great concern to families with infants. Melamine has been characterised previously by Harsha *et al.* (2008) and Mauer *et al.* (2009) at THz and IR frequencies respectively, which leads to the possibility of detection in mixtures together with milk powder and cyanuric acid.

B.2.2 Experimental Setup

Samples of milk powder, melamine and cyanuric acid are mixed together with a buffer agent, polyethylene and pressed into 13 mm diameter pellets under 10 tonnes of force. The sample powders are purchased from Sigma Aldrich, M2659 and 185809, for melamine and cyanuric acid respectively. The pressed pellets in total each weighed 1 g, consisting of a mixture of milk powder and polyethylene buffer and melamine and cyanuric acid mixtures.

These pellets are then measured in a Thermo Scientific Nicolet 6700 FTIR system (Figure B.1), with a diamond windows at room temperature in ambient air, with the detector cryogenically cooled by liquid nitrogen. Data is collected from the range of 50 to 5000 cm^{-1} wave numbers using Omnic version 7.4 software in absorbance mode with automatic atmospheric, baseline and H_2O and CO_2 corrections. The pellets are pressed onto the measurement window via a 45 PSI press and 32 samples are collected per measurement. Several measurements are performed on multiple pellets, the final data was then averaged out to obtain the final spectra.

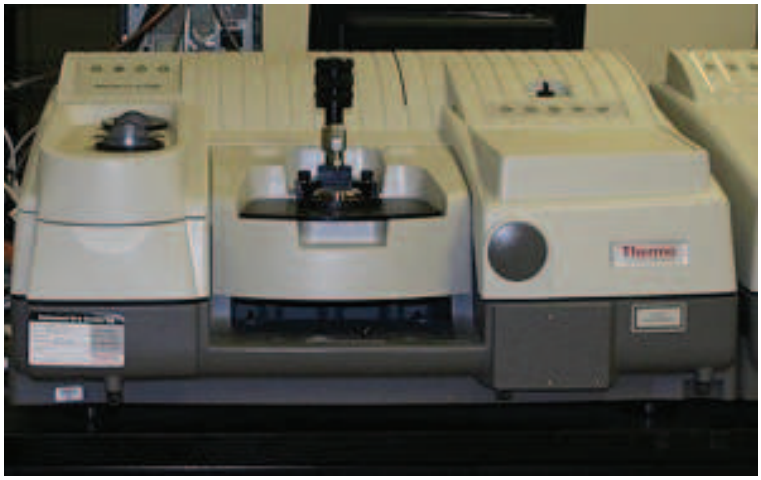

Figure B.1. Thermo Scientific Nicolet 6700 FTIR system. The FTIR system used for the baby milk powder measurements. The centre of the system contains the press to push samples down onto the measurement window.

B.2.3 Results

The samples measured containing melamine and/or cyanuric acid show distinct differences to the uncontaminated baby milk powder sample B.2. Samples containing melamine contamination show differing spectral features to the uncontaminated sample at around 1500 cm^{-1} wavenumbers, while at higher wavenumbers, a much more significant absorption is apparent. Samples which contain cyanuric acid show many more distinct absorption peaks across the measured spectra.

These measurements show significant promise, leading towards the possibility of integration across a rolling production line, where the milk powder could be scanned in realtime to detect contamination and ensure that product batches meet strict safety requirements for quality control.

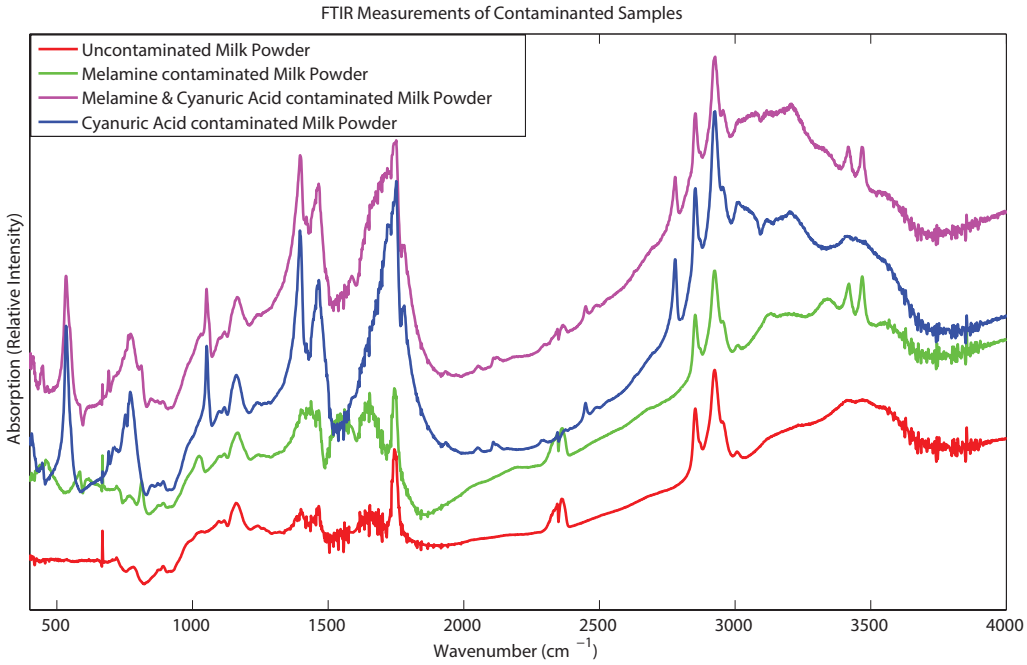

Figure B.2. FITR measurements of contaminated milk powder. The FTIR absorption spectra of contaminated and uncontaminated baby milk powder. The curves have been offset for easier viewing. A noticeable difference is observed with samples laced with melamine and cyanuric acid, key components to the baby milk powder incident that occurred in China.

B.3 Oils and Fats

B.3.1 Motivation

Hydrogenated trans fatty acids in saturated fats pose significant health concerns with frequent prolonged consumption. Long-term consumption of hydrogenated trans fatty acids can lead to significant health problems such as high cholesterol and heart disease (Lichtenstein *et al.* 1999, Jang *et al.* 2005). These concerns are particularly prevalent when cooking food using such fats or oils. In addition to this, unsaturated fats and oils may become saturated during the cooking process in which heat may be a significant factor and lead to higher cholesterol levels in the human body.

This Section explores the possibility of THz-TDS as a method to investigate the hydrogenation of fats and oils by measuring uncooked and cooked samples and determining if a difference can be observed between known saturated and unsaturated fats and oils, as similarly published in literature (Li *et al.* 2008, Li 2010).

B.3.2 Experimental Setup

Common off-the-shelf oil is used in these experiments. The oils are taken directly from the bottle as a baseline reference sample for comparison between oils that had undergone additional heating. Both the heated and unheated samples are placed into a freezer to allow for easier preparation of sample, and are then added to a 1:1 weight ratio with polyethylene powder. The mixture is combined to form a slurry, which is then allowed to return to room temperature before being injected into a liquid cell with a thickness of 580 μm. Finally the liquid cell is placed into a THz-TDS system in transmission geometry and data is then collected.

The heated samples are treated by heat from a flying pan heated on a conventional gas stove top. The frying pan is first preheated for 1 minute, then the fat or oil is placed into the pan and heated for 5 minutes. The oil is then allowed to return to room temperature before sample preparation. This is then repeated for each sample.

B.3.3 Results

The fat and oils did not exhibit any easily observable differences in colour, smell viscosity after heating. However, the results shown from measurements of the slurries in Figures B.3 to B.5, show the heated canola oil (ie. rapeseed oil) developing a higher absorption than that of the sample taken directly from the container, while it is arguable that the other samples of fat and peanut oils potentially have a higher absorption.

A more comprehensive investigation as to the cause of the higher absorption observed in the canola oil is required, but beyond the scope of this Section. In particular studies are required to determine whether this higher absorption is due to saturation of the oils or other factors leading to a change in molecular structure or another cause altogether. The viability of using THz-TDS to detect the hydrogenation of the oils appears feasible, if the source of the increase in absorption can be clearly identified and linked.

B.4 Chapter Summary

Preliminary investigations into THz applications for food quality control of baby milk powder and oils and fats for cooking are conducted in this Chapter. Measurements show that contamination by melamine and cyanuric acid in baby milk powder can be

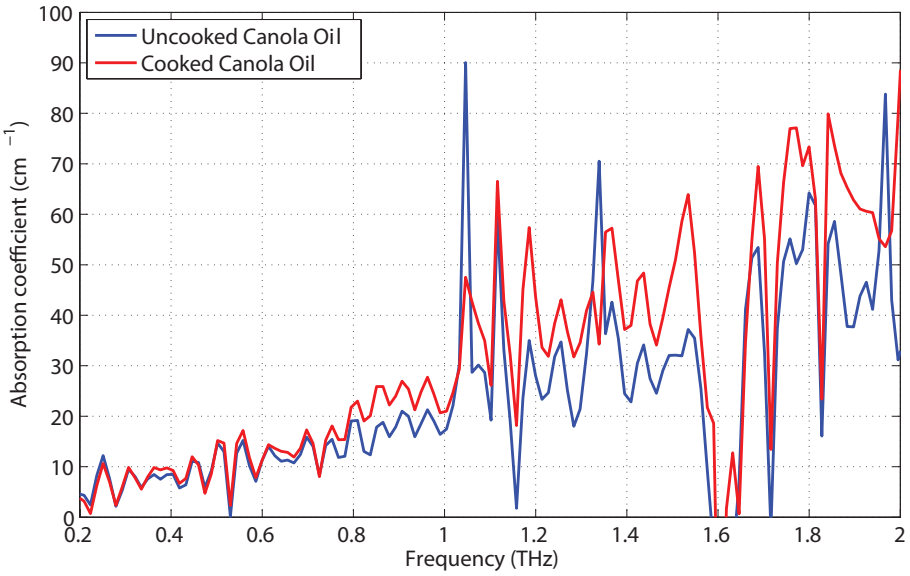

Figure B.3. Absorption of canola oil. The absorption curves of cooked and uncooked canola oil. An observable difference in absorption is apparent between samples taken directly from the bottle and after heating in a frying pan on a conventional gas top stove above 150°C.

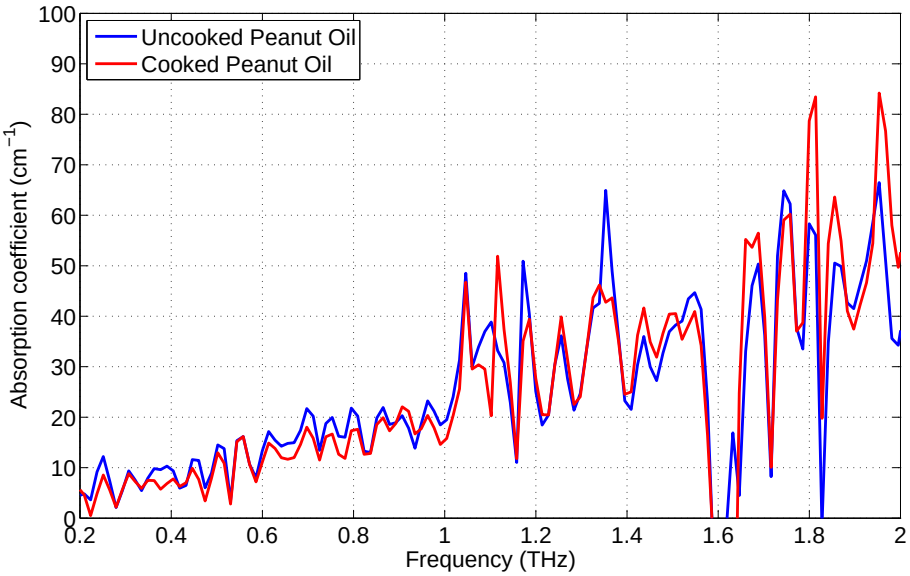

Figure B.4. Absorption of peanut oil. The absorption curves of cooked and uncooked peanut oil. No observable differences can be seen between samples taken directly from the bottle and after heating in a frying pan on a conventional gas top stove above 150°C.

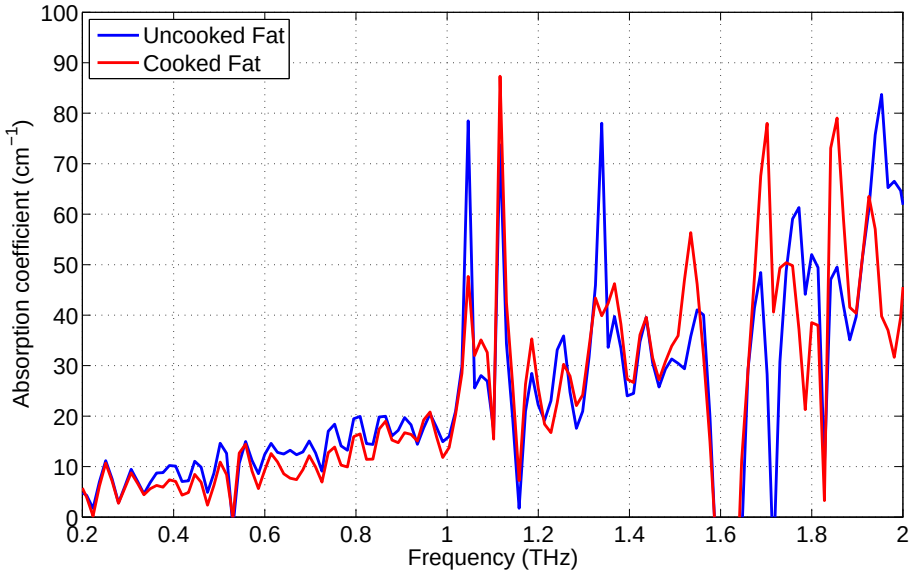

Figure B.5. Absorption of solid fat. The absorption curves of cooked and uncooked solid fat. Similar to the peanut oil samples, no observable differences can be seen between samples taken directly from the packaging and after heating in a frying pan on a conventional gas top stove above 150°C.

observed, while observable differences in absorption coefficient can be seen between a cooked and uncooked canola oil.

Appendix C

Security applications for THz-TDS

TERAHERTZ time-domain spectroscopy can be applied in real-world applications to perform security screening of illicit substances, explosives and hidden weapons. The non-ionising and broadband nature of THz-TDS enables these substances to be classified by absorption curves to provide clear identification. This Appendix outlines the potential for security screening of common luggage.

C.1 Introduction

Terahertz spectroscopy has many advantages over current techniques to detect illicit or hazardous substances. The non-invasive and non-destructive nature of measurements means that samples can be probed safely, and without human interaction. As mentioned in Chapter 1, THz-TDS has been implemented in various security applications including, he possibility of detecting hidden explosives, the possible detection of illicit narcotics and also biological weapons. Here in this Chapter, the possibility of implementing THz-TDS for security screening of common bags or suitcases is investigated, providing an addition or alternative to X-ray scanners. A simplified sample structure is used to simulate common plastic materials to construct bags and suitcases, while clothing is simulated by a sheet of cotton. Lactose is then spread onto samples of the cotton sheet to determine if the detection of trace contaminants can be classified compared with clean samples.

C.2 Experimental Setup

Initially, single sheets of nylon, polycarbonate, polyethylene purchased from local suppliers (Acrilix Plastics Pty. Ltd and Mulford Plastics Pty. Ltd.) and cotton are measured to determine their absorption coefficients and to ensure that they were opaque to THz radiation (Table C.1). Two sheets of the plastics are then sandwiched together with a cotton sheet in the middle to form the simulated suitcase sample. The combined sample is then placed into a Picometrix T-Ray 2000XP THz-TDS system for measurements in transmission mode. After this inital sample is measured, it is compared to an air reference, to see the absorption of the sample. The cotton sheet is then lathered with alpha-lactose slurry (of which the absorption spectra can be seen in Figure C.2) and left to dry before being sandwiched by the plastic sheets and measured. This sample is then compared with the initial clean sample of sandwiched cotton and a sample of pure alpha-lactose, to determine if the lactose can be detected.

C.3 Detection

The initial experiments characterising clean samples are taken to ensure that they are opaque to the incident THz radiation. These measurements show no distinct absorption features from the usable bandwidth range of 0.2 to 1 THz (blue curve, Figure C.3).

Material	Thickness (mm)	Absorption Coefficient (cm^{-1})
Nylon	3.205	0.400
Polycarbonate	2.057	6.955
Polyethylene	4.562	0.515
Cotton	0.442	3.755

Table C.1. Absorption of various plastics and cotton. The absorption coefficients of nylon, polycarbonate, polyethylene and cotton used for the preliminary investigation of security screening of bags and suitcases by THz-TDS.

The samples contaminated with lactose applied to the cotton layer however show the distinct spectral feature of lactose from Figure C.2, where an absorption peak at approximately 0.55 THz can clearly be seen from the red curve in Figure C.3. This absorption peak is somewhat attenuated compared to the pure lactose spectra in Figure C.2, however, there is less lactose present in the applied slurry, and contributions from Fresnel reflections at the multiple interfaces of the sample are potentially contributing factors to this smaller absorption peak.

C.4 Summary

This Appendix discusses the possibility of using THz-TDS to perform security screening of common bags and suitcases. Simulated samples are constructed from commonly used plastics such as, nylon, polycarbonate and polyethylene to simulate the outer layer of a bag or suitcase, while a cotton layer is used to represent the clothing contained inside. Measurements are then performed on clean samples, showing no distinct absorption features, after which the cotton layer is contaminated with lactose and measured again. The contaminated samples showed the distinct absorption features of lactose, indicating that THz-TDS may have the potential to perform security screening for secure environments, complementing the existing systems currently in use.

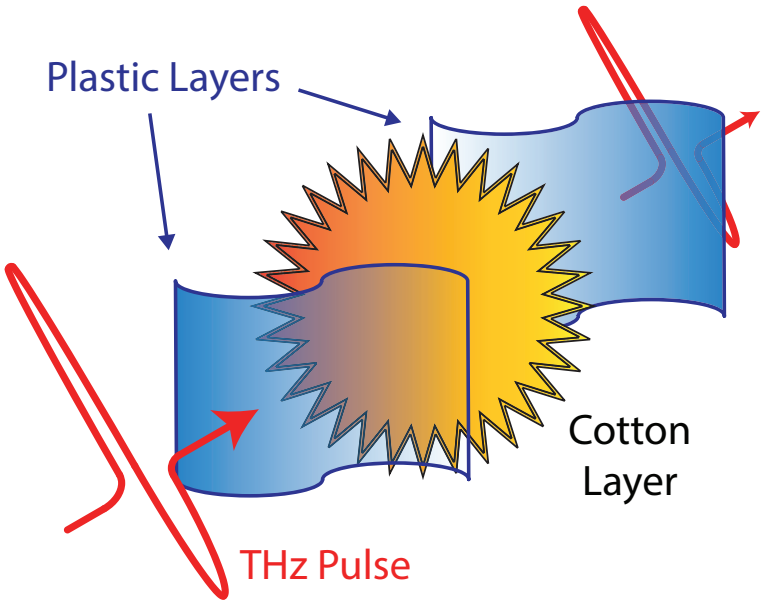

Figure C.1. Diagram of how the sample is measured. Two sheets of plastic (blue) sandwich the cotton sheet layer (orange). A clean sample is initially measured, followed by a sample contaminated with lactose. The samples are both measured in a transmission mode THz-TDS system, with the front face of the sample placed at normal incidence to the THz beam.

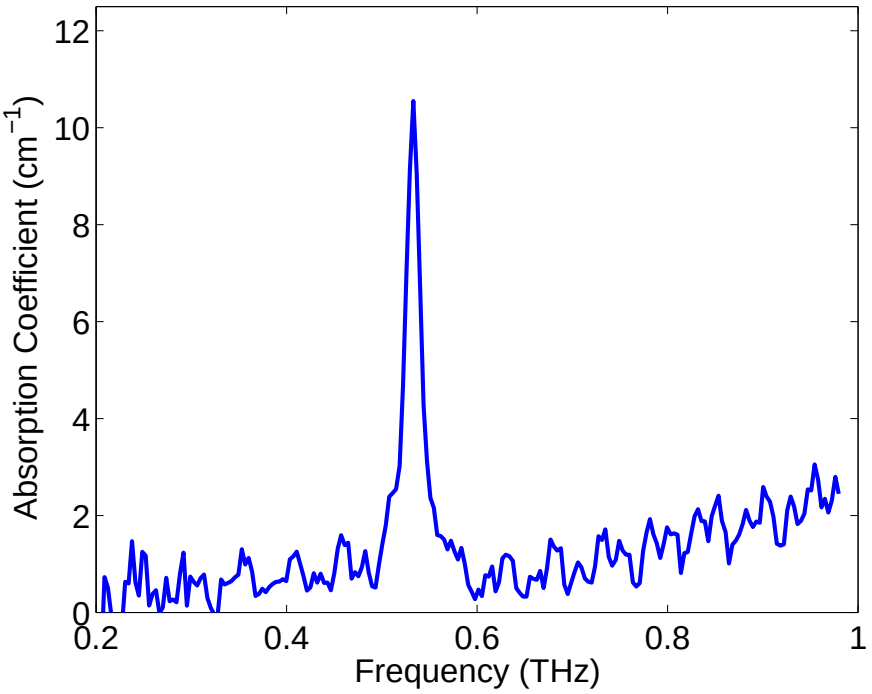

Figure C.2. Absorption spectra of lactose. The measured absorption spectra of alpha-lactose from a pressed pellet mixed with polyethylene. A distinct absorption peak is clearly observed at approximately 0.55 THz.

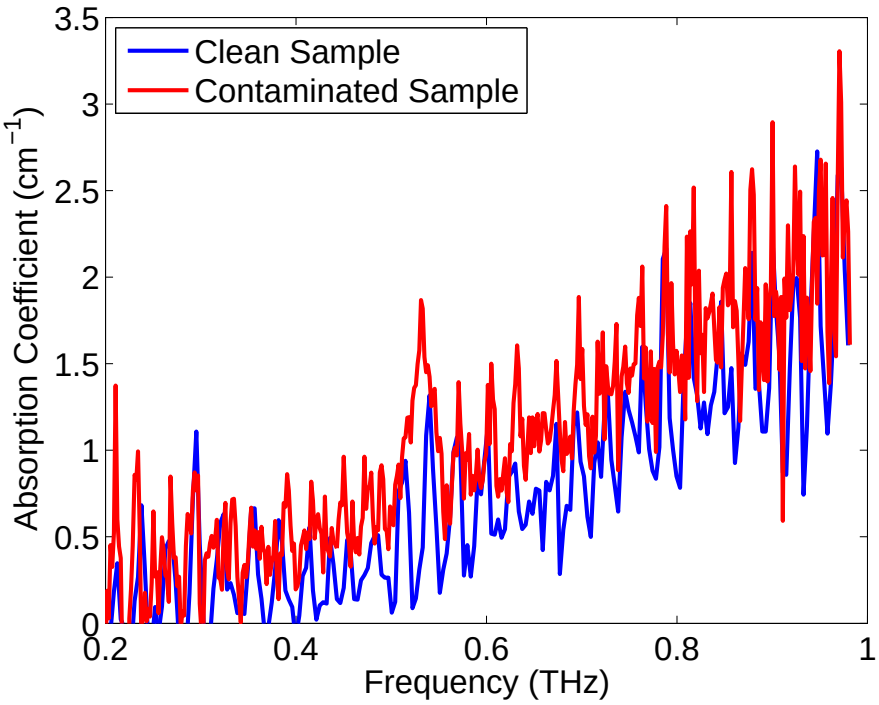

Figure C.3. Absorption spectra of clean and contaminated samples. The blue curve of the clean sample sample shows no distinguishable absorption peaks, while the red curve depicting the absorption of the contaminated sample shows the distinct absorption peak of lactose at approximately 0.55 THz. Only samples consisting of nylon polymer layers are shown here for ease of viewing.

Appendix D

Second Harmonic Generation

MUCH like in electronics, where the frequencies of signals can be manipulated by multipliers to increase or decrease the input frequency, light can also be manipulated in the same fashion. In this Appendix, the generation of the second harmonic of an infrared laser to ultravoilet is discussed.

D.1 Introduction

Second Harmonic Generation (SHG) is typically used to frequency double infrared lasers operating with a wavelength of 1064 nm to 532 nm, an intense green wavelength used in pump lasers for many applications, including the pump laser for Ti:Sapphire oscillators (Moulton 1986), which are commonly used for THz generation.

The process of SHG is fundamental in the generation of THz radiation by air plasma, where a non-linear optical crystal is used. Other possible THz emission sources, such as higher bandgap semiconductors show promise which possible higher conversion efficiencies. These semiconductors need to be pumped with shorter wavelength photons. Ultra-fast lasers operating with such centre wavelengths are not commericial available, and thus resort to SHG to achieve these required wavelengths.

The first discovery of SHG occurred in 1961 by Franken *et al.* (1961), where a ruby laser with a wavelength of 694 nm was shone onto a quartz crystal producing an output in the UV range at 347 nm. From then on, many other groups continued with the work using many addition non-linear crystals for SHG. Many of these crystals are the same as those used for Optical Rectification (Section 2.1.3), such as KDP and $LiNbO_3$ (Bass and Andringa 1967, Shapiro 1968, Comly and Garmire 1968, Glenn 1969). More recently however, other crystals have been developed to increase the conversion efficiency of SHG (Nikogosyan and Gurzadyan 1987), of particular interest in this Chapter is β radiation damaged barium borate (β-Ba_2BO_4), otherwise known as BBO, which was first used for SHG by Ishida and Yajima (1987). Further reading on the crystals used for SHG can be found from Nikogosyan (1991).

A general explanation of how SHG occurs can be explained by the combination of two photons of the same energy combining in a non-linear medium, resulting in the generation of a single photon at twice the energy, and thus twice the frequency of the original photons. This occurs similarly to optical rectification detailed in Chapter 2, where a second order non-linear polarization is generated by the $\chi^{(2)}$ non-linearity of the crystal medium (Equation 2.5), and thus radiates an electromagnetic wave at double the frequency (Glenn 1969).

D.2 Motivation

The motivation for investigating the SHG of the Ti:Sapphire laser is to achieve an equivalent wavelength to the bandgap of GaN discussed in Section 2.1.1 to achieve higher

power and higher SNR generated THz radiation from a PCA at a relatively low increase in cost.

In this case, a BBO crystal is selected due to the crystal having a high non-linear constant, a high conversion efficiency compared to other crystals, its ease of handling and high damage threshold (Ishida and Yajima 1987, Nikogosyan 1991).

D.3 Optical Setup

The optical arrangement for SHG, requires the use of a lens to focus the incident infrared laser beam onto the BBO crystal to generate a high enough intensity for the second harmonic to be generated. An additional lens on the backside of the BBO crystal is then used to re-collimate the beam. The anti-reflection coating of these lenses need to be matched to both the input and output wavelengths for maximum conversion efficiency. A photograph of this setup can be seen in Figure D.1, while the output of the collimated beam incident on a white card can be seen in Figure D.2.

From Figure D.2, it can be seen that a large residual of the infrared beam is present and mixed in with the UV generated second harmonic. The splitting of the two frequencies in a single beam requires either a prism, filters or dichoric mirrors to separate them. In this case, as the Ti:Sapphire laser is mode-locked, the pulses would be highly dispersed if a prism is used, thus either a filter tuned to reject or pass either the infrared or the UV beams or a hot/cold mirror is the prefered solution. A schematic of this design can be seen in Figure D.3.

D.4 Results

The conversion efficiency of SHG can not exceed 50% (Krylov *et al.* 1995), and at low intensities, the conversion efficiency is relatively low. However, as the intensity of the pump laser beam is increased at a fixed wavelength, the generated power of the second harmonic harmonic increases with a linear dependence. This can clearly be seen in Figure D.4, where the conversion efficiency of the BBO crystal increases with a linear dependence to the pump power fixed at a wavelength of 800 nm.

Phase matching is also important for SHG, as the thickness and orientation of a crystal used needs to be accurately tuned for a particular band of wavelengths

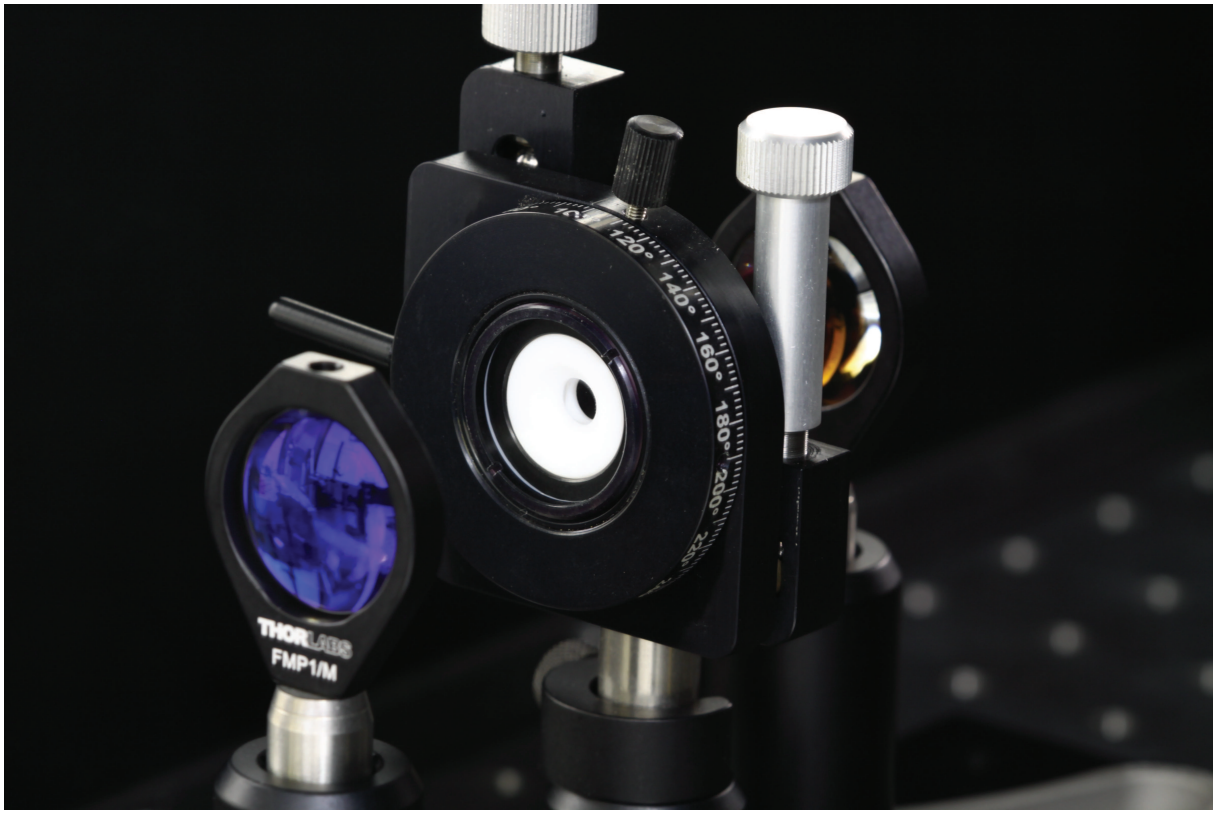

Figure D.1. An optical setup to perform second harmonic generation. Two lenses are used in front and behind the BBO crystal in the centre to focus and collimate the optical beam. The BBO crystal is mounted in the Teflon ring. Note the distinct difference in the colours of the anti-reflection coatings of the lenses. The blue tinged lens in the foreground is tuned for infrared wavelengths, while the orange tinged lens in the background is tuned for UV wavelengths.

(Glenn 1969, Nikogosyan and Gurzadyan 1987) for efficient SHG. As can be seen in Figure D.5, an infrared beam is focussed onto the BBO crystal, purchaed from EKSPLA, BBO-604H, 6 $\times$ 6 mm width by height, and a thickness of 1 mm, is phased matched for wavelengths approximately 780 to 830 nm. The infrared pump power is fixed at 500 mW, while the wavelength is varied from 740 to 870 nm in 5 nm increments and the power of generated second harmonic UV beam is measured. The peak generated power is centered around the 800 nm input wavelength as quoted by the manufacturer, while stretching beyond this wavelength shows sharp falls in conversion efficiency as expected, due to the phase mismatch.

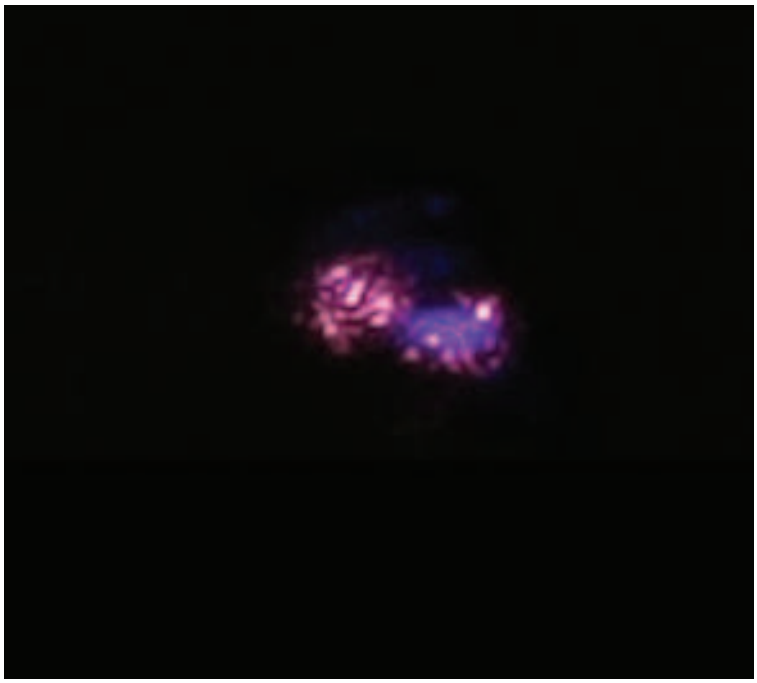

Figure D.2. Resultant output of second harmonic generation. The collimated optical output of SHG from the BBO crystal, where the red infrared residual beam is mixed with the blue ultraviolet beam. The mixing produces a violet tinge to the beam and can be separated using various optical components.

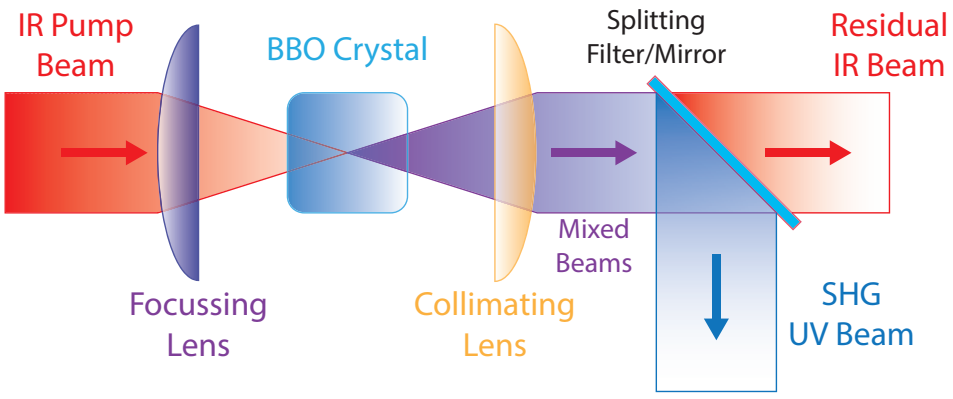

Figure D.3. Setup schematic of SHG with a BBO crystal. A filter or dichroic mirror is used to split the infrared and UV frequencies from a single beam. This allows for the residual and second harmonic to be used independantly or power of both beams measured to determine conversion efficiency.

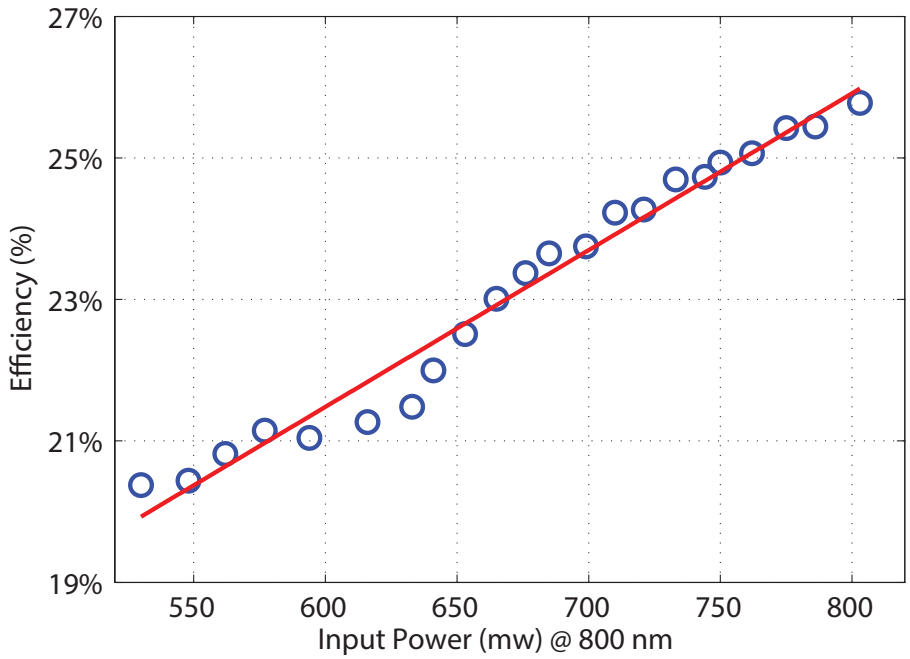

Figure D.4. Efficiency of SHG versus incident power. The same measurement setup from Figures D.3-D.5 is again used in this figure, where the wavelength is fixed at 800 nm, while the pump power is tuned from 530 to approximately 800 mW in 12 mW increments. It is clear from the data that there is a linear relationship between conversion efficiency and pump intensity (depicted by the red curve).

D.5 Appendix Summary

This Appendix has discussed an overview into SHG using a BBO crystal. The theory behind SHG is briefly discussed, while an optical setup to measure the generated second harmonic is presented. The discrete separation of the generated UV beam from the residual infrared beam is also shown using a filter or dichroic mirror. It is then possible to use this UV beam to match the higher bandgap of semiconductors such as GaN discussed in Chapter 2.

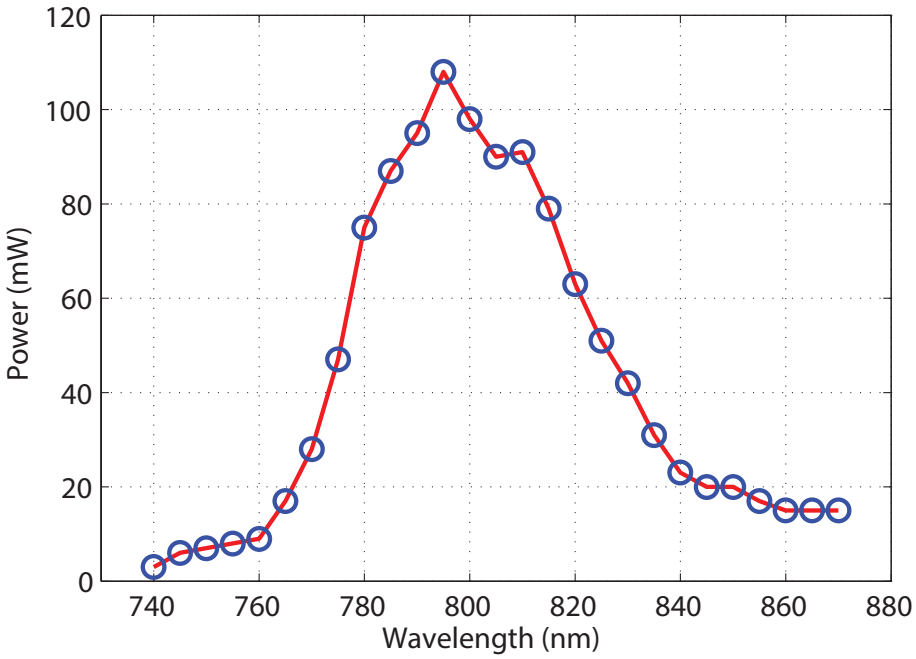

Figure D.5. Generated SHG power versus incident wavelength. The output of the Ti:Sapphire laser was fixed at 500 mW by carefully adjusting a ND (neutral density) filter, while the wavelength was swept from 740 to 870 nm in 5 nm increments. This beam is then used as the pump beam in the setup shown in Figure D.3, where the power of the generated UV beam is measured. As can clearly be seen, the crystal is optimised for wavelengths from approximately 780 to 830 nm.

Bibliography

ABBOTT-D., AND ZHANG-X.-C. (2007). Special issue on T-ray imaging, sensing, and retection, *Proc. IEEE*, **95**(8), pp. 1509–1513.

ADAM-A. J. L., PLANKEN-P. C. M., MELONI-S., AND DIK-J. (2009). Terahertz imaging of hidden paintlayers on canvas, *Opt. Express*, **17**(5), pp. 3407–3416.

ASHWORTH-P. C., PICKWELL-MACPHERSON-E., PROVENZANO-E., PINDER-S. E., PURUSHOTHAM-A. D., PEPPER-M., AND WALLACE-V. P. (2009). Terahertz pulsed spectroscopy of freshly excised human breast cancer, *Opt. Express*, **17**(15), pp. 12444–12454.

ATAKARAMIANS-S., AFSHAR-S. V., NAGEL-M., RASMUSSEN-H. K., BANG-O., MONRO-T. M., AND ABBOTT-D. (2011). Direct probing of evanescent field for characterization of porous terahertz fibers, *Appl. Phys. Lett.*, **98**(12), art. no. 121104.

AUSTON-D., AND NUSS-M. (1988). Electrooptical generation and detection of femtosecond electrical transients, *IEEE J. Quantum Electron.*, **24**(2), pp. 184–197.

AUSTON-D. H., LAVALLARD-P., SOL-N., AND KAPLAN-D. (1980). An amorphous silicon photodetector for picosecond pulses, *Appl. Phys. Lett.*, **36**(1), pp. 66–68.

AWAD-M., NAGEL-M., AND KURZ-H. (2007a). Enhanced photoconductive terahertz antenna array devices, *IRMMW-THz. Joint 32nd International Conference on Infrared and Millimeter Waves, 2007 and the 2007 15th International Conference on Terahertz Electronics.*, pp. 190–191.

AWAD-M., NAGEL-M., KURZ-H., HERFORT-J., AND PLOOG-K. (2007b). Characterization of low temperature GaAs antenna array terahertz emitters, *Appl. Phys. Lett.*, **91**(18), art. no. 181124.

BAKUNOV-M., MIKHAYLOVSKIY-R., TANI-M., AND QUE-C. (2010). A structure for enhanced terahertz emission from a photoexcited semiconductor surface, *Appl. Phys. B: Lasers Opt.*, **100**, pp. 695–698.

BANDYOPADHYAY-A., SENGUPTA-A., BARAT-R., GARY-D., FEDERICI-J., CHEN-M., AND TANNER-D. (2007). Effects of scattering on THz spectra of granular solids, *International Journal of Infrared and Millimeter Waves*, **28**(11), pp. 969–978.

BARTEL-T., GAAL-P., REIMANN-K., WOERNER-M., AND ELSAESSER-T. (2005). Generation of single-cycle THz transients with high electric-field amplitudes, *Opt. Lett.*, **30**(20), pp. 2805–2807.

BASS-M., FRANKEN-P. A., WARD-J. F., AND WEINREICH-G. (1962). Optical rectification, *Phys. Rev. Lett.*, **9**(11), pp. 446–448.

BASS, M.-M., AND ANDRINGA-K. (1967). Reproducible optical second-harmonic generation using a mode-locked laser, *IEEE J. Quantum Electron.*, **QE 3**(11), pp. 621–626.

BAUER-S. (1992). Optical properties of a metal film and its application as an infrared absorber and as a beam splitter, *American Journal of Physics*, **60**(3), pp. 257–261.

BELKIN-M. A., CAPASSO-F., XIE-F., BELYANIN-A., FISCHER-M., WITTMANN-A., AND FAIST-J. (2008). Room temperature terahertz quantum cascade laser source based on intracavity difference-frequency generation, *Appl. Phys. Lett.*, **92**(20), art. no. 201101.

BENZ-A., FASCHING-G., ANDREWS-A. M., MARTL-M., UNTERRAINER-K., ROCH-T., SCHRENK-W., GOLKA-S., AND STRASSER-G. (2007). Influence of doping on the performance of terahertz quantum-cascade lasers, *Appl. Phys. Lett.*, **90**(10), art. no. 101107.

BERRY-C., AND JARRAHI-M. (2012). Broadband terahertz polarizing beam splitter on a polymer substrate, *Journal of Infrared, Millimeter, and Terahertz Waves*, **33**(1), pp. 127–130.

BONVALET-A., JOFFRE-M., MARTIN-J. L., AND MIGUS-A. (1995). Generation of ultrabroadband femtosecond pulses in the mid-infrared by optical rectification of 15 fs light pulses at 100 MHz repetition rate, *Appl. Phys. Lett.*, **67**(20), pp. 2907–2909.

BORN-M., AND WOLF-E. (1997). *Principles of Optics*, 6 edn, Cambridge University Press.

BRALY-L. B., CRUZAN-J. D., LIU-K., FELLERS-R. S., AND SAYKALLY-R. J. (2000). Terahertz laser spectroscopy of the water dimer intermolecular vibrations. I. $(D_2O)_2$, *J. Chem. Phys.*, **112**(23), pp. 10293–10313.

BRUNNER-F. D. J., SCHNEIDER-A., AND GÜNTER-P. (2009). A terahertz time-domain spectrometerfor simultaneous transmission andreflection measurements at normalincidence, *Opt. Express*, **17**(23), pp. 20684–20693.

CARRIG-T. J., RODRIGUEZ-G., CLEMENT-T. S., TAYLOR-A. J., AND STEWART-K. R. (1995). Scaling of terahertz radiation via optical rectification in electro-optic crystals, *Appl. Phys. Lett.*, **66**(2), pp. 121–123.

CHEN-Q., AND ZHANG-X.-C. (1999). Polarization modulation in optoelectronic generation and detection of terahertz beams, *Appl. Phys. Lett.*, **74**(23), pp. 3435–3437.

CHIOU-C.-P., THOMPSON-R. B., WINFREE-W. P., MADARAS-E. I., AND SEEBO-J. (2007). Processing terahertz ray data in space shuttle inspection, *AIP Conf. Proc.*, **894**(1), pp. 425–431.

CLOUGH-B., LIU-J., AND ZHANG-X.-C. (2011). "All air–plasma" terahertz spectroscopy, *Opt. Lett.*, **36**(13), pp. 2399–2401.

COLE-B. E., WILLIAMS-J. B., KING-B. T., SHERWIN-M. S., AND STANLEY-C. R. (2001). Coherent manipulation of semiconductor quantum bits with terahertz radiation, *Nature*, **410**(6824), pp. 60–63.

COMLY-J., AND GARMIRE-E. (1968). Second harmonic generation from short pulses, *Appl. Phys. Lett.*, **12**(1), pp. 7–9.

COOK-D. J., AND HOCHSTRASSER-R. M. (2000). Intense terahertz pulses by four-wave rectification in air, *Opt. Lett.*, **25**(16), pp. 1210–1212.

COOKE-D. G., HEGMANN-F. A., YOUNG-E. C., AND TIEDJE-T. (2006). Electron mobility in dilute GaAs bismide and nitride alloys measured by time-resolved terahertz spectroscopy, *Appl. Phys. Lett.*, **89**(12), art. no. 122103.

COWARD-P. R., AND APPLEBY-R. (2003). Development of an illumination chamber for indoor millimeter-wave imaging, *Passive Millimeter-Wave Imaging Technology VI and Radar Sensor Technology VII*, pp. 54–61.

DAI-J., XIE-X., AND ZHANG-X.-C. (2007). Terahertz wave amplification in gases with the excitation of femtosecond laser pulses, *Appl. Phys. Lett.*, **91**(21), art. no. 2111102.

DAS-A., SCHUTZIUS-T. M., MEGARIDIS-C. M., SUBHECHHA-S., WANG-T., AND LIU-L. (2012). Quasi-optical terahertz polarizers enabled by inkjet printing of carbon nanocomposites, *Appl. Phys. Lett.*, **101**(24), art. no. 243108.

DENINGER-A. J., GOBEL-T., SCHONHERR-D., KINDER-T., ROGGENBUCK-A., KOBERLE-M., LISON-F., MULLER-WIRTS-T., AND MEISSNER-P. (2008). Precisely tunable continuous-wave terahertz source with interferometric frequency control, *Review of Scientific Instruments*, **79**(4), art. no. 044702.

DHILLON-S., ALTON-J., BARBIERI-S., SIRTORI-C., DE ROSSI-A., CALLIGARO-M., BEERE-H. E., AND RITCHIE-D. (2005). Ultralow threshold current terahertz quantum cascade lasers based on double-metal buried strip waveguides, *Appl. Phys. Lett.*, **87**(7), art. no. 071107.

EXTER-M. V., FATTINGER-C., AND GRISCHKOWSKY-D. (1989). Terahertz time-domain spectroscopy of water vapor, *Opt. Lett.*, **14**(20), pp. 1128–1130.

FAIST-J., CAPASSO-F., SIVCO-D. L., SIRTORI-C., HUTCHINSON-A. L., AND CHO-A. Y. (1994). Quantum cascade laser, *Science*, **264**(5158), pp. 553–556.

FAN-J. A., BELKIN-M. A., CAPASSO-F., KHANNA-S., LACHAB-M., DAVIES-A. G., AND LINFIELD-E. H. (2006). Surface emitting terahertz quantum cascade laser with a double-metal waveguide, *Opt. Express*, **14**(24), pp. 11672–11680.

FATTINGER-C., AND GRISCHKOWSKY-D. (1988). Point source terahertz optics, *Appl. Phys. Lett.*, **53**(16), pp. 1480–1482.

FAURE-J., VAN TILBORG-J., KAINDL-R. A., AND LEEMANS-W. P. (2004). Modelling laser-based table-top THz sources: Optical rectification, propagation and electro-optic sampling, *Opt. Quant. Electron.*, **36**(8), pp. 681–697.

FERGUSON-B., MICKAN-S. P., HUBBARD-S., PAVLIDIS-D., AND ABBOTT-D. (2001). Gallium nitride T-ray transmission characteristics, *Proceedings of SPIE, Electronics and Structures for MEMS II*, Vol. 4591, Adelaide, Australia, pp. 210–220.

FERGUSON-B. S., WANG-S., ZHONG-H., ABBOTT-D., AND ZHANG-X.-C. (2003). Powder retection with T-ray imaging, *Proceedings of SPIE, Terahertz for Military and Security Applications*, pp. 7–16.

FISCHER-B., HOFFMANN-M., HELM-H., MODJESCH-G., AND JEPSEN-P. U. (2005). Chemical recognition in terahertz time-domain spectroscopy and imaging, *Semicond. Sci. Technol.*, **20**(7), pp. S246–S253.

FISCHER-B. M. (2005). *Broadband THz Time-Domain Spectroscopy of Biomolecules: A Comprehensive Study of the Dielectric Properties of Biomolecules in the Far-Infrared*, PhD thesis, The University of Freiburg.

FISCHER-B. M., WALTHER-M., AND JEPSEN-P. U. (2002). Far-infrared vibrational modes of DNA components studied by terahertz time-domain spectroscopy, *Phys. Med. Biol.*, **47**(21), pp. 3807–3814.

FÜLÖP-J. A., PÁLFALVI-L., ALMÁSI-G., AND HEBLING-J. (2010). Design of high-energy terahertz sources based on optical rectification, *Opt. Express*, **18**(12), pp. 12311–12327.

FÜLÖP-J. A., PÁLFALVI-L., KLINGEBIEL-S., ALMÁSI-G., KRAUSZ-F., KARSCH-S., AND HEBLING-J. (2012). Generation of sub-mJ terahertz pulses by optical rectification, *Opt. Lett.*, **37**(4), pp. 557–559.

FRANKEN-P. A., HILL-A. E., PETERS-C. W., AND WEINREICH-G. (1961). Generation of optical harmonics, *Phys. Rev. Lett.*, **7**(4), pp. 118–119.

FRANZ-M., FISCHER-B. M., AND WALTHER-M. (2011). Probing structure and phase-transitions in molecular crystals by terahertz time-domain spectroscopy, *J. Mol. Struct.*, **1006**(1–3), pp. 34–40.

GLENN-W. H. (1969). Second-harmonic generation by picosecond optical pulses, *IEEE J. Quantum Electron.*, **QE 5**(6), pp. 284–290.

GOLAY-M. J. E. (1947). Theoretical consideration in heat and infra-red detection, with particular reference to the pneumatic detector, *Rev. Sci. Instrum.*, **18**(5), pp. 347–356.

GORSHUNOV-B., VOLKOV-A., SPEKTOR-I., PROKHOROV-A., MUKHIN-A., DRESSEL-M., UCHIDA-S., AND LOIDL-A. (2005). Terahertz BWO-spectrosopy, *Journal of Infrared, Millimeter, and Terahertz Waves*, **26**(9), pp. 1217–1240.

GOUSEV-Y. P., ALTUKHOV-I. V., KOROLEV-K. A., SINIS-V. P., KAGAN-M. S., HALLER-E. E., ODNOBLYUDOV-M. A., YASSIEVICH-I. N., AND CHAO-K.-A. (1999). Widely tunable continuous-wave THz laser, *Appl. Phys. Lett.*, **75**(6), pp. 757–759.

GREGORY-I., BAKER-C., TRIBE-W., BRADLEY-I., EVANS-M., LINFIELD-E., DAVIES-A., AND MISSOUS-M. (2005). Optimization of photomixers and antennas for continuous-wave terahertz emission, *IEEE J. Quantum Electron.*, **41**(5), pp. 717–728.

GRISCHKOWSKY-D., KEIDING-S., EXTER-M. V., AND FATTINGER-C. (1990). Far-infrared time-domain spectroscopy with terahertz beams of dielectrics and semiconductors, *J. Opt. Soc. Am. B*, **7**(10), pp. 2006–2015.

GROENENDAAL-L., JONAS-F., FREITAG-D., PIELARTZIK-H., AND REYNOLDS-J. R. (2000). Poly(3,4-ethylenedioxythiophene) and its derivatives: Past, present, and future, *Adv. Mater.*, **12**(7), pp. 481–494.

HADJILOUCAS-S., KARATZAS-L., AND BOWEN-J. (1999). Measurements of leaf water content using terahertz radiation, *IEEE Trans. Microw. Theory Tech.*, **47**(2), pp. 142–149.

HANGYO-M., NAGASHIMA-T., AND NASHIMA-S. (2002). Spectroscopy by pulsed terahertz radiation, *Meas. Sci. Technol.*, **13**(11), pp. 1727–1738.

HAN-P. Y., CHO-G. C., AND ZHANG-X.-C. (2000). Time-domain transillumination of biological tissues with terahertz pulses, *Opt. Lett.*, **25**(4), pp. 242–244.

HARDE-H., CHEVILLE-R. A., AND GRISCHKOWSKY-D. (1997). Terahertz studies of collision-broadened rotational lines, *J. Phys. Chem. A*, **101**(20), pp. 3646–3660.

HARSHA-S. S., LAMAN-N., AND GRISCHKOWSKY-D. R. (2008). High resolution waveguide THz-TDS of melamine, *Proc. Quantum Electronics and Laser Science Conference*, Optical Society of America, San Jose, California USA, p. JWA40.

HEALD-M., AND MARION-J. (1994). *Classical Electromagnetic Radiation*, 3 edn, Brooks Cole.

HEAVENS-O. S. (1955). *Optical Properties of Thin Solid Films*, Butterworth's Scientific Publications.

HEGMANN-F. A., OSTROVERKHOVA-O., AND COOKE-D. G. (2006). *Probing Organic Semiconductors with Terahertz Pulses*, Wiley-VCH Verlag GmbH & Co. KGaA, pp. 367–428.

HOFFMANN-M. C., AND FÜLÖP-J. A. (2011). Intense ultrashort terahertz pulses: generation and applications, *J. Phys. D: Appl. Phys.*, **44**(8), art. no. 083001.

HOMES-C. C., CARR-G. L., LOBO-R. P. S. M., LAVEIGNE-J. D., AND TANNER-D. B. (2007). Silicon beam splitter for far-infrared and terahertz spectroscopy, *Appl. Opt.*, **46**(32), pp. 7884–7888.

HUBER-R., BRODSCHELM-A., TAUSER-F., AND LEITENSTORFER-A. (2000). Generation and field-resolved detection of femtosecond electromagnetic pulses tunable up to 41 THz, *Appl. Phys. Lett.*, **76**(22), pp. 3191–3193.

INZELT-G. (2008). *Conducting Polymers: A New Era in Electrochemistry*, Springer.

ISHIDA-Y., AND YAJIMA-T. (1987). Characteristics of a new-type SHG crystala β-BaB_2O_4 in the femtosecond region, *Opt. Commun.*, **62**(3), pp. 197– 200.

JACOBSEN-R. H., MITTLEMAN-D. M., AND NUSS-M. C. (1996). Chemical recognition of gases and gas mixtures with terahertz waves, *Opt. Lett.*, **21**(24), pp. 2011–2013.

JANG-E. S., JUNG-M. Y., AND MIN-D. B. (2005). Hydrogenation for low trans and high conjugated fatty acids, *Compr. Rev. Food Sci. Food Saf.*, **4**(1), pp. 22–30.

JEON-T.-I., AND GRISCHKOWSKY-D. (1998). Characterization of optically dense, doped semiconductors by reflection THz time domain spectroscopy, *Appl. Phys. Lett.*, **72**(23), pp. 3032–3034.

JEPSEN-P., COOKE-D., AND KOCH-M. (2011). Terahertz spectroscopy and imaging—modern techniques and applications, *Laser Photon. Rev.*, **5**(1), pp. 124–166.

JEPSEN-P. U., AND FISCHER-B. M. (2005). Dynamic range in terahertz time-domain transmission and reflectionspectroscopy, *Opt. Lett.*, **30**(1), pp. 29–31.

JEPSEN-P. U., JACOBSEN-R. H., AND KEIDING-S. R. (1996). Generation and detection of terahertz pulses from biased semiconductor antennas, *J. Opt. Soc. Am. B*, **13**(11), pp. 2424–2436.

JEPSEN-P. U., MØLLER-U., AND MERBOLD-H. (2007). Investigation of aqueous alcohol and sugar solutions with reflection terahertz time-domain spectroscopy, *Opt. Express*, **15**(22), pp. 14717–14737.

JIN-Y.-S., KIM-G.-J., AND JEON-S.-G. (2006). Terahertz dielectric properties of polymers, *J. Korean Phys. Soc.*, **49**(2), pp. 513–517.

KAWASE-K., ICHINO-S., SUIZU-K., AND SHIBUYA-T. (2011). Half cycle terahertz pulse generation by prism-coupled cherenkov phase-matching method, *Journal of Infrared, Millimeter, and Terahertz Waves*, **32**, pp. 1168–1177.

KAWASE-K., OGAWA-Y., WATANABE-Y., AND INOUE-H. (2003). Non-destructive terahertz imaging of illicit drugs using spectral fingerprints, *Opt. Express*, **11**(20), pp. 2549–2554.

KAZARINOV-R. F., AND SURIS-R. A. (1971). Possibility of amplification of electromagnetic waves in a semiconductor with a superlattice, *Sov. Phys. Semicon.*, **5**, pp. 707–709.

KOHLER-R., TREDICUCCI-A., BELTRAM-F., BEERE-H. E., LINFIELD-E. H., DAVIES-A. G., RITCHIE-D. A., IOTTI-R. C., AND ROSSI-F. (2002). Terahertz semiconductor-heterostructure laser, *Nature*, **417**(6885), pp. 156–159.

KRESS-M., LÖFFLER-T., EDEN-S., THOMSON-M., AND ROSKOS-H. G. (2004). Terahertz-pulse generation by photoionization of airwith laser pulses composed of both fundamental and second-harmonicwaves, *Opt. Lett.*, **29**(10), pp. 1120–1122.

KRYLOV-V., REBANE-A., KALINTSEV-A. G., SCHWOERER-H., AND WILD-U. P. (1995). 2nd-harmonic generation of amplified femtosecond Ti sapphire laser-pulses, *Opt. Lett.*, **20**(2), pp. 198–200.

LAMAN-N., AND GRISCHKOWSKY-D. (2008). Terahertz conductivity of thin metal films, *Appl. Phys. Lett.*, **93**(5), art. no. 051105.

LEE-A. W. M., QIN-Q., KUMAR-S., WILLIAMS-B. S., HU-Q., AND RENO-J. L. (2006). Real-time terahertz imaging over a standoff distance (> 25 meters), *Appl. Phys. Lett.*, **89**(14), art. no. 141125.

LÖFFLER-T., KRESS-M., THOMSON-M., HAHN-T., HASEGAWA-N., AND ROSKOS-H. G. (2005). Comparative performance of terahertz emitters in amplifier-laser-based systems, *Semicond. Sci. Technol.*, **20**(7), pp. S134–S141.

LICHTENSTEIN-A. H., AUSMAN-L. M., JALBERT-S. M., AND SCHAEFER-E. J. (1999). Effects of different forms of dietary hydrogenated fats on serum lipoprotein cholesterol levels, *N. Engl. J. Med.*, **340**(25), pp. 1933–1940.

LI-J. (2010). Optical parameters of vegetable oil studied by terahertz time-domain spectroscopy, *Appl. Spectrosc.*, **64**(2), pp. 231–234.

LI-J., LI-J., AND YAO-J. (2008). Terahertz time-domain spectroscopy and application on peanut oils, *Proc. SPIE, Photonics and Optoelectronics Meetings (POEM) 2008: Terahertz Science and Technology*, Vol. 7277, Wuhan, China.

LIU-H.-B., CHEN-Y., BASTIAANS-G. J., AND ZHANG-X.-C. (2006). Detection and identification of explosive RDX by THz diffuse reflection spectroscopy, *Opt. Express*, **14**(1), pp. 415–423.

LIU-H.-B., PLOPPER-G., EARLEY-S., CHEN-Y., FERGUSON-B., AND ZHANG-X.-C. (2007a). Sensing minute changes in biological cell monolayers with THz differential time-domain spectroscopy., *Biosens. Bioelectron.*, **22**(6), pp. 1075–1080.

LIU-H.-B., ZHONG-H., KARPOWICZ-N., CHEN-Y., AND ZHANG-X.-C. (2007b). Terahertz spectroscopy and imaging for defense and security applications, *Proc. IEEE*, **95**(8), pp. 1514–1527.

LIU-H. C., WACHTER-M., BAN-D., WASILEWSKI-Z. R., BUCHANAN-M., AERS-G. C., CAO-J. C., FENG-S. L., WILLIAMS-B. S., AND HU-Q. (2005). Effect of doping concentration on the performance of terahertz quantum-cascade lasers, *Appl. Phys. Lett.*, **87**(14), art. no. 141102.

LO-Y. H., AND LEONHARDT-R. (2008). Aspheric lenses for terahertz imaging, *Opt. Express*, **16**(20), pp. 15991–15998.

LU-J.-Y., CHEN-L.-J., KAO-T.-F., CHANG-H.-H., CHEN-H.-W., LIU-A.-S., CHEN-Y.-C., WU-R.-B., LIU-W.-S., CHYI-J.-I., AND SUN-C.-K. (2006). Terahertz microchip for illicit drug detection, *IEEE Photon. Technol. Lett.*, **18**(21), pp. 2254–2256.

LU-Q. Y., BANDYOPADHYAY-N., SLIVKEN-S., BAI-Y., AND RAZEGHI-M. (2012). Widely tuned room temperature terahertz quantum cascade laser sources based on difference-frequency generation, *Appl. Phys. Lett.*, **101**(25), art. no. 251121.

MACLEOD-C. (2007). China admits tainted food link, *Technical report*, USA Today.

MAIER-S. A. (2007). *Plasmonics: Fundamentals and Applications*, Vol. 1, Springer, p. 248.

MAIR-S., GOMPF-B., AND DRESSEL-M. (2004). Spatial and spectral behavior of the optical near field studied by a terahertz near-field spectrometer, *Appl. Phys. Lett.*, **84**(7), pp. 1219–1221.

MALIK-A. K., MALIK-H. K., AND KAWATA-S. (2010). Investigations on terahertz radiation generated by two superposed femtosecond laser pulses, *J. Appl. Phys.*, **107**(11), art. no. 113105.

MARKELZ-A. (2008). Terahertz dielectric sensitivity to biomolecular structure and function, *IEEE J. Quantum Electron.*, **14**(1), pp. 180–190.

MAUER-L. J., CHERNYSHOVA-A. A., HIATT-A., DEERING-A., AND DAVIS-R. (2009). Melamine detection in infant formula powder using near- and mid-infrared spectroscopy, *J. Agric. Food Chem.*, **57**(10), pp. 3974–3980.

MAY-R. K., EVANS-M. J., ZHONG-S., WARR-I., GLADDEN-L. F., SHEN-Y., AND ZEITLER-J. A. (2011). Terahertz in-line sensor for direct coating thickness measurement of individual tablets during film coating in real-time, *J. Pharm. Sci.*, **100**(4), pp. 1535–1544.

MENDIS-R., AND MITTLEMAN-D. M. (2009). Comparison of the lowest-order transverse-electric (TE1) and transverse-magnetic (TEM) modes of the parallel-plate waveguide for terahertz pulse applications, *Opt. Express*, **17**(17), pp. 14839–14850.

MITTLEMAN-D. (2010). *Sensing With Terahertz Radiation*, Springer.

MITTLEMAN-D., JACOBSEN-R., NEELAMANI-R., BARANIUK-R., AND NUSS-M. (1998). Gas sensing using terahertz time-domain spectroscopy, *Appl. Phys. B*, **67**(3), pp. 379–390.

MOHR-P. J., TAYLOR-B. N., AND NEWELL-D. B. (2012). Codata recommended values of the fundamental physical constants: 2010, *Rev. Mod. Phys.*, **84**(4), pp. 1527–1605.

MOULTON-P. F. (1986). Spectroscopic and laser characteristics of Ti:Al_2O_3, *J. Opt. Soc. Am. B*, **3**(1), pp. 125–133.

MOUROU-G., STANCAMPIANO-C. V., ANTONETTI-A., AND ORSZAG-A. (1981). Picosecond microwave pulses generated with a subpicosecond laser-driven semiconductor switch, *Appl. Phys. Lett.*, **39**(4), pp. 295–296.

NAFTALY-M., AND MILES-R. (2007). Terahertz time-domain spectroscopy for material characterization, *Proc. IEEE*, **95**(8), pp. 1658–1665.

NAGAI-M., MATSUBARA-E., AND ASHIDA-M. (2012). High-efficiency terahertz pulse generation via optical rectification by suppressing stimulated raman scattering process, *Opt. Express*, **20**(6), pp. 6509–6514.

NASHIMA-S., MORIKAWA-O., TAKATA-K., AND HANGYO-M. (2001a). Measurement of optical properties of highly doped silicon by terahertz time domain reflection spectroscopy, *Appl. Phys. Lett.*, **79**(24), pp. 3923–3925.

NASHIMA-S., MORIKAWA-O., TAKATA-K., AND HANGYO-M. (2001b). Temperature dependence of optical and electronic properties of moderately doped silicon at terahertz frequencies, *J. Appl. Phys.*, **90**(2), pp. 837–842.

NIELSEN-K., RASMUSSEN-H. K., ADAM-A. J., PLANKEN-P. C., BANG-O., AND JEPSEN-P. U. (2009). Bendable, low-loss topas fibers for the terahertz frequency range, *Opt. Express*, **17**(10), pp. 8592–8601.

NIKOGOSYAN-D. N. (1991). Beta Barium Borate (BBO) - A review of its properties and applications, *Appl. Phys. A: Mater. Sci. Process.*, **52**(6), pp. 359–368.

NIKOGOSYAN-D. N., AND GURZADYAN-G. G. (1987). Crystals for nonlinear optics, *Soviet Journal of Quantum Electronics*, **17**(8), pp. 970–977.

PARK-S.-G., MELLOCH-M. R., AND WEINER-A. M. (1998). Comparison of terahertz waveforms measured by electro-optic and photoconductive sampling, *Appl. Phys. Lett.*, **73**(22), pp. 3184–3186.

PARROTT-E. P. J., SUN-Y., AND PICKWELL-MACPHERSON-E. (2011). Terahertz spectroscopy: Its future role in medical diagnoses, *J. Mol. Struct.*, **1006**(1), pp. 66–76.

PHILIPP-M., GRAF-U., WAGNER-GENTNER-A., RABANUS-D., AND LEWEN-F. (2007). Compact 1.9 THz BWO local-oscillator for the GREAT heterodyne receiver, *Infrared Phys. Techn.*, **51**(1), pp. 54–59.

PICKWELL-E., AND WALLACE-V. P. (2006). Biomedical applications of terahertz technology, *J. Phys. D: Appl. Phys.*, **39**(17), pp. R301–R301.

PICKWELL-E., COLE-B. E., FITZGERALD-A. J., PEPPER-M., AND WALLACE-V. P. (2004). In vivo study of human skin using pulsed terahertz radiation, *Phys. Med. Biol.*, **49**(9), pp. 1595–1607.

PIESIEWICZ-R., JANSEN-C., WIETZKE-S., MITTLEMAN-D., KOCH-M., AND KRNER-T. (2007). Properties of building and plastic materials in the THz range, *Journal of Infrared, Millimeter, and Terahertz Waves*, **28**(5), pp. 363–371.

PNG-G., FLOOK-R., NG-B. W.-H., AND ABBOTT-D. (2009). Terahertz spectroscopy of snap-frozen human brain tissue: an initial study, *Electronics Letters*, **45**(7), pp. 343–345.

PUPEZA-I., WILK-R., AND KOCH-M. (2007). Highly accurate optical material parameter determination with THz time-domain spectroscopy, *Opt. Express*, **15**(7), pp. 4335–4350.

REIMANN-K. (2007). Table-top sources of ultrashort THz pulses, *Rep. Prog. Phys.*, **70**(10), pp. 1597–1632. Quote: "To summarize, one does not know exactly how the THz generation using this method works, but it works." pp. 1615 (on Four-wave-mixing in a plasma).

RICE-A., JIN-Y., MA-X. F., ZHANG-X.-C., BLISS-D., LARKIN-J., AND ALEXANDER-M. (1994). Terahertz optical rectification from <110> zinc-blende crystals, *Appl. Phys. Lett.*, **64**(11), pp. 1324–1326.

RICHARDS-P. L. (1994). Bolometers for infrared and millimeter waves, *J. Appl. Phys.*, **76**(1), pp. 1–24.

ROCHAT-M., AJILI-L., WILLENBERG-H., FAIST-J., BEERE-H., DAVIES-G., LINFIELD-E., AND RITCHIE-D. (2002). Low-threshold terahertz quantum-cascade lasers, *Appl. Phys. Lett.*, **81**(8), pp. 1381–1383.

RØNNE-C., THRANE-L., ASTRAND-P.-O., WALLQVIST-A., MIKKELSEN-K. V., AND KEIDING-S. R. (1997). Investigation of the temperature dependence of dielectric relaxation in liquid water by THz reflection spectroscopy and molecular dynamics simulation, *J. Chem. Phys.*, **107**(14), pp. 5319–5331.

RUSSE-I.-S., BROCK-D., KNOP-K., KLEINEBUDDE-P., AND ZEITLER-J. A. (2012). Validation of terahertz coating thickness measurements using X-ray microtomography, *Mol. Pharmaceutics*, **9**(12), pp. 3551–3559.

SAKAI-K. (2005). *Terahertz Optoelectronics*, Springer.

SARTORIUS-B., STANZE-D., GÖBEL-T., SCHMIDT-D., AND SCHELL-M. (2012). Continuous wave terahertz systems based on 1.5 μm telecom technologies, *Journal of Infrared, Millimeter, and Terahertz Waves*, **33**(4), pp. 405–417.

SCALARI-G., WALTHER-C., FAIST-J., BEERE-H., AND RITCHIE-D. (2006). Electrically switchable, two-color quantum cascade laser emitting at 1.39 and 2.3 THz, *Appl. Phys. Lett.*, **88**(14), art. no. 141102.

SCHERGER-B., JÖRDENS-C., AND KOCH-M. (2011a). Variable-focus terahertz lens, *Opt. Express*, **19**(5), pp. 4528–4535.

SCHERGER-B., SCHELLER-M., JANSEN-C., KOCH-M., AND WIESAUER-K. (2011b). Terahertz lenses made by compression molding of micropowders, *Appl. Opt.*, **50**(15), pp. 2256–2262.

SCHERGER-B., SCHELLER-M., VIEWEG-N., CUNDIFF-S. T., AND KOCH-M. (2011c). Paper terahertz wave plates, *Opt. Express*, **19**(25), pp. 24884–24889.

SCHMUTTENMAER-C. A. (2004). Exploring dynamics in the far-infrared with terahertz spectroscopy, *Chem. Rev.*, **104**(4), pp. 1759–1780.

SELVAGANESH-S., MATHIYARASU-J., PHANI-K., AND YEGNARAMAN-V. (2007). Chemical synthesis of pedot-au nanocomposite, *Nanoscale Res. Lett.*, **2**(11), pp. 546–549.

SHAPIRO-S. L. (1968). Second harmonic generation in $LiNbO_3$ by picosecond pulses, *Appl. Phys. Lett.*, **13**(1), pp. 19–21.

SHEN-Y. (2003). *The Principles of Nonlinear Optics*, Wiley-Interscience.

SHEN-Y. C., UPADHYA-P. C., LINFIELD-E. H., BEERE-H. E., AND DAVIES-A. G. (2003). Ultrabroadband terahertz radiation from low-temperature-grown GaAs photoconductive emitters, *Appl. Phys. Lett.*, **83**(15), pp. 3117–3119.

SHIRAKAWA-H., LOUIS-E. J., MACDIARMID-A. G., CHIANG-C. K., AND HEEGER-A. J. (1977). Synthesis of electrically conducting organic polymers: halogen derivatives of polyacetylene, (CH), *J. Chem. Soc., Chem. Commun.*, (16), pp. 578–580.

SIEMION-A., SIEMION-A., MAKOWSKI-M., SYPEK-M., HÉRAULT-E., GARET-F., AND COUTAZ-J.-L. (2011). Off-axis metallic diffractive lens for terahertz beams, *Opt. Lett.*, **36**(11), pp. 1960–1962.

SMELA-E. (2003). Conjugated polymer actuators for biomedical applications, *Adv. Mater.*, **15**(6), pp. 481–494.

Standards Australia Committee ME/71, Quantities, Units and Conversion (1998).

STARR-A. F., RYE-P. M., SMITH-D. R., AND NEMAT-NASSER-S. (2004). Fabrication and characterization of a negative-refractive-index composite metamaterial, *Phys. Rev. B*, **70**(11), art. no. 113102.

STRACHAN-C. J., RADES-T., NEWNHAM-D. A., GORDON-K. C., PEPPER-M., AND TADAY-P. F. (2004). Using terahertz pulsed spectroscopy to study crystallinity of pharmaceutical materials, *Chem. Phys. Lett.*, **390**(1–3), pp. 20–24.

STRACHAN-C. J., TADAY-P. F., NEWNHAM-D. A., GORDON-K. C., ZEITLER-J. A., PEPPER-M., AND RADES-T. (2005). Using terahertz pulsed spectroscopy to quantify pharmaceutical polymorphism and crystallinity, *J. Pharm. Sci.*, **94**(4), pp. 837–846.

SUN-F. G., WAGONER-G. A., AND ZHANG-X.-C. (1995). Measurement of free-space terahertz pulses via long-lifetime photoconductors, *Appl. Phys. Lett.*, **67**(12), pp. 1656–1658.

TADAY-P. F. (2004). Applications of terahertz spectroscopy to pharmaceutical sciences, *Philos. Trans. R. Soc. London, A*, **362**(1815), pp. 351–364.

TAMOSIUNAS-V., ZOBL-R., ULRICH-J., UNTERRAINER-K., COLOMBELLI-R., GMACHL-C., WEST-K., PFEIFFER-L., AND CAPASSO-F. (2003). Terahertz quantum cascade lasers in a magnetic field, *Appl. Phys. Lett.*, **83**(19), pp. 3873–3875.

TANI-M., HORITA-K., KINOSHITA-T., QUE-C. T., ESTACIO-E., YAMAMOTO-K., AND BAKUNOV-M. I. (2011). Efficient electro-optic sampling detection of terahertz radiation via Cherenkov phase matching, *Opt. Express*, **19**(21), pp. 19901–19906.

TANI-M., YAMAMOTO-K., ESTACIO-E., QUE-C., NAKAJIMA-H., HIBI-M., MIYAMARU-F., NISHIZAWA-S., AND HANGYO-M. (2012). Photoconductive emission and detection of terahertz pulsed radiation using semiconductors and semiconductor devices, *Journal of Infrared, Millimeter, and Terahertz Waves*, **33**(4), pp. 393–404.

TE-C. C., FERGUSON-B., AND ABBOTT-D. (2002). Investigation of biomaterial classification using T-rays, *Proc. SPIE, Biomedical Applications of Micro- and Nanoengineering.*, Vol. 4937, pp. 294–306.

THEUER-M., BEIGANG-R., AND GRISCHKOWSKY-D. (2010). Highly sensitive terahertz measurement of layer thickness using a two-cylinder waveguide sensor, *Appl. Phys. Lett.*, **97**(7), art. no. 071106.

TINKHAM-M. (1956). Energy gap interpretation of experiments on infrared transmission through superconducting films, *Phys. Rev.*, **104**(3), pp. 845–846.

TONOUCHI-M. (2007). Cutting-edge terahertz technology, *Nat. Photon.*, **1**(2), pp. 97–105.

TURNIPSEED-S., CASEY-C., NOCHETTO-C., AND HELLER-D. N. (2008). Determination of melamine and cyanuric acid residues in infant formula using LC-MS/MS, *US FDA Laboratory Information Bulletin*, **24**(4421).

UNG-B., MAZHOROVA-A., DUPUIS-A., ROZÉ-M., AND SKOROBOGATIY-M. (2011). Polymer microstructured optical fibers for terahertz wave guiding, *Opt. Express*, **19**(26), pp. B848–B861.

UNG-B. S.-Y., BALAKRISHNAN-J., FISCHER-B. M., NG-B. W.-H., AND ABBOTT-D. (2006). Substance detection for security screening using terahertz imaging technology, *Joint 31st International Conference on Infrared Millimeter Waves and 14th International Conference on Teraherz Electronics, 2006. IRMMW-THz 2006.*, Shanghai, China, pp. 447–447.

UNG-B. S.-Y., FISCHER-B. M., NG-B.-W., AND ABBOTT-D. (2009). Comparative investigation of detection of melamine in food powders, *IRMMW-THz 2009. 34th International Conference on Infrared, Millimeter, and Terahertz Waves, 2009*, Busan, Korea.

UNG-B. S.-Y., FUMEAUX-C., LIN-H., FISCHER-B. M., NG-B. W.-H., AND ABBOTT-D. (2012). Low-cost ultra-thin broadband terahertz beam-splitter, *Opt. Express*, **20**(5), pp. 4968–4978.

UNG-B. S.-Y., LI-J., LIN-H., FISCHER-B. M., WITHAYACHUMNANKUL-W., AND ABBOTT-D. (2013a). Dual-mode terahertz time-domain spectroscopy system, *IEEE Transactions on Terahertz Science and Technology*, **3**(2), pp. 216–220.

UNG-B. S.-Y., NG-B. W.-H., AND ABBOTT-D. (2008). Simultaneous dual scanning terahertz system, *33rd International Conference on Infrared, Millimeter and Terahertz Waves, 2008. IRMMW-THz 2008*, Pasadena, USA.

UNG-B. S.-Y., NG-B. W.-H., AND ABBOTT-D. (2010). A preliminary study of hydrogenation of oils using terahertz time domain spectroscopy, *35th International Conference on Infrared Millimeter and Terahertz Waves (IRMMW-THz), 2010*, Rome, Italy.

UNG-B. S.-Y., WENG, B. ABD SHEPERD-R., ABBOTT-D., AND FUMEAUX-C. (2013b). Inkjet printed conductive polymer-based beam-splitters for terahertz applications, *Opt. Mat. Express*, **3**(9), pp. 1242–1249.

VAN EXTER-M., AND GRISCHKOWSKY-D. (1990a). Carrier dynamics of electrons and holes in moderately doped silicon, *Phys. Rev. B*, **41**(17), pp. 12140–12149.

VAN EXTER-M., AND GRISCHKOWSKY-D. (1990b). Characterization of an optoelectronic terahertz beam system, *IEEE Trans. Microw. Theory Techn.*, **38**(11), pp. 1684–1691.

VAN RUDD-J., AND MITTLEMAN-D. M. (2002). Influence of substrate-lens design in terahertz time-domain spectroscopy, *J. Opt. Soc. Am. B*, **19**(2), pp. 319–329.

VERNITSKAYA-T. V., AND EFIMOV-O. N. (1997). Polypyrrole: a conducting polymer; its synthesis, properties and applications, *Russ. Chem. Rev.*, **66**(5), pp. 443–457.

VITIELLO-M. S., SCAMARCIO-G., SPAGNOLO-V., DHILLON-S. S., AND SIRTORI-C. (2007). Terahertz quantum cascade lasers with large wall-plug efficiency, *Appl. Phys. Lett.*, **90**(19), pp. 191115–3.

VOISIAT-B., BIČIŪNAS-A., KAŠALYNAS-I., AND RAČIUKAITIS-G. (2011). Band-pass filters for THz spectral range fabricated by laser ablation, *Appl. Phys. A: Mater. Sci. Process.*, **104**, pp. 953–958.

WALKER-S. B., AND LEWIS-J. A. (2012). Reactive silver inks for patterning high-conductivity features at mild temperatures, *J. Am. Chem. Soc.*, **134**(3), pp. 1419–1421.

WALLACE-V. P., FITZGERALD-A. J., PICKWELL-E., PYE-R. J., TADAY-P. F., FLANAGAN-N., AND HA-T. (2006). Terahertz pulsed spectroscopy of human basal cell carcinoma, *Appl. Spectrosc.*, **60**(10), pp. 1127–1133.

WALTHER-C., SCALARI-G., FAIST-J., BEERE-H., AND RITCHIE-D. (2006). Low frequency terahertz quantum cascade laser operating from 1.6 to 1.8 THz, *Appl. Phys. Lett.*, **89**(23), art. no. 231121.

WALTHER-M. (2003). *Modern Spectroscopy on Biological Molecules Structure and Bonding Investigated by THz Time-Domain and Transient Phase-Grating Spectroscopy*, PhD thesis, The University of Freiburg.

WALTHER-M., COOKE-D. G., SHERSTAN-C., HAJAR-M., FREEMAN-M. R., AND HEGMANN-F. A. (2007). Terahertz conductivity of thin gold films at the metal-insulator percolation transition, *Phys. Rev. B*, **76**(12), art. no. 125408.

WALTHER-M., FISCHER-B. M., AND UHD JEPSEN-P. (2003). Noncovalent intermolecular forces in polycrystalline and amorphous saccharides in the far infrared, *Chem. Phys.*, **288**(2–3), pp. 261–268.

WANG-J. (2008). Dairy giant's share price plummets 60 per cent, *Technical Report A5*.

WANG-S., FERGUSON-B., MANNELLA-C., ABBOTT-D., AND ZHANG-X. C. (2002). Powder detection using THz imaging, *Quantum Electronics and Laser Science Conference, 2002. QELS '02. Technical Digest*, pp. 44–45.

WANG-T.-J., MARCEAU-C., CHEN-Y., YUAN-S., THEBERGE-F., CHATEAUNEUF-M., DUBOIS-J., AND CHIN-S. L. (2010). Terahertz emission from a DC-biased two-color femtosecond laser-induced filament in air, *Appl. Phys. Lett.*, **96**(21), art. no. 211113.

WARD-J. F. (1966). Absolute measurement of an optical-rectification coefficient in ammonium dihydrogen phosphate, *Phys. Rev.*, **143**(2), pp. 569–574.

WATANABE-Y., KAWASE-K., IKARI-T., ITO-H., ISHIKAWA-Y., AND MINAMIDE-H. (2003). Component spatial pattern analysis of chemicals using terahertz spectroscopic imaging, *Appl. Phys. Lett.*, **83**(4), pp. 800–802.

WEBSTER-J. G. (1999). *The Measurement, Instrumentation, and Sensors Handbook*, CRC Press.

WEINER-A. M., KAN'AN-A. M., AND LEAIRD-D. E. (1998). High-efficiency blue generation by frequency doubling of femtosecond pulses in a thick nonlinear crystal, *Opt. Lett.*, **23**(18), pp. 1441–1443.

WENG-B., SHEPHERD-R., CHEN-J., AND WALLACE-G. G. (2011). Gemini surfactant doped polypyrrole nanodispersions: an inkjet printable formulation, *J. Mater. Chem.*, **21**(6), pp. 1918–1924.

WILLIAMS-B., KUMAR-S., HU-Q., AND RENO-J. (2005). Operation of terahertz quantum-cascade lasers at 164 K in pulsed mode and at 117 K in continuous-wave mode, *Opt. Express*, **13**(9), pp. 3331–3339.

WILLIAMS-B., KUMAR-S., HU-Q., AND RENO-J. (2006). High-power terahertz quantum-cascade lasers, *Electron. Lett.*, **42**(2), pp. 89–91.

WILLIAMS-B. S. (2007). Terahertz quantum-cascade lasers, *Nature Photonics*, **1**(9), pp. 517–525.

WILLIAMS-B. S., CALLEBAUT-H., KUMAR-S., HU-Q., AND RENO-J. L. (2003). 3.4-THz quantum cascade laser based on longitudinal-optical-phonon scattering for depopulation, *Appl. Phys. Lett.*, **82**(7), pp. 1015–1017.

WITHAYACHUMNANKUL-W., FISCHER-B. M., LIN-H., AND ABBOTT-D. (2008). Uncertainty in terahertz time-domain spectroscopy measurement, *J. Opt. Soc. Am. B*, **25**(6), pp. 1059–1072.

WOODWARD-R. M., COLE-B. E., WALLACE-V. P., PYE-R. J., ARNONE-D. D., LINFIELD-E. H., AND PEPPER-M. (2002). Terahertz pulse imaging in reflection geometry of human skin cancer and skin tissue, *Phys. Med. Biol.*, **47**(21), pp. 3853–3863.

WOODWARD-R. M., WALLACE-V. P., PYE-R. J., COLE-B. E., ARNONE-D. D., LINFIELD-E. H., AND PEPPER-M. (2003a). Terahertz pulse imaging of ex vivo basal cell carcinoma, *J. Investig. Dermatol.*, **120**(1), pp. 72–78.

WOODWARD-R., WALLACE-V., ARNONE-D., LINFIELD-E., AND PEPPER-M. (2003b). Terahertz pulsed imaging of skin cancer in the time and frequency domain, *Int. J. Biol. Phys.*, **29**(2-3), pp. 257–259.

WU-Q., AND ZHANG-X.-C. (1996). Ultrafast electro-optic field sensors, *Appl. Phys. Lett.*, **68**(12), pp. 1604–1606.

XIE-X., XU-J., DAI-J., AND ZHANG-X.-C. (2007). Enhancement of terahertz wave generation from laser induced plasma, *Appl. Phys. Lett.*, **90**(14), art. no. 141104.

XU-S., LIU-J., ZHENG-G., AND LI-J. (2010). Broadband terahertz generation through intracavity nonlinear optical rectification, *Opt. Express*, **18**(22), pp. 22625–22630.

XU-X., WEI-Y., SHEN-F., YIN-H., XU-J., GONG-Y., AND WANG-W. (2012). A watt-class 1-THz backward-wave oscillator based on sine waveguide, *Phys. Plasmas*, **19**(1), art. no. 013113.

YALLOP-C., AND DELBRIDGE-A. (2005). *The Macquarie Dictionary*, 4 edn, Macquarie Library.

YAMAMOTO-K., YAMAGUCHI-M., MIYAMARU-F., TANI-M., HANGYO-M., IKEDA-T., MATSUSHITA-A., KOIDE-K., TATSUNO-M., AND MINAMI-Y. (2004). Noninvasive inspection of C-4 explosive in mails by terahertz time-domain spectroscopy, *Jpn. J. Appl. Phys*, **43**(3B), pp. L414–L417.

YAMASHITA-M., OTANI-C., SHIMIZU-M., AND OKUZAKI-H. (2011). Effect of solvent on carrier transport in poly(3,4-ethylenedioxythiophene)/poly(4-styrenesulfonate) studied by terahertz and infrared-ultraviolet spectroscopy, *Appl. Phys. Lett.*, **99**(14), art. no. 143307.

YASUDA-T., IWATA-T., ARAKI-T., AND YASUI-T. (2007). Improvement of minimum paint film thickness for THz paint meters by multiple-regression analysis, *Appl. Opt.*, **46**(30), pp. 7518–7526.

YU-C., FAN-S., SUN-Y., AND PICKWELL-MACPHERSON-E. (2012). The potential of terahertz imaging for cancer diagnosis: A review of investigations to date, *Quant. Imaging Med. Surg.*, **2**(1), pp. 33–45.

ZANDONELLA-C. (2003). Terahertz imaging: T-ray specs, *Nature*, **424**(6950), pp. 721–722.

ZEITLER-J. A., SHEN-Y., BAKER-C., TADAY-P. F., PEPPER-M., AND RADES-T. (2007). Analysis of coating structures and interfaces in solid oral dosage forms by three dimensional terahertz pulsed imaging, *J. Pharm. Sci.*, **96**(2), pp. 330–340.

ZHANG-W., AZAD-A. K., AND GRISCHKOWSKY-D. (2003). Terahertz studies of carrier dynamics and dielectric response of n-type, freestanding epitaxial GaN, *Appl. Phys. Lett.*, **82**(17), pp. 2841–2843.

ZHAO-G., MORS-M. T., WENCKEBACH-T., AND PLANKEN-P. C. M. (2002a). Terahertz dielectric properties of polystyrene foam, *J. Opt. Soc. Am. B*, **19**(6), pp. 1476–1479.

ZHAO-G., SCHOUTEN-R. N., VAN DER VALK-N., WENCKEBACH-W. T., AND PLANKEN-P. C. M. (2002b). Design and performance of a THz emission and detection setup based on a semi-insulating GaAs emitter, *Rev. Sci. Instrum.*, **73**(4), pp. 1715–1719.

ZHONG-H., KARPOWICZ-N., AND ZHANG-X.-C. (2006). Terahertz emission profile from laser-induced air plasma, *Appl. Phys. Lett.*, **88**(26), art. no. 261103.

ZURK-L. M., ORLOWSKI-B., WINEBRENNER-D. P., THORSOS-E. I., LEAHY-HOPPA-M. R., AND HAYDEN-L. M. (2007). Terahertz scattering from granular material, *J. Opt. Soc. Am. B*, **24**(9), pp. 2238–2243.

Glossary

Acronyms

ATR	Attenuated Total Reflection
BBO	β-Barium Borate
BWO	Backward-Wave Oscillator
CCD	Charge Coupled Device
CW	Continuous-Wave
DAST	4-Dimethylamino-N-Methyl-4-Stilbazolium-Tosylat
DC	Direct Current
DFG	Difference Frequency Generation
EO	Electrooptical
FTIR	Fourier-Transform Infrared-Spectroscopy
GaN	Gallium Nitride
GaP	Gallium Phosphate
GaSe	Galllium Sellenide
HiZ	High-Impedence
ICP	Intrinsically Conducting Polymers
InGaAs	Indium Gallium Arsenide
KDP	Potassium Dihydrogen Phosphate
LDPE	Low-Density Polyethylene
$LiNbO_3$	Lithium Niobate
LIA	Lock-In Amplifier
LT-GaAs	Low-Temperature Grown Gallium Arsenide
ND	Neutral Density
OR	Optical Rectification
PCA	Photoconductive Antenna
PEDOT	Poly(3,4-ethylenedioxythiophene)
PPY	Polypyrrole
QCL	Quantum Cascade Laser
Redox	Reduction and Oxidation
SEM	Scanning Electron Microscope

SHG	Second-Harmonic Generation
Si	Silicon
SNR	Signal-to-Noise Ratio
TDS	Time-Domain Spectroscopy
THz	Terahertz
THz-TDS	Terahertz Time-Domain Spectroscopy
UV	Ultra-Violet
ZnTe	Zinc Telluride

Index

Biography

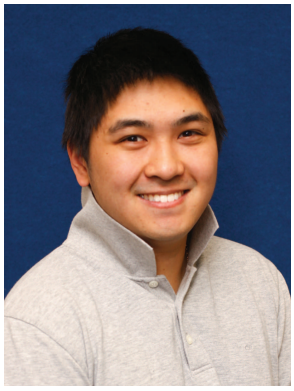

Benjamin Seam Yu Ung was born in Adelaide, Australia. He received Bachelor degrees in Engineering with honours in computer systems engineering and in mathematics and computer science from the University of Adelaide, in 2005. In 2006, Benjamin won a University of Adelaide Divisional Scholarship in pursuit of a PhD degree in electrical engineering at The University of Adelaide supervised by Prof Derek Abbott, Dr Bernd Fischer, and Dr Brian Ng.

In 2007, he was also a visiting scholar at the Polytechnic University of Hong Kong collaborating under Prof Charles Surya, and in 2008 was a visiting scholar at the Chinese University of Hong Kong collaborating under Prof Emma MacPherson. In 2009, received The University of Adelaide Research Abroad Scholarship.

Benajmin Ung was on the executive committee of IEEE affiliated Electrical and Electronic Engineering Society of Adelaide University (2006-2009) and is a member of IEEE and the OSA.

From 2013, Benjamin Ung is employed as a Postdoctoral Fellow with the Department of Electronic Engineering at the Chinese University of Hong Kong under Prof Emma MacPherson.

Benjamin Seam Yu Ung
bung@eleceng.adelaide.edu.au

Scientific Genealogy of **Benjamin Seam Yu Ung**